Computational Investigation of Lithium Metal Anodes for Solid-State Batteries

by

Jeong Seop Yoon

A dissertation submitted in partial fulfillment
of the requirements for the degree of
Doctor of Philosophy
(Mechanical Engineering)
in the University of Michigan
2023

Doctoral Committee:

Professor Jeff Sakamoto, Co-Chair
Professor Donald Siegel, Co-Chair, University of Texas at Austin
Associate Professor Neil Dasgupta
Professor Katsuyo Thornton

Jeong Seop Yoon

yujsyoon@umich.edu

ORCID iD: 0000-0002-9002-094X

Acknowledgements

First, I would like to express my gratitude to my advisor, Professor Donald Siegel, for his patient guidance and insightful mentorship throughout my Ph.D. study. His unwavering support has not only nurtured me as an independent researcher but has also honed my logical acumen in scientific investigations. It has been my privilege to push the boundaries of scientific knowledge under his expert advisement.

I extend my sincere thanks to my dissertation committee members, Professor Jeff Sakamoto, Professor Neil Dasgupta, and Professor Katsuyo Thornton. Through numerous collaborative sessions and dissertation discussions, their invaluable advice and constructive feedback have profoundly enriched my academic journey. I am truly grateful for their dedicated service on my thesis committee.

I am indebted to the members of the Energy Storage and Materials Simulation Lab, both past and present, for their constant support. The insightful feedback and camaraderie within the group have been helpful in shaping the course of my doctoral research. My gratitude also extends to the friends I have made at the University of Michigan, the University of Texas, and in Korea, who have infused joy into this Ph.D. expedition.

I wish to acknowledge the generous funding I have received from two sources: 1) the Joint Center for Energy Storage Research (JCESR), an Energy Innovation Hub funded by the U.S. Department of Energy, Office of Science, Basic Energy Sciences, and 2) the Department of Energy as part of the Energy Frontier Research Center *Mechano-chemical Understanding of Solid Ion Conductors* (MUSIC).

Last, my deepest appreciation goes to my parents and family for their boundless support and unwavering love. Their encouragement has been my rock throughout this transformative journey.

Table of Contents

List of Tables

List of Figures

List of Appendices

Abstract

Solid-state batteries that employ a Li-metal anode (LMSSB) are being widely explored within the battery community due to their potential to achieve improved energy densities. A solid-state battery would also convey safety benefits due to the elimination of the volatile and flammable liquid electrolytes commonly used in existing Li-ion systems. However, realizing these benefits is challenging, as it is widely known that LMSSBs suffer from internal short-circuiting due to dendrite formation and inefficiencies during cycling.

One hypothesis for suppressing dendrite formation in LMSSB suggests that maintaining interfacial contact between the Li anode and the solid electrolyte is crucial. At moderate discharge rates, relatively slower diffusion within the anode results in roughening and void formation in Li near this interface. The resulting reduction in interfacial contact focuses the Li-ion current during plating to a reduced number of contact points, generating high local current densities that nucleate dendrites.

In Chapters 3 and 4, a strategy for minimizing void formation in Li anodes is proposed. Using a multi-scale model, it is shown that capacity and current density in LMSSBs can be improved by reducing the grain size and increasing the dislocation density of Li, thereby exploiting fast diffusion within microstructural defects of Li anodes. Diffusion rates along 55 tilt and twist GBs, and two dislocation types (edge and screw) in Li are predicted using molecular dynamics. Using these atomic-scale data, a 1D meso-scale model of Li depletion in the anode during discharge was developed. The model predicts that grain sizes in the range of 0.1-3 μm, or dislocation densities of 10^{11}-10^{12}/cm^2, yield sufficiently fast self-diffusivity to enable robust

LMSSBs. The range of values reflects the range of diffusivities predicted in the dislocation cores and GBs, and approximations intrinsic to the meso-scale model. As the optimal grain sizes and dislocation densities are different from those in common use by several orders of magnitude, strategies for controlling the microstructures of Li metal are discussed. Lastly, by using atomistic data, a plastic deformation map is constructed for Li anodes under stack pressure. The map indicates that when the grain size is large (~150 μm), dislocation-climb dominates the creep deformation. However, in fine-grained Li (~1 μm), grain boundary sliding creep is the dominant mechanism of plastic deformation.

Regarding cycling inefficiencies in LMSSB, another hypothesized failure mode relates to the interfacial wettability of the Li anode and the metal current collector during operation of 'anode-free' LMSSBs. When Li and a metal substrate have poor work of adhesion, the nucleation barrier of Li on a metal surface (e.g., Cu foil) can be large. This can result in inhomogeneous deposition of Li and overpotentials of that deposition.

To understand the origin of low adhesion between the Li and a Cu substrate, in Chapter 5 the properties of Li/Cu and Li/Cu_2O interfaces were computed using density functional theory. These calculations indicate that Cu and Cu_2O are lithiophilic; thus Li is predicted to wet both materials. However, the strongly exothermic conversion reaction, $Cu_2O + 2\ Li \rightarrow Li_2O + 2\ Cu$, instead favors the formation of a Li/Li_2O interface. Prior work has shown that the stoichiometric Li/Li_2O interface exhibits poor wetting behavior. A mechanism involving the conversion of native copper oxide into Li_2O is consistent with the observation of inhomogeneous Li plating on Cu and high overpotentials observed experimentally in anode-free LMSSBs.

Chapter 1 Introduction

1.1 Motivation

Toward the decarbonized world, the transition from fossil fuels to carbon-free energy sources is accelerated. In step with this trend, the demand for lithium-ion batteries (LIB) is ever-increasing. LIB's application in portable electronics is extended to electric vehicles (EV), grid storage, and even electric aircraft.[1] The significant growth of the market and applications of LIB has been possible because of the sustained improvement in battery performance and price; Now, the gravimetric energy density of LIB is over 250 Wh/kg (90 Wh/kg in 1990s), and the cost of LIB modules is less than 150 USD/kWh (over 1000 USD/kWh previously).[2,3]

Despite the advancement, there are challenging issues hampering the further scaling of the current LIB. First, it is hard to enhance the gravimetric/volumetric energy density of LIB using a bulky graphite anode. As shown in Fig 1.1,[4] when Li metal replaces the graphite anode, a significant increase in specific energy and energy density is predicted; SSB using Li anode and NCA (e.g., $LiNi_{0.8}Co_{0.15}Al_{0.05}O_2$) cathode is estimated to satisfy the EV targets of 350 Wh/kg[5] and 750 Wh/L proposed by U.S. Department of Energy (DOE). Second, batteries using liquid electrolytes have a safety problem. Because of the flammability and volatility of organic solvents, weakness to physical damage, and the leakage issue, the replacement of liquid to solid-state electrolyte is pursued. Third, metal resource problems and the demand for a lower cost per battery require “beyond Li-ion” technologies.[4]

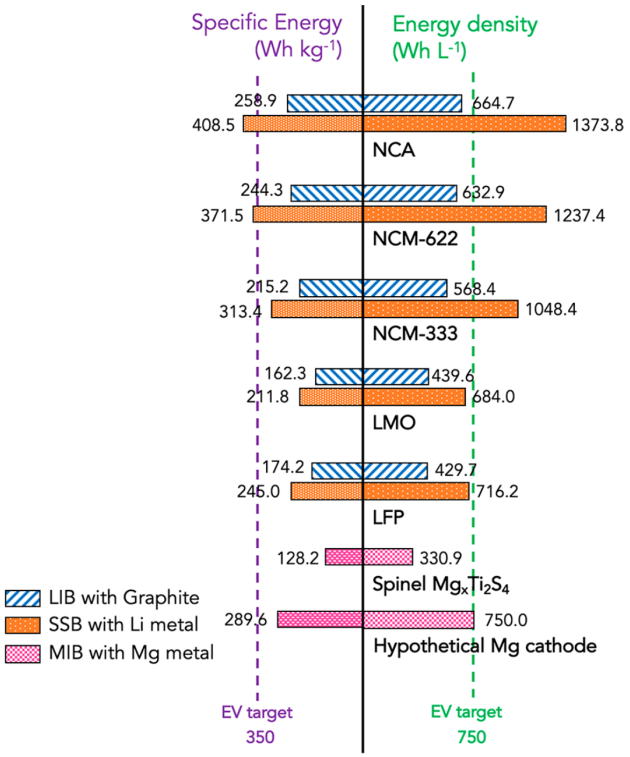

Figure 1.1 Specific energy and energy density for lithium-ion batteries (LIB) using a graphite anode, for solid-state batteries (SSB) using a Li metal anode, and for magnesium ion batteres (MIB) using a Mg anode, in combination with different cathode materials.[4]

1.2 Li Metal Solid-State Batteries

Developing next-generation batteries that can outperform the current Li-ion battery remains a very active area of research. Possible next-generation chemistries include: Na-ion and K-ion batteries, all-solid-state batteries, multivalent (Mg, Ca) batteries, etc. Among these, all-solid-state batteries employing a Li metal anode (LMSSB) are considered a promising candidate because of their advantages of improved safety and high gravimetric/volumetric energy density compared to conventional Li-ion batteries. To realize LMSSB, first, many studies have been performed to develop solid electrolytes (SE) satisfying the performance requirements: high ionic

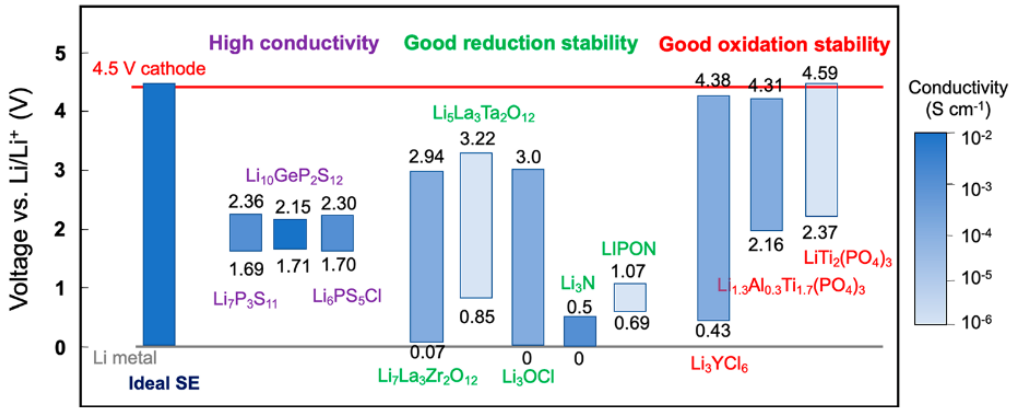

Figure 1.2 Ionic conductivity and calculated oxidation/reduction limits of solid electrolytes(SE). An ideal SE should show high ionic conductivity (~10^{-2} S/cm) and a wide electrochemical window.[4]

conductivity (~10^{-2} S/cm) with electrically insulating properties; a wide electrochemical window and chemical stability at interfaces with Li metal anode and cathode materials; good mechanical properties to be resistant to dendrite initiation and growth. Though various types of SE have been developed, more studies are required to find solid ionic conductors which meet all requirements. Typically, sulfide SE, such as LGPS or argyrodite (e.g., LPSCl), have been reported to have a high ionic conductivity (10^{-3}-10^{-2} S/cm).[6,7] However, sulfide SE has shortcomings, such as high sensitivity to moisture in the air and reactivity with electrode materials. On the other hand, oxide SE, such as garnets (e.g., $Li_7La_3Zr_2O_{12}$), exhibit high stability in the air, large electrochemical window, and good ionic conductivity (10^{-4}-10^{-3} S/cm, though slower than sulfide SE).[4]

Second, enhancing interfacial stability between solid electrolytes and electrode materials has been investigated in previous works.[8–11] Oftentimes, interfacing Li anodes with SE is challenging because of the high reactivity of Li metals. When the reaction product of Li and SE forms an interface comprised of ionic and electronic mixed conducting phases, the decomposition of SE can be extended. To mitigate this, introducing an artificial passivation layer has been suggested to form electrically insulating products (e.g., Li_3N, Li_2S, Li_2O, Li_3P) at the

interface.[11–13] Developing a thermodynamically stable pair of cathode and SE is also challenging. Interfacial instability of the sulfide SE and layered oxide cathode materials have been reported.[14,15] Therefore, stabilizing the cathode/SE interface by introducing a passivation coating is another active research area.[8,10,16]

Third, addressing the dendrite formation issue is critical to realize LMSSB. It has been reported that the loss of interfacial contact between Li and SE during stripping can cause dendrite growth and failure of a battery;[17,18] Such a contact loss at the Li/SE interface has been hypothesized to arise from the slower self-diffusion rate in Li than in SE.[19] In spite of many efforts to suppress the dendrite precipitation, studies have reported that dendrites are observed during cycling LMSSB even at the current density much lower than the current level required for advanced applications (e.g., electric vehicles).[19,20]

1.3 Challenges in Li Metal Solid-State Batteries

One of the challenges in developing Li metal solid-state batteries (LMSSB) is relevant to dendrite formation. Originally, the dendrite issue has plagued conventional Li-ion batteries using liquid electrolytes since it can lead to an internal short circuit and the explosion of a cell. However, by replacing the liquid-phase with stiff solid-phase electrolytes, the dendrite initiation was expected to be preventable; In the study of Monroe and Newman,[21] solid electrolytes with a shear modulus two times larger than that of Li metal were predicted to suppress dendrites. Nevertheless, even the batteries satisfying Monroe's criterion are observed to suffer from dendrite issues, indicating this condition is not sufficient, and more variables play a role.

One hypothesis to explain the origin of dendrites is related to the void formation

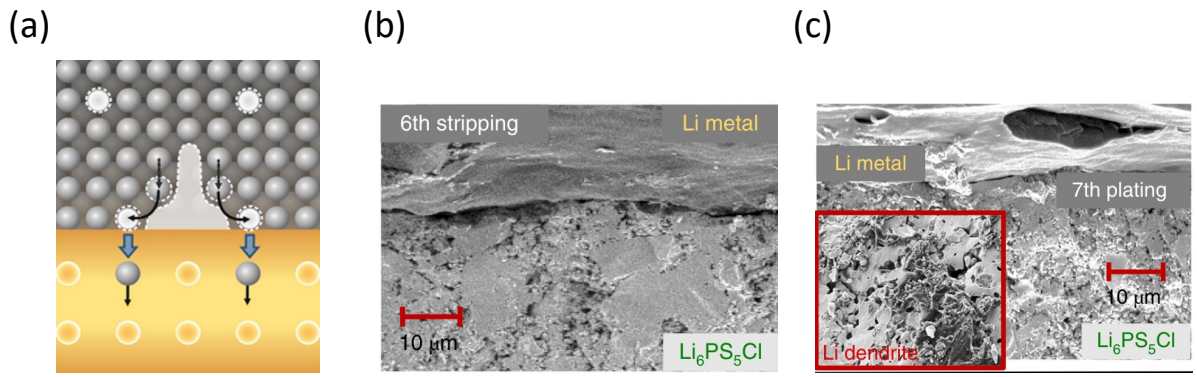

Figure 1.3 Morphology evolution of Lithium metal anode at the Li/SE interface. (a) Schematic shows that when the stripping current density is high, the rate at which Li is removed at the interface can be faster than the rate at which Li is replenished, resulting in void formation.[17] SEM images show that (b) during stripping, voids are formed at the Li/SE interface, and (c) dendrites are initiated during the subsequent plating.[18]

at the Li/SE interface during stripping.[17] At moderate discharge rates, relatively slower diffusion within the anode results in roughening and void formation in Li near the Li/SE interface. The resulting reduction in interfacial contact focuses the Li-ion current during plating to a reduced number of contact points, generating high local current densities that nucleate dendrites.[17,18] In prior studies, several approaches have been made to prevent the void formation: applying a high stack pressure to induce creep deformation of Li;[17,18,22] raising the temperature to increase self-diffusivity of Li;[23] and alloying Li with other metals to retain the good contact between Li and SE.[24,25] Though these approaches have demonstrated the longer retention of Li/SE interface at higher current rates, all exhibit tradeoffs associated with their implementation in practical LMSSB.

Another key challenge in developing LMSSB is cycling inefficiencies in an "anode-free" cell. One hypothesis explains that this is related to the nucleation overpotential and inhomogeneous nucleation and growth of Li on the metal current collector (e.g., Cu foil). Because of the poor wettability of Li and a metal substrate, the nucleation barrier of Li on a

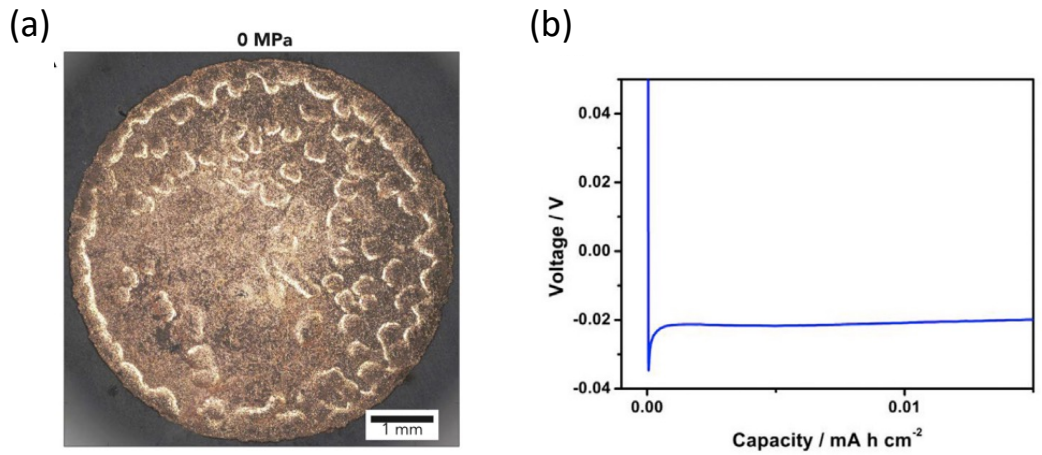

Figure 1.4 (a) The optical image shows the inhomogeneous deposition of Li to Cu current collector in a Li/LLZO/Cu cell under no stack pressure.[26] (b) Voltage profile during Li deposition to the interface between Cu current collector and LLZO at 0.05 mA/cm^2. The difference between the minimum voltage and plateau level indicates the nucleation overpotential of Li.[27]

metal foil can be large, as shown in Figure 1.4.[26,27] As energy penalties are required to nucleate Li on a metal during charging, it is less efficient. Also, since the poor wettability between Li and a current collector can cause contact loss at the Li/current collector, the Coulombic efficiency can be degraded.[28] The study of Dudney et al.,[29] showed that in an "anode-free" cell when Li nucleates non-uniformly on the current collector and isolated Li islands are formed, low reversibility and damage to the current collector can occur.

Several studies have demonstrated lowering the nucleation energy of Li on Cu current collector and enhancing the wetting by introducing an interlayer between Li and Cu substrate.[6,30–32] However, a limited number of studies focused on revealing the origin of Li nucleation overpotential on Cu foil. Oftentimes, it is hypothesized that the Li nucleation barrier is attributed to the negligible solubility of Li and Cu metal, and the poor work of adhesion between them. However, there are works hinting lithiophilicity of Cu metal,[6,33] contradicting previous hypothesis on the Li and Cu metal interface. It would be worthwhile to perform

comprehensive atomistic simulations to reveal the origin of nucleation overpotential of Li on a Cu foil.

In this dissertation, we focus on understanding Li metal anode in terms of kinetic and thermodynamic properties using multiscale simulations 1) to understand how the microstructure of the anode can impact the cell performance, and 2) to clarify how the presence of residual oxide on the current collector can influence interface formation.

1.4 Goals and Outline

The main goal of this thesis is to use atomic-scale simulations to understand mechanisms that underlie dendrite formation and cycling inefficiencies in Li metal-solid state batteries (LMSSB). As discussed in section 1.3, one hypothesis is that void formation at the Li/SE interface leads to dendrite initiation in LMSSB. To minimize void formation, we explore whether enhancing the polycrystalline diffusivity of Li anode can be achieved by increasing microstructural defects (i.e., grain boundaries, dislocations) in Li metal. These features can be fast diffusion pathways in other solids. Another hypothesis regarding cycling inefficiency in the anode-free LMSSB focuses on inhomogeneous plating due to poor wettability between Li and metal current collector. To understand the non-uniform plating of Li on the Cu current collector, we investigated the thermodynamics and adhesive properties of interfaces involving Li and Cu (or Cu oxide). The outline of this dissertation is as follows.

Chapter 2 covers the methodology of atomistic simulations employed in this dissertation. First, the fundamentals of first principles calculations are explained, including the Schrödinger of DFT. Second, the framework of classical molecular dynamics (MD) is explained. Subsequently, the interatomic potential (i.e., 2NN-MEAM) used to measure the intrinsic physical properties of

Li metal is overviewed. Third, various models for the prediction of Li polycrystalline diffusivity and effective volume diffusivity are discussed. Afterward, the mesoscale model based on 1-D Fick's law is explained, including assumptions for initial and boundary conditions, and the context of exploiting the model to predict the performance of batteries.

Chapter 3 discusses exploiting grain boundary diffusion to minimize dendrite formation in Li metal-solid state batteries. Using MD, the self-diffusivities of Li atoms in 55 distinct tilt/twist grain boundaries are measured, and overall polycrystalline diffusivity of Li metal is predicted as a function of grain size and temperature. Lastly, by mesoscale simulations based on Fick's 2^{nd} law, the discharge process of LMSSB is investigated, revealing the importance of the anode's microstructure on the performance of LMSSB.

Chapter 4 investigates exploiting fast diffusion in microstructural defects (i.e., dislocation, grain boundary) to minimize dendrite formation in Li metal-solid state batteries. Using MD, the transport properties in edge and screw dislocations are calculated, and the polycrystalline diffusivity of Li is computed as a function of grain size, dislocation density, and temperature. The mesoscopic model developed in Chapter 3 is parameterized with the atomistic data to identify the design/operating parameters to achieve performance targets of advanced Li metal batteries.

Chapter 5 presents predicting the wettability of the interface between Li and Cu current collector. Using DFT, the thermodynamic properties of Li/Cu and Li/Cu_2O interfaces are studied. Subsequently, by combining our study's results with prior studies on the lithiation of Cu_2O, and Li/Li_2O interface, a model is proposed to explain the wetting of Li on the Cu current collector as plating progresses.

Chapter 6 concludes this thesis by summarizing the findings, and suggests the future work for the development of LMSSB.

One manuscript of computational studies in this dissertation is under review for publication in a peer-reviewed journal (Chapter 3), and two manuscripts are in preparation (Chapters 4 and 5). In addition, it needs to be acknowledged that experimental characterizations are in progress in the collaboration group for the Li and Cu foil interface to confirm our computational findings. (Chapter 5).

Chapter 2 Methodology

2.1 First Principles Calculations

2.1.1 Schrödinger Equation

To understand the behavior of materials at the atomistic level, the quantum mechanical prediction of a material's electronic structure is required. Schrödinger equation describes how the electronic wavefunction of a physical system evolves over time, and evaluates the total energy of a system. As the formalism is extremely complex, assumptions can be made to simplify the calculations of the electronic wave function. First, since the atomic nuclei are significantly heavier than electrons, nuclei can be treated as static (Born-Oppenheimer approximation[34]). Second, electrons in a system are assumed to be non-relativistic and time-independent. With these assumptions, the many-body Schrödinger equation will read,[35]

$$\left[\frac{h^2}{2m}\sum_{i=1}^{N}\nabla_i^2 + \sum_{i=1}^{N}V(r_i) + \sum_{i=1}^{N}\sum_{j<i}U(r_i,r_j)\right]\Psi = E\Psi \qquad (2.1)$$

where h is Planck's constant, m is the mass of an electron, N is the number of total electrons, V is the potential function of electron-nuclei interaction, U is the potential function of electron-electron interaction, r is the position of the i^{th} electron, Ψ is the electronic wave function, E is the ground state energy. The three terms in the bracket of equation (2.1), in sequence, correspond to the kinetic energy of electrons, the interaction energy between electrons and nuclei, and the interaction energy between electrons. Despite the approximations, solving time-independent Schrödinger equations are infeasible except for the simplest systems of atoms, because of the high dimensionality of wave functions (i.e., 3N for N electron system).

2.1.2 Density Functional Theory

By solving the functional of electron density instead of the many-body Schrödinger equation, the ground state energy of the system can be calculated. The functional can be expressed as follows,

$$E[n(\boldsymbol{r})] = T_o[n(\boldsymbol{r})] + \int V(\boldsymbol{r})n(\boldsymbol{r})d\boldsymbol{r} + E_H[n(\boldsymbol{r})] + E_{XC}[n(\boldsymbol{r})] \quad (2.2)$$

where, T_o is the kinetic energy of electrons, V is the potential energy of electron-nuclei interaction, E_H is the Hartree energy, E_{XC} is the exchange-correlation energy, $n(\boldsymbol{r})$ is the electron density. The electron density can be calculated with the following equation,

$$n(\boldsymbol{r}) = 2\sum_{i=1}^{N} \psi_i^*(\boldsymbol{r})\psi_i(\boldsymbol{r}) \quad (2.3)$$

where, ψ_i is the wavefunction of the ith electron.

The set of wavefunctions of the ground state energy of a system can be determined by self-consistently solving the Kohn-Sham equation[36] given by,

$$\left[\frac{h^2}{2m}\nabla^2 + V(\boldsymbol{r}) + V_H(\boldsymbol{r}) + V_{XC}(\boldsymbol{r})\right]\psi_i(\boldsymbol{r}) = \varepsilon_i\psi_i(\boldsymbol{r}) \quad (2.4)$$

where ε_i is the eigenvalue of ith electron, V_H is the Hartree potential, V_{XC} is the exchange-correlation potential. The Hartree potential is as follows,

$$V_H(\boldsymbol{r}) = e^2 \int \frac{n(\boldsymbol{r}')}{|r-\boldsymbol{r}'|} d\boldsymbol{r}' \quad (2.5)$$

and the exchange-correlation potential is as follows,

$$V_{XC}(\boldsymbol{r}) = \frac{\delta E_{XC}(\boldsymbol{r})}{\delta n(\boldsymbol{r})} \quad (2.6)$$

Assuming the initial electron density, the Kohn-Sham equation can calculate the wave function of each electron in the system. Subsequently, all electronic wave functions can be exploited to calculate the electron density $n(\boldsymbol{r})$, and these iterations proceed until $n(\boldsymbol{r})$ converges. Finally, the converged electron density can be used to obtain the ground state energy of the system.

2.1.3 Exchange-Correlation Functional

When solving the Kohn-Sham equation, as the exact form of the exchange-correlation functional is not known, approximate expressions are required. Various approximations for the exchange-correlation term have been developed, such as the local density approximation (LDA), the generalized gradient approximation (GGA), Hybrid functionals, etc.

First, LDA approximates a uniform electron gas, and the exchange-correlation energy at each position is determined by the known exchange-correlation potential of the uniform electron gas with the electron density of that position.[35]

$$V_{XC}^{LDA}(\boldsymbol{r}) = V_{XC}^{electron\ gas}[n(\boldsymbol{r})] \tag{2.7}$$

LDA is known to work reasonably well when the variation of electron density with respect to position is small.

Second, GGA considers the gradient of the electron density, and it can be expressed by,

$$V_{XC}^{GGA}(\boldsymbol{r}) = V_{XC}^{GGA}[n(\boldsymbol{r}), \nabla n(\boldsymbol{r})] \tag{2.8}$$

The commonly used GGA functionals are the Perdew-Burke-Ernzerhof (PBE)[37] and the Perdew-Wang functional (PW-91)[38]. In some cases (e.g., Fe), where LDA predicts wrong ground state structures, GGA can correct the failings of LDA. In addition to these approximations, there are more exchange-correlation functionals, including hybrid functional,[39,40] DFT+U functional,[41] van der Waals functional,[42] etc.

2.1.4 Implementation

In chapter 5, for accurate predictions of thermodynamic properties of Li/Cu and Li/Cu_2O interfaces, first-principles calculations were performed through the Vienna *Ab-initio* Simulation Package (VASP)[43]. The ground state energy of relaxed structures was calculated to obtain

interfacial properties, such as the work of adhesion, interface formation energy, and strain energy. The interaction between an ion core and valence electrons was treated with the projector augmented wave (PAW)[44,45] method. In all calculations, GGA-PBE functional was used, and the grid of Gamma-centered k-points and the energy cutoff confirmed in convergence tests were adopted. In addition, all calculations were implemented with the Gaussian smearing width of 0.1 eV and no spin polarization.

2.2 Classical Molecular Dynamics

2.2.1 Principles of Molecular Dynamics

Molecular Dynamics (MD) is a simulation method based on Newton's law of motion to predict the time-evolution of a system of particles.

$$\boldsymbol{F} = m\boldsymbol{a} = m\frac{d\boldsymbol{v}}{dt} = m\frac{d^2\boldsymbol{r}}{dt^2} \tag{2.9}$$

The force exerted on each atom at each time can be calculated by using the negative gradient of the potential U of the simulation cell.

$$\boldsymbol{F} = -\nabla U(\boldsymbol{r}) \tag{2.10}$$

Velocity Verlet algorithm[46,47] is a commonly used method to update the position, velocity, and acceleration of atoms in the cell at the next time step $t+\Delta t$, over the course of the simulation. In this algorithm, the velocity at the next half-time step $t + \frac{1}{2}\Delta t$ is calculated first, and then the position and acceleration at the next time step $t + \Delta t$ are calculated subsequently as follows.

$$\boldsymbol{v}(t + \tfrac{1}{2}\Delta t) = \boldsymbol{v}(t) + \tfrac{1}{2}\boldsymbol{a}(t)\Delta t \tag{2.11}$$

$$\boldsymbol{r}(t + \Delta t) = \boldsymbol{r}(t) + \boldsymbol{v}(t + \tfrac{1}{2}\Delta t)\Delta t \tag{2.12}$$

$$\boldsymbol{a}(t+\Delta t) = -\frac{1}{m}\nabla U(\boldsymbol{r}(t+\Delta t)) \tag{2.13}$$

Lastly, the velocity of atoms at the next time step can be computed with equation 2.14.

$$\boldsymbol{v}(t+\Delta t) = \boldsymbol{v}\left(t+\frac{1}{2}\Delta t\right) + \frac{1}{2}\boldsymbol{a}(t+\Delta t)\Delta t \tag{2.14}$$

As the simulation progresses, atomic positions, velocities, and energies can be updated, which can be exploited to analyze the structural, thermodynamic, and kinetic properties of a system.

2.2.2 Force-Field

To evaluate the thermodynamic and transport properties of Li metal, the force field developed by Kim et al[48] is adopted. It is an interatomic potential based on the second nearest-neighbor modified embedded atom method (2NN-MEAM), which accurately describes the various fundamental physical properties of the pure Li metal. The (2NN) MEAM formalism calculates the total energy of a system with equation 2.15.

$$E = \sum_i \left[F_i(\overline{\rho}_i) + \frac{1}{2}\sum_{j(\neq i)} S_{ij}\phi_{ij}(R_{ij})\right] \tag{2.15}$$

The first term in the bracket evaluates the energy F_i, required to embed an atom i in the background electron density $\overline{\rho}_i$. In the following term, $\phi_{ij}(R_{ij})$ captures the pair-interaction between atoms i and j separated by the distance R_{ij}, while S_{ij} is the screening function representing the impact of all other neighbor atoms k on the interaction between atoms i and j.

2NN-MEAM captures the angular contributions by considering the directionality of bondings to compute the background electron density at each atomic site; In addition, compared to the MEAM force field, the interaction range in 2NN-MEAM is enlarged to the second nearest neighbor atoms, which allows more accurate predictions of physical properties of bcc Li.[49]

Therefore, in Chapters 3 and 4, all classical calculations for the Li metal are performed with 2NN-MEAM of Kim et al[48] using LAMMPS.[50] Because of the lower computational cost, the classical method enabled modeling of microstructural defects of Li (i.e., GB and dislocation) in large-scale simulation cells, and the measurement of Li transport properties in these defects.

2.3 Mesoscale simulation

2.3.1 Polycrystalline Diffusivity (GB+TJ+Bulk)

In Chapter 3, to evaluate the diffusion rates in polycrystalline Li, four different models are considered. Depending on assumptions on the microstructures, the models describe the transport in the intergranular regions (GBs, and triple junctions (TJs) in the Chen's model) and the intragranular regions (Bulk) differently.

First, the Hart equation[51,52] for $D_{polycrystal}$ (i.e., polycrystalline diffusivity) assumes that the 1-D diffusion direction is parallel to GB planes as described in Fig 2.1a. As this model neglects laterally interconnected GB regions (i.e., GBs perpendicular to the diffusion direction), the calculated diffusivity can be regarded as an upper bound of polycrystals. Recent experimental reports have observed columnar-shaped grains[53,54] in Li following plating. In this case, the Hart model is a more suitable model for predicting the transport in Li polycrystalline. $D_{polycrystal}$ can be obtained from equation 2.16, where f is GB volume fraction and D_{GB} and D_{Bulk} are self-diffusivities of the GB and Bulk, respectively. Equation 2.17 from the regular polygon model[55] is used to calculate the GB volume fraction in polycrystals.

$$D_{Polycrystal} = fD_{GB} + (1-f)D_{Bulk} \tag{2.16}$$

$$f = 1 - \left(1 - \frac{w}{d}\right)^2 \text{ (w: GB width, d: Grain diameter)} \tag{2.17}$$

Second, the other extreme of polycrystalline diffusivities is estimated by the 1-D Maxwell-Garnet model[52,56] which assumes that the diffusion direction is normal to GB planes (Fig 2.1b). The general equation of this model is derived for the effective diffusivity of a composite, where the spherical inclusions and the host represent grains and GBs in a polycrystal, respectively.[57] The Maxwell-Garnet formula for $D_{polycrystal}$ is given by equation 2.18,

$$D_{Polycrystal} = \frac{D_{GB}[\left(f+d^{'}-fd^{'}\right)D_{Bulk}+fD_{GB}(d^{'}-1)]}{D_{GB}\left(d^{'}-f\right)+fD_{Bulk}} \tag{2.18}$$

where $d^{'}$ is the arbitrary space dimension. ($d^{'}$=1: GBs perpendicular to the diffusion direction, $d^{'}$=2 or 3: GBs enclosing 2D-circular or 3D-spherical grains).

Third, the generic 2D-patterned Grain model[52] falls between the extremes of the two previous models in that it assumes that half of GB planes are oriented perpendicular to the diffusion direction, while the other half are parallel (Fig 2.1c). In this case, $D_{polycrystal}$ is given by:

$$D_{Polycrystal} = \frac{D_{GB}(\varepsilon(1-\varepsilon)D_{GB}+\left(1-\varepsilon+\varepsilon^2\right)D_{Bulk})}{\varepsilon D_{Bulk}+(1-\varepsilon)D_{GB}} \tag{2.19}$$

$$\varepsilon = w/(w+d) \tag{2.20}$$

where ε is the volume fraction of GBs normal to the diffusion direction.

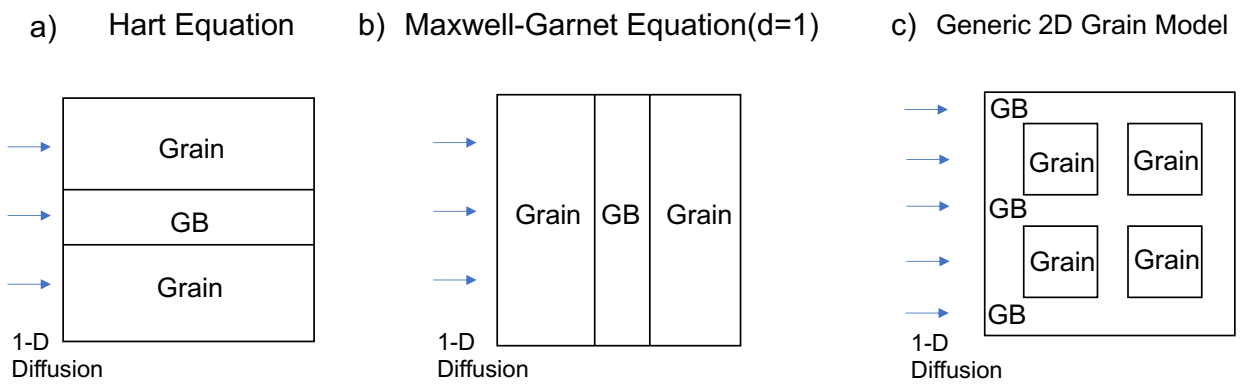

Figure 2.1 Li Polycrystalline diffusivity as predicted by 3 models that make different assumptions about GB orientation. Schematic a-c show the Hart model(GB parallel with 1-D diffusion), Maxwell-Garnet model(GB normal to 1-D diffusion), 2D grain model(relative to 1-D diffusion, both normal and parallel GBs are present) respectively.

Lastly, another generic model proposed by Chen et al[58] is examined. The assumptions in this model include that 1) bulk grains are enclosed by GBs and TJs, 2) TJs isolate the neighboring GB facets, 3) grains are assumed to have the Voronoi polyhedral shape and log-normal size distribution, and 4) no dislocation pipes are present in bulk grains. In this model, $D_{polycrystal}$ can be calculated by equation 2.21,

$$D_{Polycrystal} = f_{TJ}D_{TJ} + f_{GB}D_{GB} + f_{Bulk}D_{Bulk} + \frac{f_{TJ}f_{GB}(D_{TJ}-D_{GB})^2}{f_{TJ}(D_{TJ}-D_{GB})-2(f_{GB}+f_{TJ})D_{TJ}} + \frac{f_{ig}f_{Bulk}(D_{ig}-D_{Bulk})^2}{f_{ig}(D_{ig}-D_{Bulk})-3D_{ig}} \quad (2.21)$$

where, f_{GB} f_{TJ}, f_{ig} are the volume fraction of GBs, TJs, and intergranular regions, respectively. The volume fraction parameters can be calculated with equations 2.22-2.24,

$$f_{GB} = H_{GB}\frac{w}{d} = 2.9105\frac{w}{d} \quad (2.22)$$

$$f_{TJ} = H_{TJ}\left(\frac{w}{d}\right)^2 = 2.5259\left(\frac{w}{d}\right)^2 \quad (2.23)$$

$$f_{ig} = f_{GB} + f_{TJ} \quad (2.24)$$

where H_{GB}, H_{TJ} are numerical factors determined by the grain shape and grain size distribution. D_{TJ}, D_{ig} are the diffusivity of triple junctions and intergranular regions (GBs and TJs). As D_{TJ} of Li is not available, assumptions are made that D_{TJ} could be 1, or 10^2, or 10^4 times D_{GB}. Equation 2.25 reads the expression for D_{ig},

$$D_{ig} = \frac{1}{f_{ig}}\left[f_{GB}D_{GB} + f_{TJ}D_{TJ} + \frac{f_{TJ}f_{GB}(D_{TJ}-D_{GB})^2}{f_{TJ}(D_{TJ}-D_{GB})-2f_{ig}D_{TJ}}\right] \quad (2.25)$$

As shown later in Figure 3.11, the prediction of the 2D grain model and the Maxwell-Garnet $d^{'}$ = 2,3 models are confirmed to be similar to those of the Hart model across the range of diffusivities observed for the different GBs. In addition, when D_{TJ} is assumed to be smaller than 10^2 D_{GB} (speculated to be reasonable guess given that D_{TJ} is approximately 2-10 times D_{GB} in

Cu[59]), Chen's model is confirmed to be within the error-bar range of the Hart model except at the ~10^{-2} μm grain size. As a result, we adopted the Hart equation to predict the polycrystalline diffusivity of the Li anode in Chapter 3.

2.3.2 Effective Volume Diffusivity (Dislocation+Bulk)

In section 2.3.1, when estimating the diffusivity of the intragranular region, only atom transport in the pristine BCC bulk region is considered. However, within grains, dislocations can provide a path for fast diffusion in Li metal via so-called pipe diffusion. There are two broad categories of transport models for a single crystal with dislocations, as depicted in Figure 2.2.

First, the Hart equation assumes that dislocation cores are parallel with the diffusion direction (Figure 2.2a). Equation 2.26 of Hart model[51] reads that f_{Pipe} is the volume fraction of dislocations in Li, D_{Pipe} and D_{Bulk} are the dislocation and bulk diffusivity at finite temperatures respectively. In particular, $f_{Dislocation}$ is obtained from the product of dislocation density ρ_{Pipe}, and cross-section area of dislocation pipe $\pi {r_d}^2$ (r_d is a pipe radius).

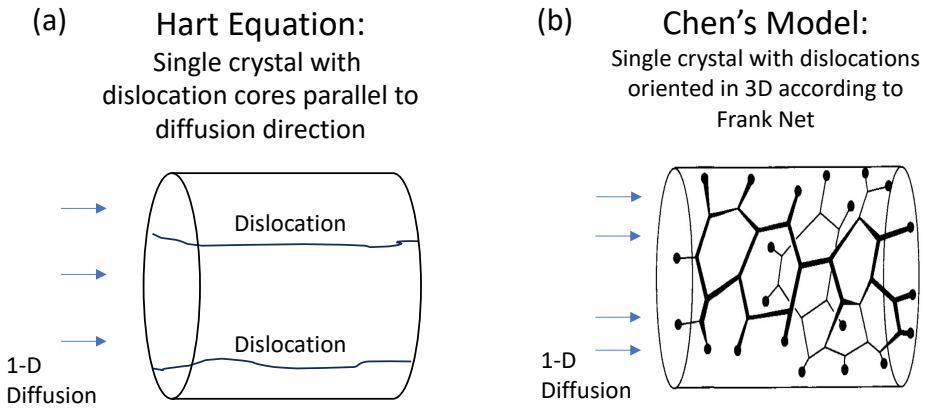

Figure 2.2 Effective volume diffusivity of Li as predicted by 2 models that make different assumptions about dislocation orientation. Schematic a-b show the Hart model (dislocation parallel with 1-D diffusion), Chen model (dislocations oriented in 3D according to Frank net[123]) respectively.

$$D_{effective} = f_{Pipe}D_{Pipe} + \left(1 - f_{Pipe}\right)D_{Bulk} \quad (2.26)$$

Second, the model proposed in Chen et al's study can account for the more realistic case where dislocations form a 3-dimensional network (or Frank net).[58] In this model, diffusion fluxes can pass along the two parallel diffusion paths in the intragranular region, i.e., the bulk region and the Frank network (Figure 2.2b). Equation 2.27 exhibits Chen's model,

$$D_{effective} = \left(1 - \frac{f_{Pipe}}{f_{Pipe}+f_{Bulk}}\right) D_{Bulk} + \left(\frac{f_{Pipe}}{f_{Pipe}+f_{Bulk}}\right)^{t} D_{Pipe} \quad (2.27)$$

where t is the scaling exponent, which can capture the non-parallel nature of diffusion along the network of dislocations. t can be determined by the dynamic and static exponents in 3 dimensions in percolation theory,[58,60] and t=1.4 proposed in the Chen et al's work is used in our calculations.[58]

Figure 4.9 later exhibits the effective diffusivities predicted by Hart and Chen's models as a function of dislocation density at various temperatures. The plots indicate that $D_{effective}$ from the two models are beyond the error-bar range of each other. Therefore, for the calculation of diffusivities in intragranular regions, both models are considered in this thesis.

2.3.3 Polycrystalline Diffusivity (Dislocation+GB+TJ+Bulk)

In section 2.3.1, various polycrystalline models considering GBs, TJs (in Chen's model), and bulk grain interior region are introduced. Among these models, the Hart model[51] is expected to reasonably describe the diffusion in the electrodeposited Li for two reasons: 1) experimental characterization of Li deposit shows columnar morphology, and 2) the other realistic models yield predictions that are comparable as shown in Figure 3.11.

In section 2.3.2, it is discussed that incorporating contributions of dislocation diffusion in the granular region enables more realistic modeling, and both Hart and Chen's models are taken into account. As two models predict distinct effective volume diffusivities (Figure 4.9), it is concluded that calculations need to be performed with both models.

In Chapter 4, we predict the polycrystalline diffusivity of Li metal by considering the dislocation pipe diffusions in intragranular regions, additionally. In total, two scenarios are considered.

First, the Hart models[51] for both intergranular (GBs) and intragranular (Bulk and Pipes) regions are integrated. This extended model assumes that GBs and intragranular dislocations are parallel with the 1-D diffusion direction. The corresponding equation 2.28 is expressed as,

$$D_{Polycrystal} = f_{GB}D_{GB} + f_{Pipe}D_{Pipe} + \left(1 - f_{GB} - f_{Pipe}\right)D_{Bulk} \tag{2.28}$$

$$f_{GB} = 1 - (1 - \frac{w}{d})^2 \quad \text{(w: GB width, d: grain diameter)} \tag{2.29}$$

$$f_{Pipe} = \pi {r_d}^2 \rho_{Pipe} \ (r_d\text{: pipe radius, } \rho_{Pipe}\text{ : dislocation density}) \tag{2.30}$$

Second, Chen's model[58] for the polycrystalline diffusivity is adopted. The model is based on assumptions that: 1) bulk grains are enclosed by GBs and TJs, 2) TJs isolate the neighboring GB facets, 3) grains are assumed to have the Voronoi polyhedral shape and log-normal size distribution, and 4) dislocations form a 3D network in bulk grains. The corresponding equation 2.31 is expressed as,

$$D_{Polycrystal} = f_{TJ}D_{TJ} + f_{GB}D_{GB} + f_{Bulk}D_{Bulk} + {f_{Pipe}}^{t}(f_{Pipe} + f_{Bulk})^{1-t}D_{Pipe} + \frac{f_{TJ}f_{GB}\left(D_{TJ} - D_{GB}\right)^2}{f_{TJ}(D_{TJ} - D_{GB}) - 2(f_{GB} + f_{TJ})D_{TJ}} + \frac{f_{ig}f_{Bulk}\left(D_{ig} - D_{Bulk}\right)^2}{f_{ig}(D_{ig} - D_{Bulk}) - 3D_{ig}} \tag{2.31}$$

All parameters regarding volume fraction, diffusivities, scaling factor t are explained in equations 2.22-2.25, 2.27, 2.30. In addition, as the Li D_{TJ} is not available, it is assumed to be 10^2 D_{GB} in calculations for Chapter 4 (See discussion in Figure 3.11).

Because Chen's model assumes more realistic microstructures in polycrystalline materials than Hart model, (e.g., a 3D network of dislocations VS 1D parallel dislocations), the $D_{Polycrystal}$ of two models are predicted to be different. For example, as exhibited in Figure 4.10 later, at 10^{11}/cm^2 dislocation density and 150 μm grain size, the $D_{Polycrystal}$ at 300K in Hart model ($4.3*10^{-10}$ cm^2/s) is estimated to be larger than that in Chen's model ($6.0*10^{-11}$ cm^2/s). The effect of selecting different polycrystalline models on the battery design guidelines will be explained further in Chapter 4 discussion section.

2.3.4 Mesoscale Model of Li Stripping in LMSSB

To simulate the Li anode stripping during the discharge of Li metal solid-state batteries (LMSSB), a mesoscale model is developed. The time and space-dependent Li concentration in the anode can be captured with 1-D Fick's 2nd law using Equation 2.32.

$$\frac{\partial C}{\partial t} = D\frac{\partial^2 C}{\partial x^2} \tag{2.32}$$

To solve the Fick's law partial differential equation, two boundary conditions and one initial condition are required. In our model, the following assumptions were made for the model,

1. There is no concentration gradient at x=L:

$$\frac{\partial C}{\partial x} = 0 \text{ (x=L, t>0).}$$

2. The Li flux, $J_{Migration}$, is driven by a constant current density i, at x=0:

$$J_{Migration} = \frac{i}{F} \text{ (x=0, t>0).}$$

3. At t=0, the concentration of Li across the anode is constant everywhere and equal to $C_o = 0.078$ mol/cm^3 : $C = C_o$ (0<x<L, t=0).

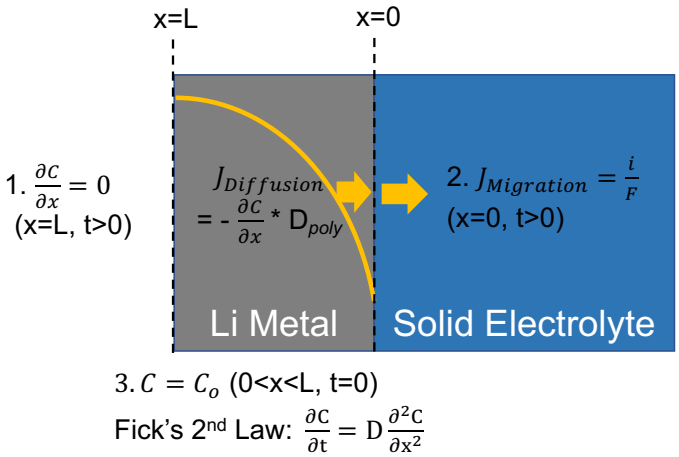

Figure 2.3 Boundary and initial conditions for the application of Fick's 2nd law to predict the Li concentration in the anode as a function of time and position. x=0 corresponds to the Li/SE interface, and x=L is an electrochemically non-active anode surface (corresponding to the current collector).

In addition, no stack pressure is assumed because this simulation is aimed at estimating the Li depletion point at the Li/SE interface, determined by two competing fluxes (i.e., the Li^0 diffusional flux in the anode and Li^+ ion flux in the SE driven by the stripping current).

The general solution to 1D Fick's law model with the given initial and boundary conditions has been reported in several studies[23,61], which reads,

$$C(x,t) = C_o - \frac{2It^{1/2}}{FD^{1/2}}\sum_{n=o}^{\infty}\left[ierfc\frac{2(n+1)L-x}{2(Dt)^{1/2}} + ierfc\frac{2nL+x}{2(Dt)^{1/2}}\right] \quad (2.33)$$

where t is time, x is position, D is the polycrystalline diffusivity, L is anode thickness, I is stripping current, C_o is initial Li concentration, and F is Faraday's constant. In our model, the polycrystalline diffusivity D is calculated as a function of grain size and dislocation density, and input to the general solution 2.33. Here, D is assumed to be constant and independent of the Li concentration. In this way, the atomistic data obtained from MD simulations were used to predict the Li stripping process at the mesoscopic level.

Several prior studies[23,24,61] have employed 1-D Fick's 2nd law with the given initial and boundary conditions above to describe the transport in the anode and to model battery performance. These studies showed that the upper bound of the deliverable capacity can be limited by the "depletion time," t_d [23,24,61] at which the concentration of metal atoms at the interface (between the anode and solid electrolyte) becomes zero. Using the notation in Eq. 2.33, at $t = t_d$, $C(x = 0, t = t_d) = 0$. In the study of Jow et al.,[61] the depletion time was used to determine the diffusivity within a Li anode interfaced with a $LiI(Al_2O_3)$ solid electrolyte. Krauskopf et al's work[24] also demonstrated that the delithiation process of the Li-Mg electrode interfaced with solid electrolyte could be predicted by 1-D Fick's law model. In the work of Tsai et al.,[23] a mathematical model based on the 1-D Fick's law was exploited to explain the enhanced discharge capacity and dendrite-tolerance of a Na metal symmetric cell (i.e., $Na/Na_{3.4}Zr_2(SiO_4)_{2.4}(PO_4)_{0.6}/Na$) with the high self-diffusivity of Na metal.

In this dissertation, by using the proposed mesoscale model based on 1-D Fick's law, we estimated the discharge capacity of LMSSB as a function of the discharge rate, anode thickness, and the microstructural features of Li anode (i.e., grain size, dislocation density). In this calculation, it is assumed that a void will be formed at the depletion time. However, it needs to be acknowledged that in a 3D system, before the depletion time, vacancies can be clustered and voids can be formed at the Li/SE interface. In conclusion, we demonstrate that the enhanced self-diffusivity of Li anode by the microstructural engineering can satisfy performance targets of the solid-state batteries employing Li metal anode.

Chapter 3 Exploiting Grain Boundary Diffusion to Minimize Dendrite Formation in Lithium Metal-Solid State Batteries

3.1 Introduction

The dendrite-based failure mode occurs during cycling at room temperature under moderate current densities and is precipitated by the formation of voids in the Li anode at the solid electrolyte interface during discharge/stripping.[17,18] Stripping from the Li anode generally does not occur in a homogeneous, layer-by-layer fashion; this behaviour results in Li voids or pits being formed at the interface. Janek et al[17] have argued that voiding occurs when the rate at which Li vacancies are formed during stripping exceeds the rate at which these vacancies are annihilated by the diffusion of Li atoms from other regions in the anode. Upon subsequent plating, the reduced interfacial contact resulting from the voids focuses Li deposition at the remaining (few) contact points, increasing the local current density and fostering dendrite nucleation.

One strategy that has been proposed to mitigate void formation is the application of pressure normal to the Li/SE interface.[17,18,22] This applied pressure can generate plastic deformation within the Li – specifically creep deformation – and facilitate the redistribution of Li so as to fill vacancies and voids. While this approach has demonstrated the ability to delay void formation to higher current densities, it is unclear whether the high pressures required – on the order of 10 MPa – are realistic in mass-produced cells. Moreover, recent work[62] by Fincher and Chiang has shown that these pressures encourage fracture of the solid electrolyte. For these reasons, the use of high pressure may not be an ideal solution.

A second strategy to minimize dendrite formation is to raise the temperature. Numerous authors have shown that the cyclability of a Li metal anode in contact with a SE dramatically improves as the temperature is increased.[19,23] The performance improvement at elevated temperatures can be attributed to faster self-diffusion and creep.[19,23] Unfortunately, and as with the use of pressure, it is not clear that a high-temperature battery is a practical solution, given that modern EV battery systems weigh hundreds of kilograms and should function in cold climates (-40 °C).

As a third strategy, Grovenor et al[25] examined whether alloying could speed up diffusion in a Li-based anode. More specifically, the diffusivity of Li in Li-Mg alloys with up to 30 at.% magnesium was measured with an isotope tracer method. They found that Li diffusivity was approximately an order of magnitude slower in the Li-Mg alloys, in contrast to prior reports.[24] At high current densities, the larger diffusivity of an unalloyed (pure) Li anode yielded superior performance compared to the alloyed variants. (Interestingly, and despite its larger Li diffusivity, at low current density the Li-Mg alloys were superior due to their ability to maintain interfacial contact with the SE.) While other alloy compositions may yield an improvement in Li-diffusivity, any alloy will add inactive mass and volume to the anode, penalizing (specific) energy density.

Here we propose a different approach to facilitating the redistribution of Li during stripping – exploiting GB diffusion within the Li anode. It is well known that diffusion along grain boundaries in polycrystalline materials can differ dramatically from diffusion in the bulk (i.e., within the grain interiors).[63–65] In some cases, the rate of GB diffusion is faster than in the bulk,[65–67] and in some cases, it is slower.[68–70] It is also well-established that the grain size (and thus the area fraction of GBs) of a polycrystalline metal can be influenced by its electro-

deposition rate and by substrate effects.[53,71–73] Thus, if GB diffusion in Li is fast, *and* the grain size can be kept small, then enhanced Li transport can be achieved without resorting to high pressure, elevated temperature, or alloying.

Here, using a multi-scale simulation methodology, a comprehensive analysis of GB diffusion in Li is presented. First, the self-diffusivity of Li in 55 distinct tilt and twist GBs are evaluated using molecular dynamics and a 2nd nearest-neighbor MEAM interatomic potential. These calculations predict that GB diffusion is 3 to 6 orders of magnitude faster than in bulk Li, reflecting a significantly smaller activation energy for GB diffusion. Subsequently, polycrystalline diffusivities are predicted as a function of grain size. At room temperature, the polycrystalline diffusivity of Li increases from ~10^{-11} for grains with 1 mm diameter to ~10^{-7} cm^2/s when the grain diameter is reduced to 10 nm. Finally, these atomistic data are used to parameterize a mesoscale diffusion model based on Fick's 2nd law. The model predicts the cell capacity as a function of discharge current density, anode thickness, and the grain size of the Li anode. The model reveals that an average grain size of approximately 1 μm can meet established performance targets of an all-solid-state lithium metal battery. Testable strategies for controlling the grain size during cycling are discussed.

3.2 Methods

The 2nd nearest-neighbor modified embedded-atom method force field (2NN-MEAM) for Li proposed by Kim et al[74] was used in the present study. Prior calculations using this potential have demonstrated that it accurately reproduces fundamental physical properties of Li, including elastic properties, vacancy formation and migration energies, surface energies, specific heat, etc. All simulations were conducted using the LAMMPS code.[50]

A total of 55 tilt and twist GBs were investigated. These systems employed different choices of the tilt/twist axes (i.e., [001], [01-1], [11-1]), misorientation angles, and coincidence site lattices. Tables A.1-A.2 list all of the GBs that were examined. Each grain boundary simulation cell used a bi-crystal structure with two equivalent interfaces and periodic boundary conditions applied in all three directions. The GB planes were separated by a bulk region of a minimum thickness of 6 nm to prevent interactions between the two interfaces. For all models, the GB plane was aligned parallel to the X-Z plane of the simulation cell; the GB normal was thus parallel to the Y direction.

Figure 3.1 shows a flow chart of the computational procedure used in this study. A multi-step process was used to identify the minimum energy structure of each GB. First, the γ surface was evaluated for each model by rigidly translating one grain relative to the other by either 1/8th or 1/16th of the length of the repeat unit in the X and Z directions. (The value 1/8th was adopted when the repeat unit was smaller than 14 Å). The resultant grid spacing in each direction was typically ~1 Å. For each translational state, pairs of close-contact atoms at the interface were identified. A single atom, chosen at random, was deleted from each pair. The threshold for close-contacts was varied from 1 - 2.6 Å in steps of 0.1 Å. The atom positions and simulation cell length along the Y direction were relaxed for each distinct translation state and close-contact criterion. Accounting for the different interfacial translations and close-contact distances, between 1088 and 4352 interface models were generated for each GB geometry. 162,112 initial GB structures were evaluated in total.

An example γ surface for a $\Sigma 5(310)/[001]$GB is shown in Figure 3.2. Similar plots for the other GBs are presented in Tables A.3-A.4. Subsequently, a 2nd relaxation was initiated from the minimum energy configuration on the γ-surface.

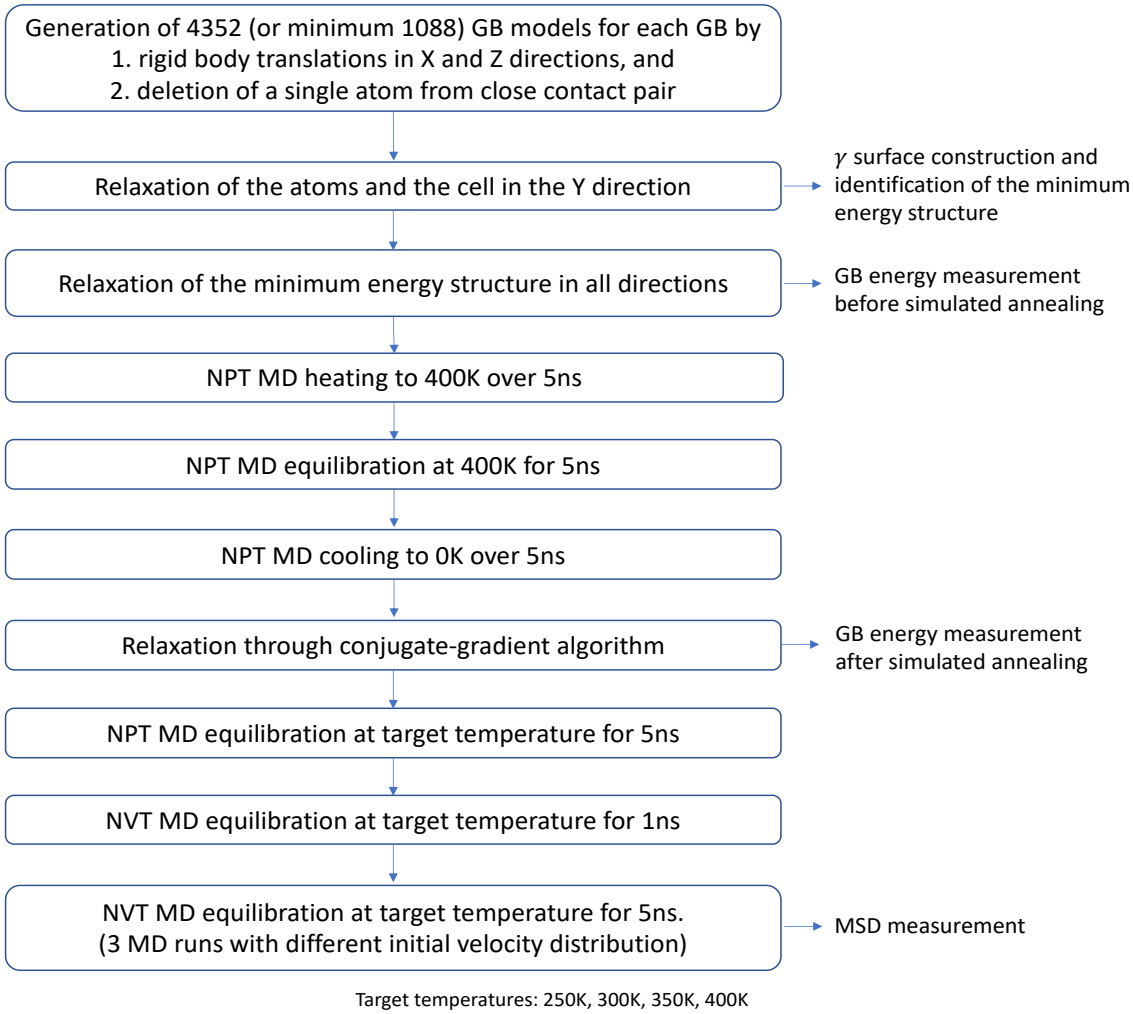

Figure 3.1 Flow chart describing the procedure for calculating GB diffusivity.

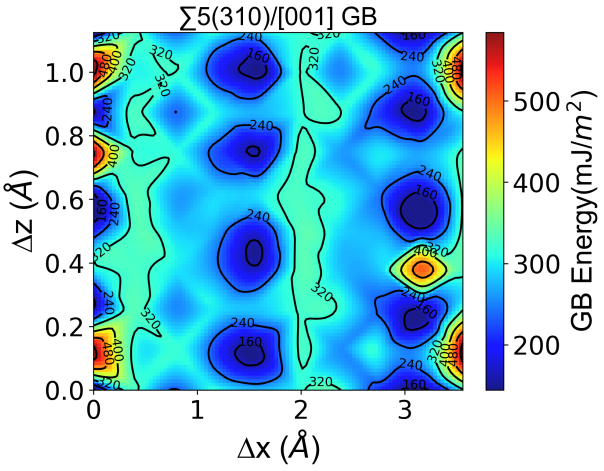

Figure 3.2 Calculated γ-surface for a $\Sigma 5$ $(310)/[001]$ GB.

In this case, all atomic positions and the cell size were relaxed in all degrees of freedom. The structure resulting from this second relaxation was used to calculate the GB energy, shown in Equation 3.1.

$$\gamma_{GB} = \frac{(E_{GB} - NE_{bulk})}{2A} \tag{3.1}$$

Here, γ_{GB} represents the GB energy, E_{GB} represents the total energy of the GB simulation cell, E_{bulk} is the total energy per atom of a bulk Li cell, N is the number of atoms in the GB cell, and A is the area of the GB plane. The numerator is the difference between the energy of the GB cell and that of a perfect lattice with the same number of atoms. The factor of 2 in the denominator accounts for the two distinct GBs contained within the simulation cell.

Finally, simulated annealing was used to further equilibrate the GBs and facilitate identification of the minimum energy GB structures. Starting from the lowest-energy geometry identified by the previous relaxation steps, NPT MD was used to heat each GB cell from 0 K to 400 K for over 5 ns at 1 atm. This was followed by NPT equilibration at 400 K / 1 atm for an additional 5 ns, and NPT cooling to 0 K / 1 atm over 5 ns. A final relaxation was performed and the GB energy was re-evaluated. The energies of the annealed structures were very similar to those obtained before annealing, suggesting that the GB geometries were close to the global energy minimum.

GB migration was observed in several of the annealing simulations. This migration is undesirable as it can reduce the separation between the two GBs (increasing the likelihood for GB/GB interactions). In extreme cases this can result in annihilation of the GBs (Figure 3.3). To minimize GB migration, the motion of a subset of atoms in the bulk regions were constrained. More specifically, atom motion in the y-direction (normal to the GB plane) was prohibited in two

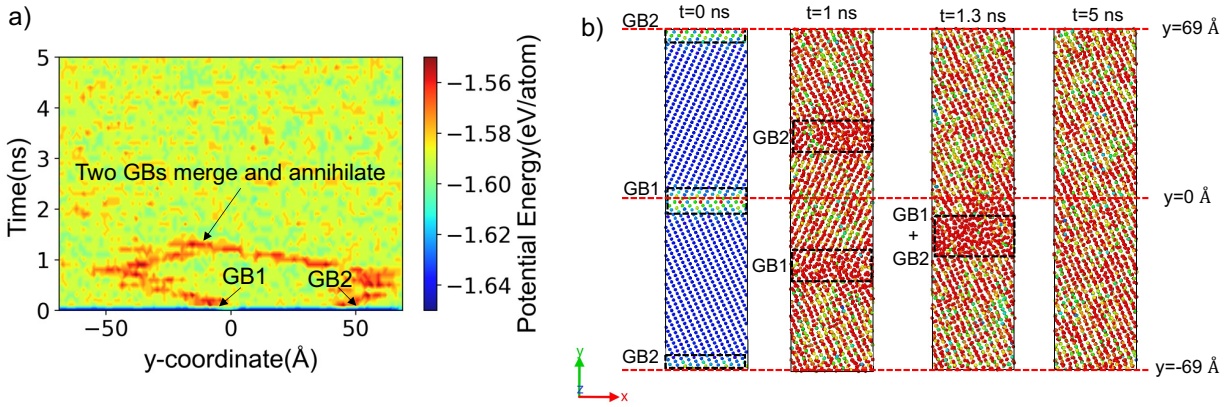

Figure 3.3 Migration of two $\Sigma 11(311)/[01\text{-}1]$ tilt GBs and their subsequent annihilation during NPT annealing at 400 K. a) Color map showing the GB locations vs time based on the atomic potential energies. b) Snapshots during NPT annealing at selected times. Red indicates high potential energy and blue represents low potential energy.

10 Å wide regions centered at fractional positions y = 0.25 and 0.75. (The GB planes are located at y = 0 and y = 0.5.) Motion in the x and z directions was not constrained, as shown in Figure 3.4.

Following the annealing process, 5 ns of NPT MD was performed at 1 atm and at one of four target temperatures: 250K, 300K, 350K, or 400K. This was followed by 1 ns of NVT equilibration and a 5 ns NVT MD production run for the purpose of calculating diffusivity. Snapshots of all atom positions were dumped every 0.1 ns for postprocessing. To quantify statistical uncertainties in the simulations, 3 distinct MD production runs were performed with different initial velocity distributions.

The mean squared displacements (MSD) of atoms within the GB regions were used to calculate the GB self-diffusivity. In prior studies of GB diffusion, the MSD of atoms in/near the boundary was calculated by tracking displacements in a fixed region (e.g., 10 Å) surrounding the boundary.[59,65,66] This approach assumes that the GB position does not change significantly during the MD run, and that the width of the GB can be defined in a consistent fashion.

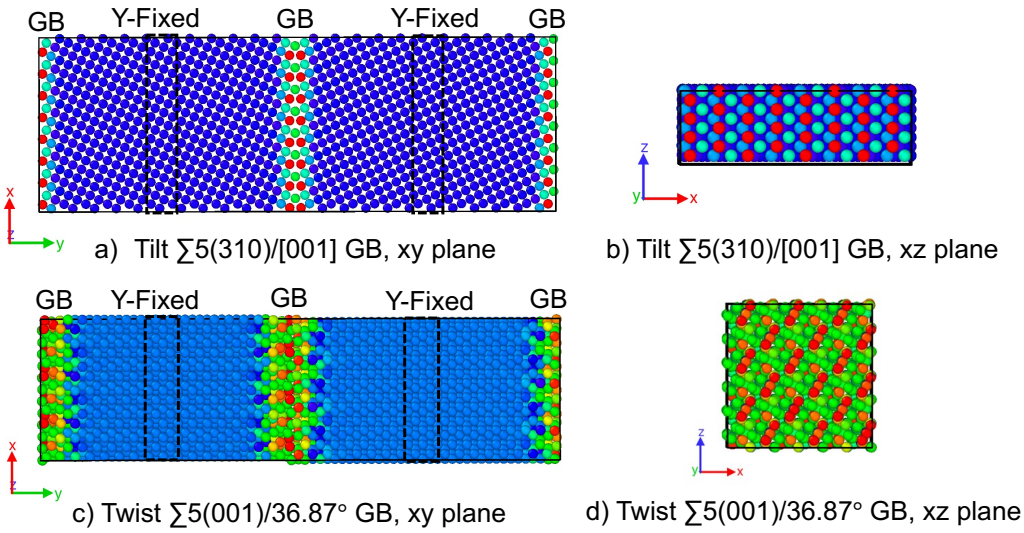

Figure 3.4 Simulation cells for ∑5(310)/[001] tilt and ∑5(001)/θ=36.87 twist grain boundaries (viewed along two viewing directions) as determined by g-surface calculations. Atoms are colored based on their potential energy, with red (blue) corresponding to highest (lowest) energy. Black-boxes indicate regions where the atom displacements are constrained in the y-direction during MD.

However, as illustrated in Figure 3.3, displacements of some GBs are observed during MD, especially at higher temperatures, even with constraints applied to atoms in the bulk regions.

To address these issues, an automated scheme was developed to track the position and width of the GBs. As a first step in the procedure, each simulation cell was partitioned, at 0.1 ns intervals, into 100 bins along the y-direction (50 bins were used for smaller simulation cells). The average potential energy of the atoms in each bin was calculated and plotted as shown in Figure 3.5(a). These plots of potential energy vs. position exhibit two peaks that are associated with the two GB regions. Next, the peaks were fit to a Gaussian function, and the width measured at 25% of the peak height was adopted as the GB width. (Table A.5 tabulates the widths of all GBs at finite temperatures.) This procedure was repeated at 0.1 ns intervals in NVT MD and allows for the calculation of the MSD within a region centered on the instantaneous

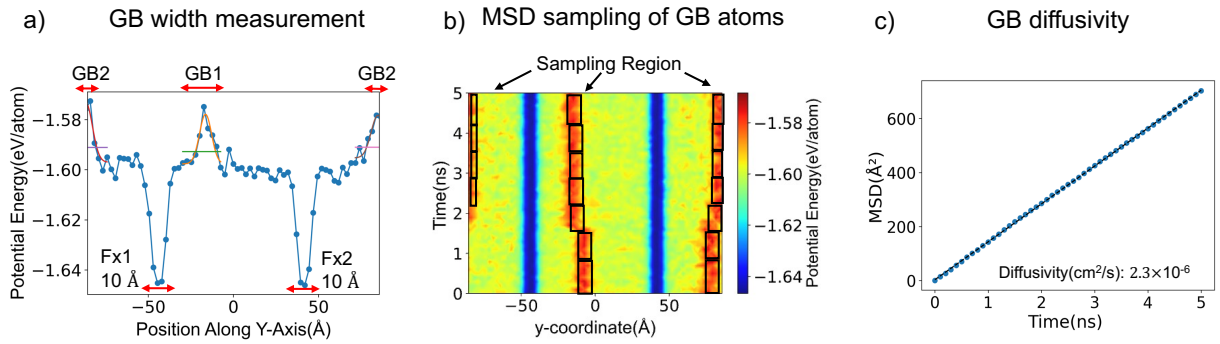

Figure 3.5 Methodology to sample mean squared displacements of atoms within the GB region of a ∑33(811)/[01-1] GB. a) Determination of the GB location and width at an arbitrary time during MD. GB positions correspond to maxima in the planar-averaged potential energy with respect to position normal to the GB plane. GB width is calculated by fitting Gaussians to these maxima. b) GB positions visualized during 5 ns of MD. Regions of low potential energy (blue) correspond to atoms in the bulk region with fixed y-coordinates. Black boxes indicate the instantaneous location of the GB region. c) Calculated mean squared displacements of GB atoms at 350 K.

location and width of the GB, Figure 3.5(b). (Use of a smaller sampling interval of 0.01 ns did not significantly change the results, Figure A.1.) Afterward, the MSD was calculated using Eq 3.2.

$$\text{MSD} = < x^2(t) + y^2(t) + z^2(t) > \tag{3.2}$$

Figure 3.5(C) shows an example MSD plot for a ∑33(811)/[01-1] GB. Subsequently, the MSD values were averaged over all time origins by increasing the reference time t from 0 to t_{max}-Δt, where t_{max} is the maximum simulation time (5 ns), and Δt is the maximum diffusion time window, taken as 1 ns. MSD plots constructed using this moving window approach are presented in Tables A.6-A.7. Finally, the diffusivity of Li atoms in the GB region was calculated by performing a linear fit to the MSD data and applying the Einstein relation, Equation 3.3.

$$\text{MSD} = 6\bar{D}t \tag{3.3}$$

To draw comparisons to the bulk, the diffusivity in body-centered cubic Li was also evaluated. These calculations were performed in a BCC simulation cell containing 1999 atoms and one vacancy. This system was annealed and equilibrated in the same fashion as done for the

GB systems. MSDs were collected and bulk diffusivities were predicted at 250K, 300K, 350K, and 400K. These diffusivity values were then scaled to account for the non-equilibrium vacancy concentration used in the simulations. The equilibrium vacancy fraction is given by equation 3.4, where E_v^f is vacancy formation energy, and C_v^{eq} is equilibrium vacancy fraction:

$$C_v^{eq} = \exp\left(-\frac{E_v^f}{K_B T}\right) \tag{3.4}$$

For an equilibrium concentration of vacancies, the bulk diffusivity, D_{eq}, can be obtained from equation 3.5[75,76,]

$$D_{eq} = \frac{C_v^{eq}}{C_v^*} D^* \tag{3.5}$$

where C_v* and D* denote, respectively, the non-equilibrium vacancy fraction used in the simulations and the diffusivity predicted by MD. D_{eq} was adopted as the bulk diffusivity and was used below to estimate the polycrystalline diffusivity.

It is highly likely that a realistic lithium metal anode will be polycrystalline. A small number of models exist for predicting the diffusivity of a polycrystal under differing assumptions. The Hart model[51,52] assumes that the GB planes and the diffusion are parallel. This scenario may be realized if the grains adopt a columnar structure.[53,54] The Maxwell-Garnet 1D model[52,56] assumes that the GB slabs are normal to the diffusion direction. The 2D grain model[52] uses a mixture of GB orientations, in which half of the GB planes are parallel to the diffusion direction, and the other half are perpendicular (See Figure 2.1). Lastly, Chen's model[58] is examined which assumes 1) bulk grains are enclosed by GBs and triple junctions (TJs), 2) TJs isolate the neighboring GB facets, and 3) grains are assumed to have the Voronoi polyhedral shape and log-normal size distribution. These models are compared in Figure 3.11. There, it can be seen that the Hart, 2D grain, the Chen (with $D_{TJ}=10^2 D_{GB}$ assumption) models yield

comparable results, while the 1D Maxwell-Garnett model yields diffusivities similar to that for a single crystal (as expected). Given the similarity in the predictions between the Hart, Maxwell-Garnet (2D, 3D), 2D grain, and Chen models, and experimental evidence suggesting that some electrodeposited Li films exhibit columnar grains with diameters on the order of microns, [53,54] the Hart equation was adopted in this study to model polycrystalline diffusivity, $D_{Polycrystal}$, equation 3.6.[51,52]

$$D_{Polycrystal} = fD_{GB} + (1-f)D_{Bulk} \tag{3.6}$$

Here f is the volume fraction of GBs in the Li anode, and D_{GB} and D_{Bulk} are the self-diffusivities of the GB and bulk regions, respectively. The GB volume fraction, f, was calculated using the regular polygon model,[55] Equation 3.7, where w is the representative GB width at each temperature, and d is the grain size.

$$f = 1 - (1 - \frac{w}{d})^2 \tag{3.7}$$

The GB width, w, at each temperature was calculated by averaging all GB widths for a given temperature. This was predicted to be in the range of 10.9-15.3 Å as shown in Table A.5. The grain size, d, was an input variable ranging from 10^{-2} to 10^{3} μm.

Lastly, the Li polycrystalline self-diffusivity was used as input to a mesoscale model of Li anode stripping during the discharge of a LMSSB. The time and space-dependence of the Li concentration in the anode during stripping was modeled using Fick's 2nd law, Equation 3.8.

$$\frac{\partial C}{\partial t} = D\frac{\partial^2 C}{\partial x^2} \tag{3.8}$$

Several prior studies[23,24,61,77] have employed Fick's 2nd law to describe Li transport in the anode. For example, in the work of Zhao et al[78], Fick's law was used as one of the governing equations in a phase field model of void evolution at the Li/SE interface. In the study of Jow et al[61]., Fick's

2nd law was used to determine the diffusivity within a Li anode interfaced with a LiI(Al_2O_3) solid electrolyte.

Equation 3.8 was solved assuming: a constant stripping rate at the SE interface (x = 0), a uniform initial Li concentration equal to that of bulk Li, no stack pressure, and a zero-flux condition at the boundary opposite of the interface (x = L, i.e., at the current collector). (See the section 2.3.4 for additional details.) The general solution to this model, developed by Jow et al, is given by Equation 3.9[23,61].

$$C(x,t) = C_o - \frac{2It^{1/2}}{FD^{1/2}} \sum_{n=o}^{\infty} \left[ierfc \frac{2(n+1)L-x}{2(Dt)^{1/2}} + ierfc \frac{2nL+x}{2(Dt)^{1/2}} \right] \quad (3.9)$$

3.3 Results and Discussion

3.3.1 Grain Boundary Energies

Plots of grain boundary energy (GBE) as a function of misorientation angle are presented in Figure 3.6. The plots compare the GB energies obtained before and after simulated annealing. Several features of these data are of note. First, GBs generally exhibit energies that are only slightly smaller after annealing. This indicates that the GB structure obtained from the gamma-surface search is a relatively stable (local) minimum on the potential energy surface. Second, the GBEs, as predicted by prior DFT calculations,[79] are larger than those predicted in the present study, although both methods exhibit similar trends. We hypothesize that the lower energies reported here reflect the extensive search performed over the configuration space. A similar search with DFT would be more challenging to conduct due to its greater computational cost. Third,

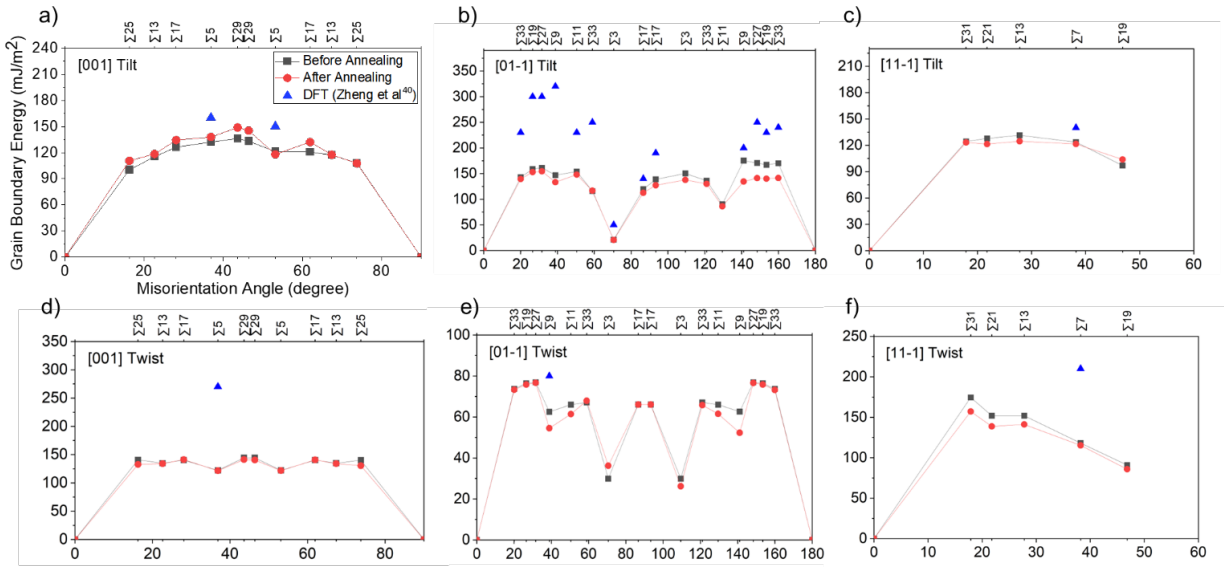

Figure 3.6 GB energy before/after annealing as a function of misorientation angle. a) [001] tilt b) [01-1] tilt c) [11-1] tilt d) [001] twist e) [01-1] twist f) [11-1] twist rotation axis. The Σ-values of the coincidence site lattice are listed at the top axis of each plot. Recent energies calculated from DFT are shown for comparison.[79]

several cusps in the GB energies appear in the plots, with notable examples including ∑5(210) 53.1°, ∑9(411) 38.9°, ∑3(211) 70.5°, ∑11(233) 129.5°, ∑9(01-1) 38.9°, and ∑3(01-1) 70.5°. This behavior is consistent with previous studies of GB energy trends in BCC metals[80,81]. The low energies of these GBs suggest that they will have a greater probability of appearing in polycrystalline systems that are close to equilibrium.[82]

3.3.2 Grain Boundary Diffusivity

Figure 3.7 shows Arrhenius plots of Li diffusivity for all GBs studied. For comparison, the calculated bulk diffusivity and measured polycrystalline diffusivity[83] are also shown. Compared to the bulk diffusivity, GB diffusivities are predicted to be 3 to 6 orders of magnitude larger. This result aligns with previous work[65–67] which reported faster GB diffusion in metals. In addition, the measured polycrystalline diffusivity falls

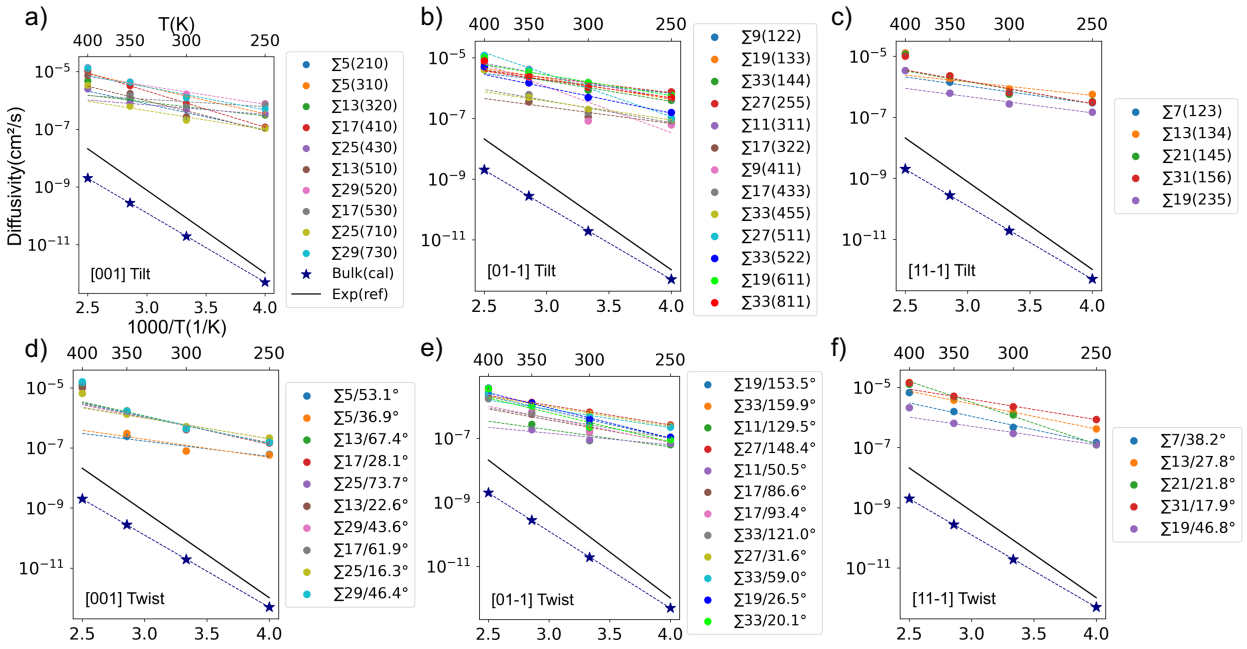

Figure 3.7 Calculated GB diffusivities for a) [001] tilt, b) [01-1] tilt, c) [11-1] tilt, d) [001] twist, e) [01-1] twist, and f) [11-1] twist GBs. For comparison, the calculated bulk diffusivity and experimental polycrystalline diffusivity[83] are shown with stars and as the solid black line, respectively.

between that of the bulk and GBs. This is reasonable given that diffusion in a polycrystalline metal should be a combination of diffusion involving GBs and the bulk.

The activation energy for GB diffusion was calculated by performing separate linear fits to the diffusivity data at the 3 low temperatures (i.e. 250K, 300K, 350K) and at the 3 high temperatures (i.e. 300K, 350K, 400K), Table A.9-A.10. Two fits were performed to account for an apparent change in slope near 400 K; this approach yielded better agreement with the data than the use of a single fit. At low temperatures, the calculated GB activation energies range from 0.1 to 0.3 eV. These values are smaller than the calculated value for bulk diffusion, 0.48 eV, (which includes the vacancy formation energy), and thus explains the higher mobility of atoms in the GB region.[45–49,50,51]

The bulk activation energy measured by experiments[84–88] is 0.52-0.57 eV, and DFT calculations report values of 0.58-0.59 eV[89,90]. A commonly used rule-of-thumb regarding GB diffusion in alkali metals is that the energy barrier for GB diffusion is 60-67% of that for bulk diffusion.[91,92] According to this rule, the GB activation energy would be approximately 0.3 eV. Hence, this rule underestimates the GB diffusivity.

The GB activation energies at high temperatures fall in the range of 0.2 to 0.4 eV, suggesting a different diffusion mechanism compared to low-temperature diffusion. Prior studies[65,93–95] have reported that pre-melting can occur at GBs – i.e., a disordered phase forms in the GB region at temperatures below the bulk melting temperature. Accordingly, it is hypothesized that the change in activation energy above 400K results from pre-melting. To test this hypothesis, the pair distribution function (PDF) was evaluated for atoms in the GB region. Figure 3.8 compares the PDF for bulk Li and for 6 representative GBs at different temperatures. In the bulk, a liquid-like distribution is calculated above 500K. On the other hand, in the GB PDFs, a liquid-like distribution is detected at 400 K, in support of pre-melting.

The pre-melting hypothesis was also verified by calculating the centro-symmetry (CS) parameter of the GBs as a function of temperature, Figure 3.9. The CS value[50] measures the local lattice disorder. The CS parameter equals zero for a site surrounded by the undistorted lattice; it assumes non-zero values when the surrounding lattice is disordered. In the idealized BCC lattice, all neighboring atoms are symmetrically arranged around a given atom. In contrast, an asymmetrical environment exists near defects, resulting in non-zero CS values. For reference, a centro-symmetry value of ~8 was measured in the dislocation core of BCC Fe[96] and values larger than 8 were reported

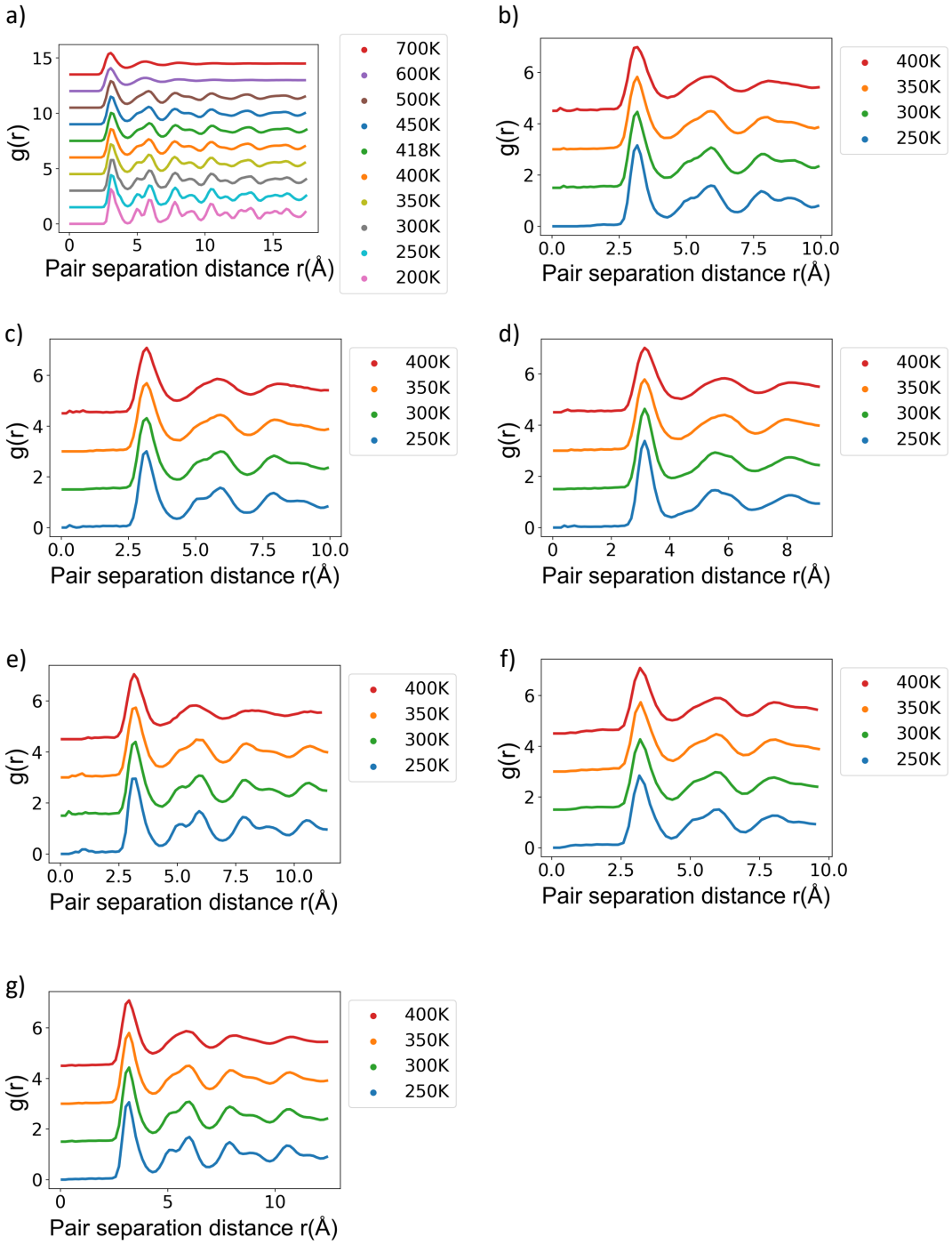

Figure 3.8 Pair distribution functions (PDFs) of 6 randomly chosen Li GBs compared to that of bulk Li. a) bulk Li, b) ∑5(210)/[001] tilt, c) ∑11(311)/[01-1] tilt, d) ∑31(156)/[11-1] tilt, e) ∑5(001)/53.13° twist, f) ∑11(01-1)/50.48° twist, and g) ∑13(11-1)/27.8° twist GBs. GB PDFs at 400 K are similar to that of melted bulk Li. (The melting temperature of the force field is 418 K.)

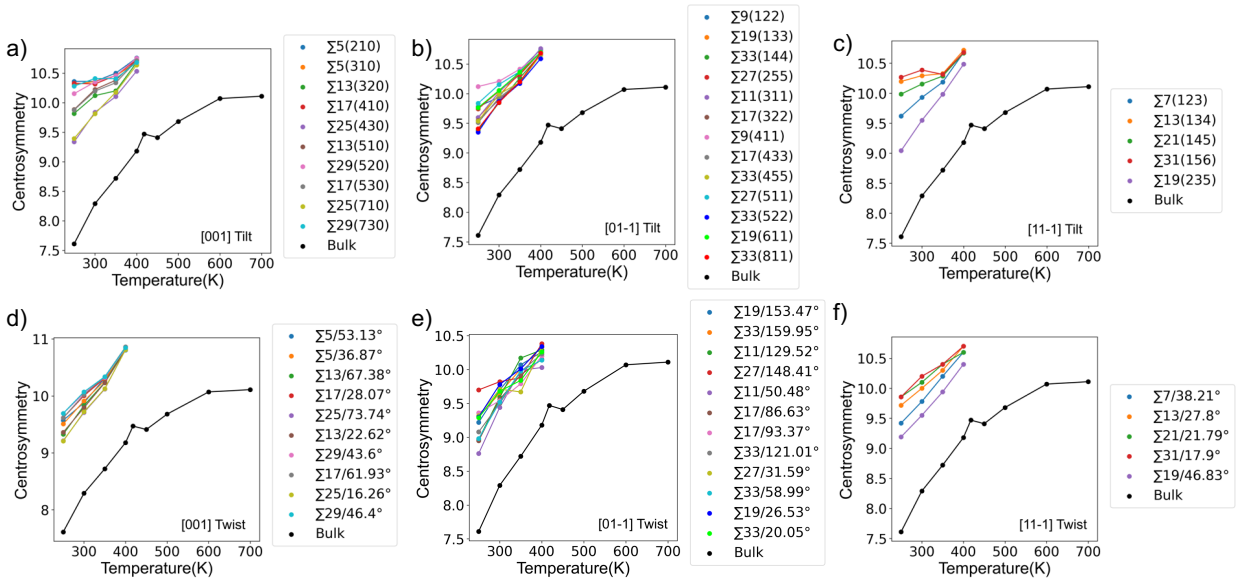

Figure 3.9 Calculated centrosymmetry parameter for 6 Li GBs: a) [001] tilt, b) [01-1] tilt, c) [11-1] tilt, d) [001] twist, e) [01-1] twist, and f) [11-1] twist rotation axes. For comparison, the centrosymmetry values for bulk Li is shown as the black line in each plot.

in BCC-Fe twin boundaries[97]. According to Figure 3.9, the CS values of the Li GBs examined here are larger than that of the bulk. This is consistent with the GB region being intrinsically more disordered. Moreover, the values of the CS parameter for different GBs tend to converge to a similar value as the temperature is increased from 250K to 400K. This result also supports the pre-melting at 400K; at this temperature the distinct crystalline features of GBs diminish as a similar disordered, liquid-like phase emerges.

Figure 3.10a compares: (i) the largest diffusivity (ii) the average diffusivity of the three GBs exhibiting the largest diffusivities, (iii) the average diffusivity of the three GBs exhibiting the smallest diffusivities, (iv) the average diffusivity computed across all GBs, (v) the smallest diffusivity, and (vi) the bulk diffusivity. From this data, it is evident that an order of magnitude separates the diffusivities of the fastest and slowest GBs. For example, at 300K, the ∑31(11-1) 17.9° twist, the ∑29(520) tilt, and the ∑11(311) tilt GBs are predicted to exhibit the fastest

diffusivities of 2.3×10^{-6} cm^2/s, 1.7×10^{-6} cm^2/s, and 1.6×10^{-6} cm^2/s, respectively. Whereas the ∑9(411) tilt, the ∑5(001) 53.1° twist, and the ∑5(001) 36.9° twist boundaries are predicted to exhibit the slowest diffusivities of 8.4×10^{-8} cm^2/s, 8×10^{-8} cm^2/s, and 8×10^{-8} cm^2/s, respectively. Comparing the average GB diffusivity to the bulk diffusivities reveals that the GB diffusivities are 3 to 6 orders of magnitude larger, depending on the temperature. The gap between the average GB and bulk diffusivity becomes smaller at higher temperatures, reflecting the larger activation energy associated with bulk diffusion.

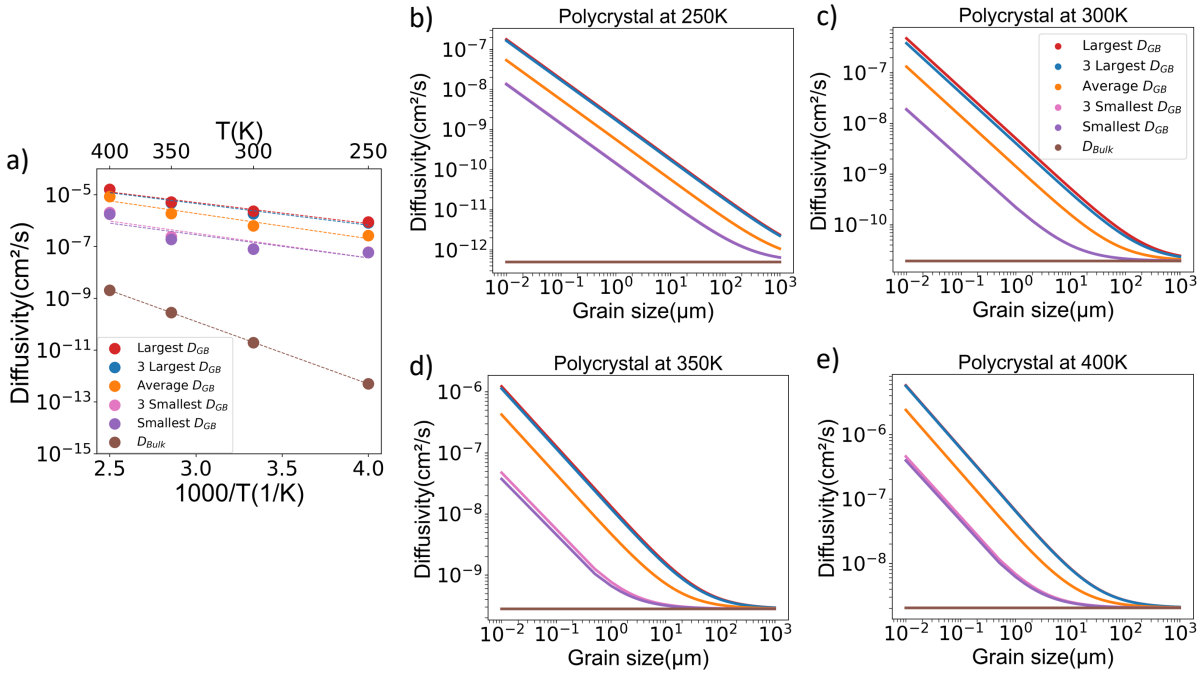

Figure 3.10 a) The largest and smallest, the average of 3 fastest, overall GBs, and 3 slowest GB diffusivities vs inverse temperature. Polycrystalline diffusivity (Eq. 3.6) as a function of grain size at b) 250 K c) 300 K d) 350 K e) 400 K. Here "Largest," "Smallest," etc refers to the range of D_{GB} shown in panel a).

3.3.3 Polycrystalline Diffusivity

Polycrystalline diffusivity is estimated using the GB diffusivity data shown in Fig. 3.10a and equation 3.6. Figures 3.10b-3.10e illustrate the upper and lower bounds as well as average

values for $D_{Polycrystal}$ as a function of temperature and grain size. The calculated polycrystalline diffusivity is in good agreement with recent experimental measurements. Assuming a 150 μm grain size at 300K, $D_{polycrystal}$ is computed to be 2.9×10^{-11}cm^2/s, whereas for grains "of the order of 100 μm" Siniscalchi et al. reported diffusivities of 3.9×10^{-11} and 1.6×10^{-10}cm^2/s at room temperature.[25] This agreement is reasonable given the uncertainties in grain size distribution, dislocation density, and the presence of impurities.

Fig. 3.10b-3.10e show that the polycrystalline diffusivity increases as the grain size decreases. This trend reflects the faster diffusivity predicted for GBs, and the greater volume fraction occupied by GBs as the grain size decreases. For example, Figure 3.10c shows that Li diffusivity can be increased from ~10^{-11} to ~10^{-7} cm^2/s at 300K by reducing the grain size from 1 mm to 10 nm. The increase in mobility due to smaller grain size is more pronounced at low temperatures. At 250K, decreasing the grain size from 1 mm to 10 nm results in an increase in $D_{polycrystal}$ from ~10^{-12} to ~10^{-8} cm^2/s. At 400K, a similar change in grain size results in a smaller increase of only two-orders-of-magnitude, from ~10^{-8} to ~10^{-6} cm^2/s.

Wang et al[19] reported a diffusion coefficient for Li-ions in the solid electrolyte LLZO at room temperature of 2.15×10^{-9} cm^2/s. This diffusivity is much faster than the self-diffusivity for Li metal reported by Jow et al,[61] $5.6*10^{-11}$ cm^2/s. Hence, Wang et al argued that slower diffusion in the Li anode may be an important factor in determining the critical current density (CCD) for dendrite formation in solid-state Li metal batteries. The data in Figure 3.10 suggests that $D_{polycrystal}$ can be increased by several orders of magnitude by reducing the Li grain size, and thus, the transport properties of the Li anode may not be the rate-limiting factor.

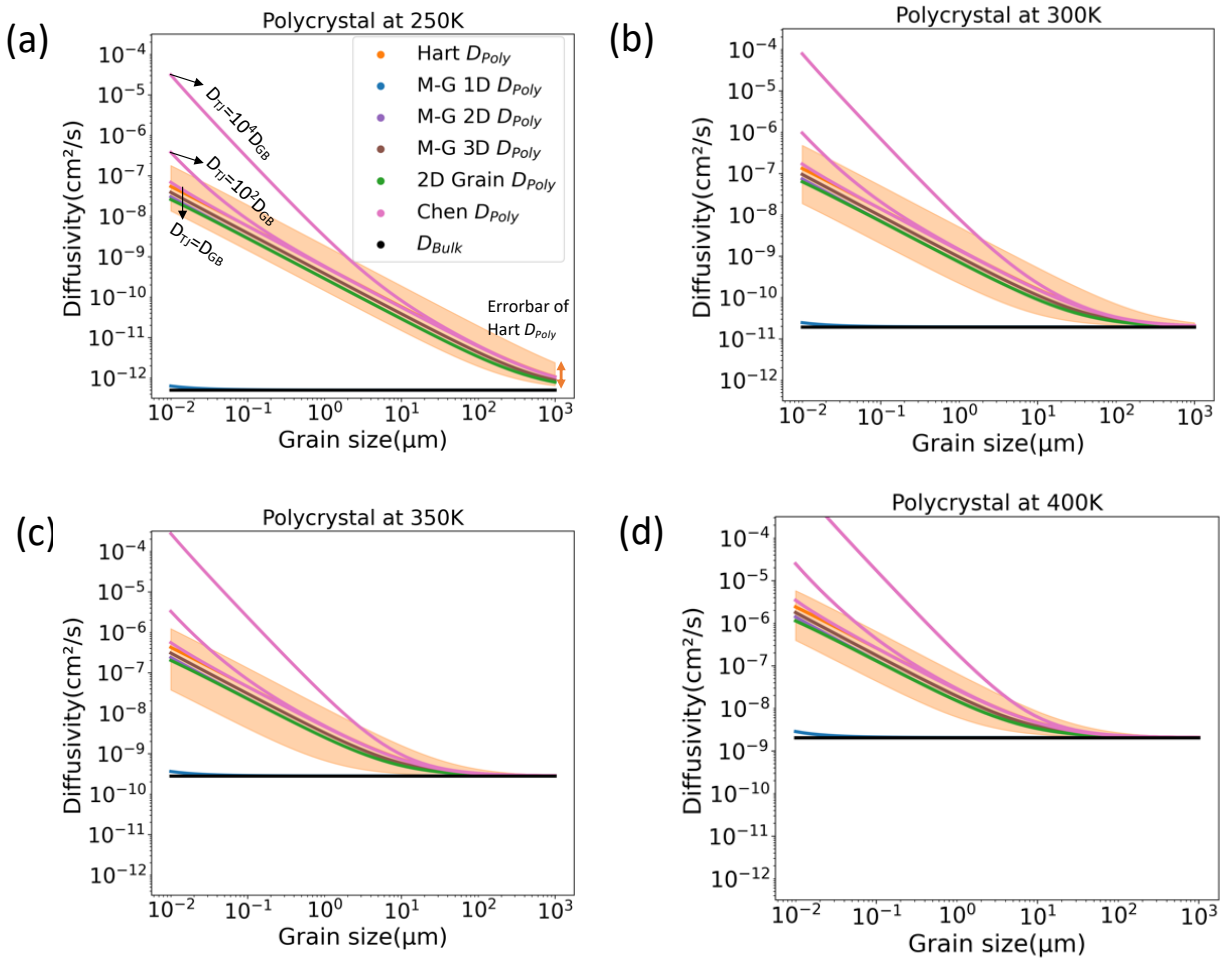

Figure 3.11 Li Polycrystalline diffusivity as predicted by 3 models that make different assumptions about GB orientation. The Hart model, Maxwell-Garnet model, 2D grain models are used to predict the polycrystalline diffusivity at (a) 250K, (b) 300K, (c) 350K, and (d) 400K, respectively. The calculation results of the Hart model are shown with the orange line, those of the Maxwell-Garnet models are shown with blue, purple, brown lines, the Generic 2D grain model with a green line, and the Chen model with pink lines. 3 different pink lines correspond to different assumptions on the triple-junction diffusivity. The orange shaded area represents the range of polycrystalline diffusivities from the Hart model, assuming scenarios where the largest and smallest GB diffusivities are used, respectively, as inputs to that model.

The $D_{polycrystal}$ in Figure 3.10 is estimated with the Hart model using equation 3.6. However, the prediction can vary depending on the assumptions on the GB orientations relative to the diffusion direction within the Li polycrystalline (Figure 2.1). The diffusivities estimated by different polycrystalline models are compared in Figure 3.11. The result in plots displays that the prediction of the 2D grain model and Maxwell-Garnet $d^{'} = 2$, 3 models are similar to those of the Hart model across the range of diffusivities observed for the different GBs. In case of Chen's

model, as the diffusivity in Li triple junctions (D_{TJ}) is not available, 3 different assumptions are made on D_{TJ} and compared; D_{TJ} is D_{GB}, or 10^2 D_{GB}, or 10^4 D_{GB}. Results show that up to $D_{TJ} = 10^2$ D_{GB}, except at the 10^{-2} μm grain size, polycrystalline diffusivities are within the error-bar range of the Hart model; Given that D_{TJ} is estimated to be faster than D_{GB} by a factor of 2-10 in Cu,[59] it is speculated that D_{TJ} is smaller than 10^2 D_{GB} is a reasonable approximation. Also, the experimental characterizations observed a columnar structure in electro-deposited Li.[53,54] Therefore, in the present study, we exploited the Hart model in the following meso-scale simulations.

3.3.4 Diffusion Length

As previously discussed, during discharge the rate of Li stripping from the Li anode surface can exceed the rate of Li self-diffusion in the bulk of the anode, resulting in void formation at the interface. In principle, void formation could be minimized by pausing cell operation between charge and discharge half-cycles; this "replenishment time" could allow Li diffusion to reduce the roughness of the Li surface. This strategy was investigated by Kasemchainan et al[18], who included ~30-minute pauses between half-cycles of a Li/Li_6PS_5Cl/Li symmetric cell.[7] To verify whether such a ~30 minute pause is sufficient, a rough estimate of the diffusion length in polycrystalline Li can be obtained from Equation 3.10, where t is the diffusion time.

$$L = \sqrt{D_{polycrystal} \times t} \tag{3.10}$$

Figure 3.12 plots the diffusion length, L, as a function of grain size and time at 300 K. Assuming a grain size of 150 μm and t = 30 minutes, the predicted diffusion length is 2.3 μm.

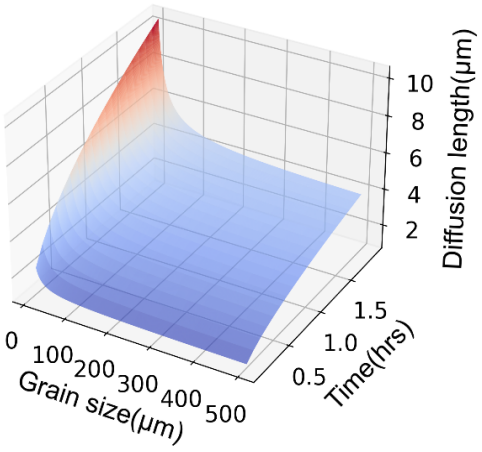

Figure 3.12 Diffusion length as a function of grain size (μm) and time (hrs) at 300K.

For comparison, the targets for capacity from a Li anode range from 3 to 5 mAh/cm^2,[20] which corresponds to a minimum Li thickness of 15 – 25 μm. Hence, the diffusion length under these conditions is a small fraction (9-15%) of the desired anode thickness. In the experiments of Kasemchainan et al, a thinner anode with a thickness of 5 μm was used.[18] Nevertheless, this thickness still exceeds the diffusion length by more than a factor of two for a 30-minute rest period. Therefore, increasing the replenishment time and employing strategies to reduce the grain size are proposed as opportunities to improve performance.

3.3.5 Battery Design Guidelines

The calculated polycrystalline diffusivity can be used to estimate the maximum discharge capacity as a function of discharge current, Li grain size, and anode thickness. More importantly, this data allows one to estimate the ranges of grain size and anode thickness that satisfy various performance goals.[20,98]

As mentioned earlier, during discharge it is desirable for the diffusional flux of Li atoms within the anode to be comparable to the rate at which Li is stripped. When Li diffusion is slower than the stripping rate, the concentration of Li atoms at the interface can decrease, resulting in roughening of the anode surface, void formation, and loss of contact between the anode and solid electrolyte. The time at which this contact loss occurs (relative to the start of the discharging half-cycle) is referred to in the literature as the "depletion time," t_d[24,61]. The depletion time determines the upper bound of the deliverable capacity, and is a function of the discharge rate, anode thickness, and Li grain size. Here, t_d was calculated in 1D by solving Fick's 2nd law for the Li concentration in the anode, Equation 3.9. Using the notation in Eq. 3.9, at $t = t_d$, $C(x = 0, t = t_d) = 0$.

The validity of this model was assessed by comparing its predictions with the experiments of Krauskopf et al[17]. That study examined stripping in a Li/LLZO/Li symmetric cell with a 120 μm thick Li anode. The cell was discharged at 0.1 mA/cm^2 and no stack pressure was applied. Since no information on the Li grain size was reported, a nominal value of 150 μm is assumed here. Such a value appears to be representative of the grain size for purchased Li foil.[99] Applying the present computational model to this scenario, delamination is predicted at $t_d = 36$ hours from the start of stripping, while the experimentally measured depletion time from Krauskoph et al. was 12 hours. Given the 1D nature of our model, coupled with the lack of information regarding grain size and the initial state of the Li/LLZO interface, this is an acceptable agreement between theory and experiment.

Figure 3.13 illustrates Li concentration profiles in the anode as a function of anode thickness under the operating conditions used by Krauskoph et al. As discharge progresses, the initially uniform interfacial Li concentration decreases, with the most rapid decreases in

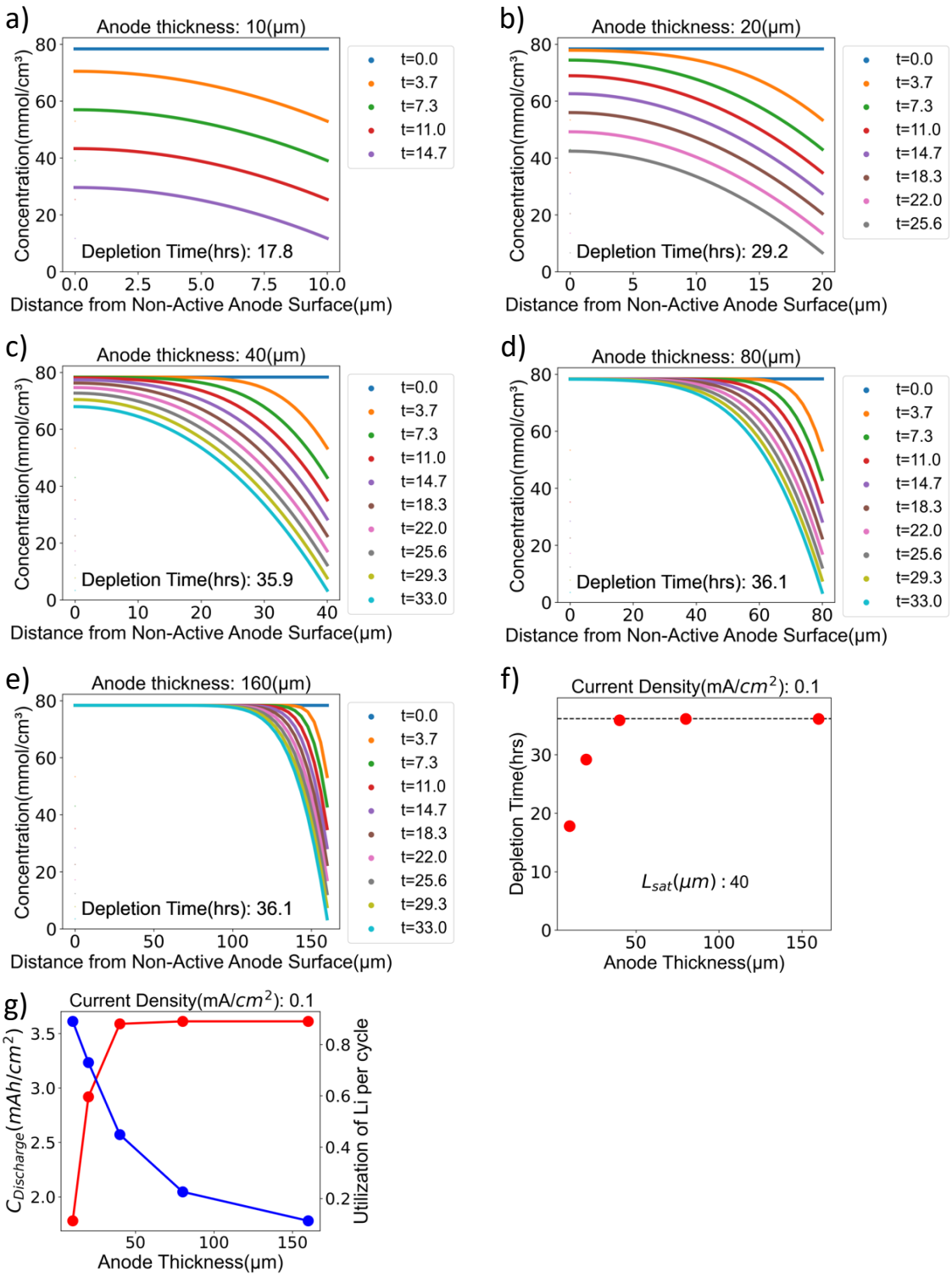

Figure 3.13 Concentration profiles for Li anodes during discharge as a function of time and anode thickness. The grain size is assumed to be 150 μm, with a stripping current density of 0.1mA/cm^2. Anode thickness include a) 10μm, b) 20μm, c) 40μm, d) 80μm, and e) 160μm. The depletion time as a function of anode thickness is plotted in f); the discharge capacity and Li utilization fraction as a function of anode thickness are plotted in g).

concentration occurring near the SE interface. Eventually, the concentration of Li at the interface goes to zero (at time t = t_d), resulting in contact loss and an open circuit (i.e., a cessation of discharge). The maximum discharge capacity is the product of the stripping current and t_d. For the conditions simulated here, and for anode thicknesses up to 40 μm, t_d increases as the anode thickness increases, resulting in a larger discharge capacity. However, increasing the anode thickness beyond 40 μm does not increase the maximum discharge capacity. Beyond 40 μm thicknesses, t_d plateaus at a value of approximately 36 h, with a corresponding capacity of 3.6 mAh/cm^2. Thus, for the present combination of grain size and current density, the achievable capacity for anodes of thickness less than ~40 μm is limited by the thinness of the anode and the inability of Li self-diffusion to compensate for Li-stripping. In contrast, for anode thicknesses greater than 40 μm, capacity is limited only by Li self-diffusion, Figure 3.13g. This result implies that at a given stripping current and grain size – for this example, 150 μm grains and 0.1 mA/cm^2 stripping current density – the amount of inaccessible Li can be minimized by tuning the anode thickness, which in this case corresponds to a thickness of 40 μm.

Figure 3.14 illustrates the achievable discharge capacity as a function of stripping current density, Li grain size, and the anode thickness. The maximum discharge times are found by moving from right to left, and from top to bottom on each plot. This corresponds to reducing the grain size (our new solution) or decreasing the stripping current (the trivial solution). The percentage of accessible Li exceeds 90% when the combination of current and grain size falls to the left of the largest contour line in each plot.

Various targets for solid-state batteries have been proposed.[20,98] For example, the ARPA-E IONICS program targets a minimum current density of 3 mA/cm^2, a capacity of 3 mAh/cm^2, and 80% utilization of the total Li capacity per cycle. Similarly, the fast-charging program

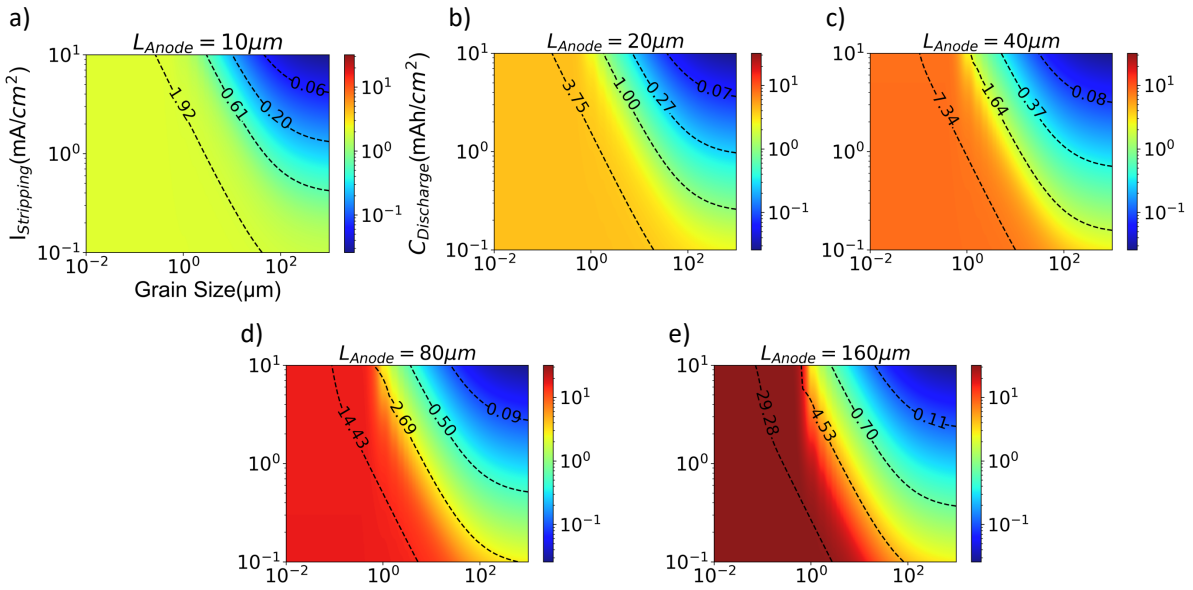

Figure 3.14 Maximum discharge capacity as a function of stripping current and grain size for Li anode thicknesses of a) 10 μm, b) 20 μm, c) 40 μm, d) 80 μm, and e) 160 μm.

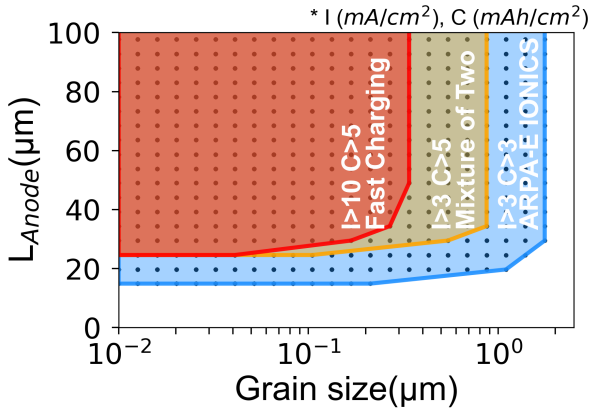

Figure 3.15 Design guidelines for capacity (C) and current density (I) based on anode thickness and grain size. Conditions that satisfy the fast-charging goal (I>10 C>5) are shown in red, those that satisfy the ARPA-E Ionics goal (I>3 C>3) are shown in blue, and those that satisfy a mixture (I>3 C>5) are orange.

targeted a Li capacity of 5 mAh/cm^2 at 10 mA/cm^2. Figure 3.15 illustrates the combinations of anode thicknesses and grain sizes that are predicted to achieve these performance targets. To meet these fast-charging targets, the present model predicts that the thickness of the Li anode (L_{Anode}) should be greater than 25 μm, while the grain size (d_G) should be less than ~0.3 μm. To

meet the IONICS targets, $L_{Anode} > 15\ \mu m$ and $d_G < 1.8\ \mu m$. Finally, as an intermediate scenario, to satisfy the fast-charging capacity goal and the IONICS current density goal, $L_{Anode} > 25\ \mu m$ and $d_G < 0.9\ \mu m$ are necessary. As expected, when the target current density and capacity are increased, the minimum anode thickness should increase and the grain size must shrink. The minimum anode thickness is bounded by the minimum capacity of each target (e.g. $L_{Anode}=25\ \mu m$ for C=5 mAh/cm^2 for the fast charging goal).

The design guidelines for a microstructural feature of Li, (i.e., grain size) can be varied because of uncertainties in GB diffusivities of a Li metal. As discussed in Figure 3.10, depending on GB structures present in a Li polycrystal, the self-diffusivity of the Li anode can change resulting in different performances of LMSSB. The required grain size above is evaluated with a mesoscale model informed with the "average" polycrystalline diffusivity at 300K (Figure 3.10c). However, when the "smallest" and "largest" polycrystalline diffusivities at 300K are used, the optimal grain size for performance targets are estimated to be $0.1\mu m$ and 3 μm respectively, as exhibited in Fig 3.16. The target Li self-diffusivity is ~10^{-9} cm^2/s, Figure 3.17. This grain size is much smaller than what has been reported in the literature for commercial Li foils, which have average grain diameters of 150 μm.[99] Hence, the present model suggests that the desired current density and capacity targets cannot be achieved with commercial, large-grained Li, where Li[99] self-diffusion is too slow to keep pace with the stripping current. This observation may explain why much recent work on Li metal anodes has employed large stack pressures (~10 MPa) or elevated temperatures to minimize dendrite formation.[17,18,23] In the former case, the application of stack pressure will induce creep deformation in the Li anode, which is another mode of Li transport that can minimize void formation at the SE interface. Similarly, the use of elevated temperatures will increase the self-diffusion of Li, resulting in reduced voiding. In principle, by

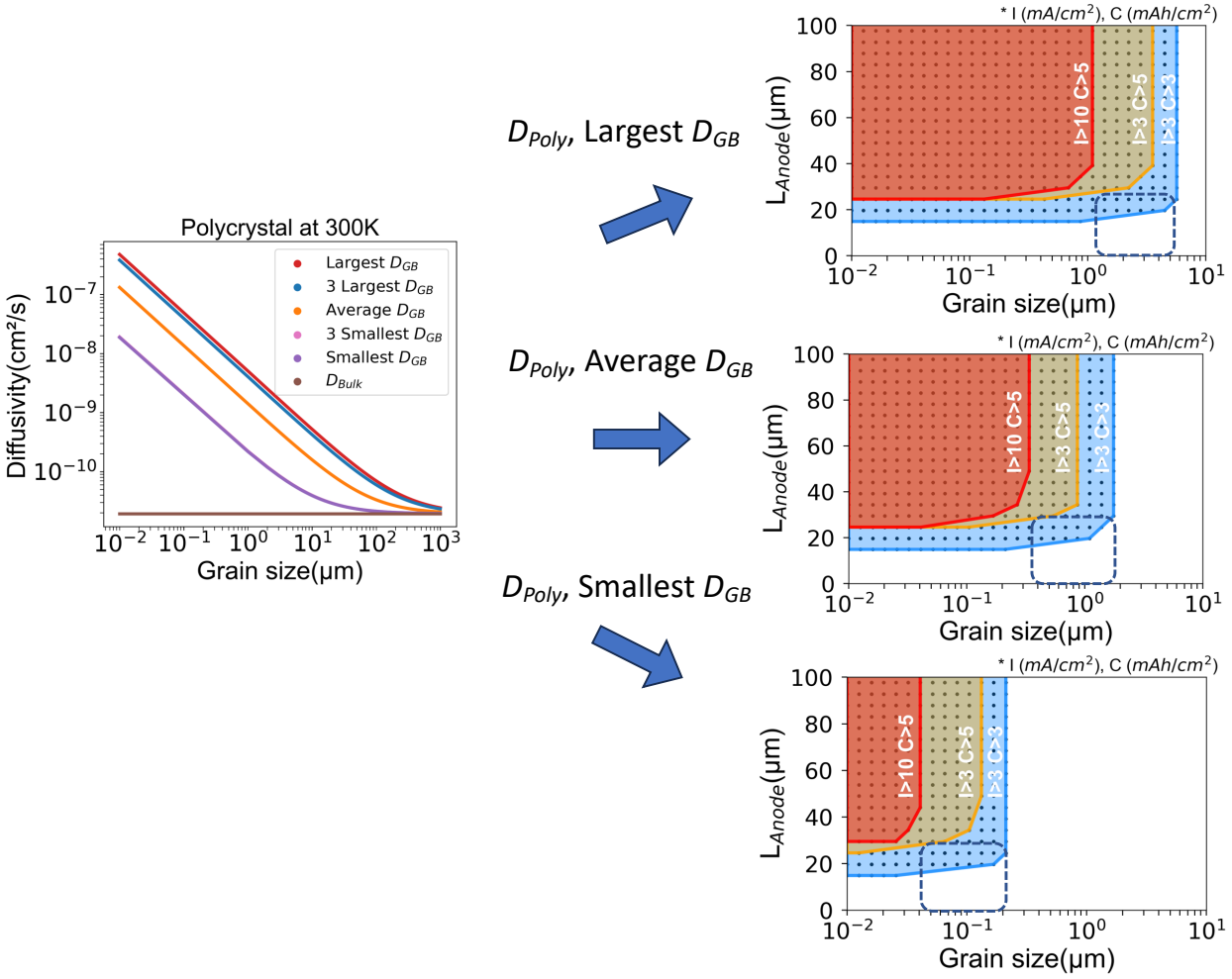

Figure 3.16 Variation in design guidelines because of the uncertainties in GB diffusivities. When the lower-bound, average, and upper-bound polycrystalline diffusivity (corresponding to smallest, average, and largest D_{GB}) are used for the estimation, the required grain sizes are predicted to be approximately 0.1, 1, and 3 μm respectively.

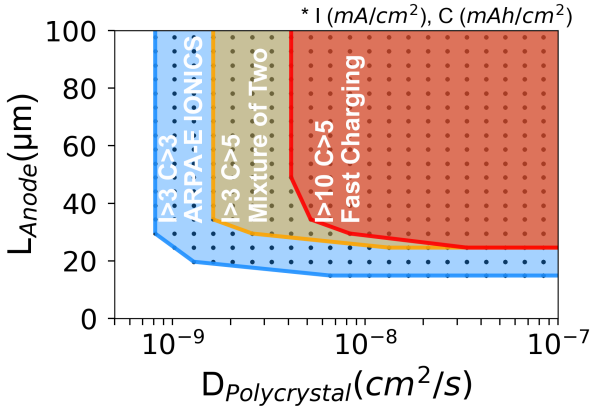

Figure 3.17 Design guidelines for Li metal anodes. Regions of different color indicate the combinations of polycrystalline self-diffusivity and anode thicknesses that satisfy three different battery performance goals.

controlling the grain size, the benefits of elevated temperatures or high stack pressures may be realized without incurring their respective drawbacks. For example, recent work has shown that the application of stack pressure, while helpful for void suppression, facilitates fracture of the SE.[62]

How can a micron-scale grain size be achieved in a functioning Li metal battery? Given that the Li anode is (partially) stripped and reformed during battery cycling, controlling the grain size during cycling may be difficult. Unfortunately, the grain size appears to be an overlooked property of the anode; very few studies report Li grain size distributions or discuss how the grain size varies with initial processing conditions or with the current density used during cycling.[53,54,71,100,101] Recent work has shown evidence of Li being electrodeposited in the form of columnar grains with micron-sized grain diameters.[53,54] Such a geometry would maximize the diffusion of Li atoms along GBs to the SE interface.

In principle, several potential strategies exist for controlling grain size, even in the context of plating/stripping. For example, it is known that the electro-deposition process itself can generate small-grained morphologies. Ni alloys that are electrodeposited in the fabrication of micro-electro-mechanical systems (MEMS) exhibit grain sizes on the nano-scale.[102,103] Nevertheless, it is not currently known if Li behaves similarly to Ni when electrodeposited during battery operation. Secondly, templating effects may also be exploited. This strategy requires that the initial Li anode be fabricated with a small grain size, and that some fraction of the Li be retained upon stripping (i.e., the anode is not fully stripped). The remaining, small-grained Li would then act as a template during subsequent charging/plating, encouraging the newly-plated Li to mimic the microstructure of the substrate.[104] Finally, controlling the rate of charging could also be helpful in maintaining a small grain size. The rapid deposition of Li (i.e.,

fast charging) will increase the number density of Li nuclei, resulting in smaller grain sizes. If uniformly high plating currents are not practical, brief pulses of high current density could be interspersed between longer periods of plating at more moderate rates. This latter approach combines the aspects of the templating strategy with the concept of enhancing the density of Li nuclei. Additional experimental analysis of the microstructure of the Li anode and its potential impact on cell performance would undoubtedly be helpful in clarifying these issues.

In closing, it is important to recognize the limitations of the present model. First, the model estimates the depletion time using a one-dimensional approximation. Voiding and loss of contact at the Li/SE interface are, however, three-dimensional phenomena. These phenomena could be captured more realistically by kinetic Monte Carlo or phase field techniques,[78,105] especially if these models were parametrized using the transport properties predicted here. Second, as the model assumes a cell under no stack pressure, Li redistribution from plastic deformation is not captured. Third, the model accounts only for bulk and GB diffusion of Li. Diffusion along surfaces and along dislocation cores may also be important but are not accounted for here. Finally, the model treats vacancies as non-interacting particles, and thus does not account for potential vacancy clustering. Consequently, several avenues exist for extending the model. Despite these limitations, the model is qualitatively consistent with existing experimental data. It also provides an experimentally testable design suggestion – that smaller grain sizes are advantageous in the operation of Li metal batteries.

3.4 Conclusion

Minimizing void formation in the Li metal anode is a key challenge in developing Li metal-based solid-state batteries. Void formation results in a reduction in the interfacial contact area, which focuses the Li-ion current during plating to a reduced number of contact points. This phenomenon generates high local current densities during plating, which can nucleate dendrites.

The present study proposes a strategy for minimizing void formation based on exploiting fast GB diffusion within the anode. By decreasing the grain size of the metallic anode, the volume fraction of grain boundaries will be increased, resulting in a greater contribution of GB diffusion to mass transport within the anode.

Molecular dynamics simulations were used to calculate diffusion coefficients for a diverse sampling of 55 tilt and twist GBs in Li. GB diffusion was found to be 3 to 6 orders of magnitude faster than in the bulk. Using these atomic-scale data as input, a meso-scale model of Li depletion in the anode during discharge was developed. Although limited to 1-D, the model is qualitatively consistent with experimental data. Importantly, the model allows for the development of design and operation guidelines for LMSSBs by linking the Li grain size, discharge current density, anode thickness, and achievable capacity.

The model predicts that grain sizes of approximately 0.1-3 μm are needed to meet performance targets for LMSSBs. These grain sizes are two orders of magnitude smaller than those in common use. Strategies for controlling the grain size in a battery environment where the anode undergoes plating and stripping are discussed.

In total, the model highlights the importance of the anode's microstructure on the performance of LMSSBs. It also presents an alternative to the use of high pressures in controlling void formation in LMSSBs.

Chapter 4 Pipe Diffusion Rates and Deformation Maps for Li Metal Anodes From Atomistic Simulations

4.1 Introduction

In the development of LMSSB, a challenging issue is the formation of undesirable dendrites during cycling, which can lead to a failure of a battery. Previous studies[17,106] have reported that maintaining the contact between Li metal anode and solid electrolytes (SE) during stripping is critical to prevent dendrite initiation; Because it determines the uniformity of the current density at the Li/SE interface during subsequent plating. Therefore, many efforts have been made to balance the diffusional flux of Li^0 atoms within the Li anode and the Li^+ ion flux in SE during stripping. For example, Krauskopf et al[17] estimated the critical anodic current bounded by the maximum diffusional flux of Li vacancy, so stripping can happen while the Li anode maintains good contact with SE. In the work of Tsai et al[23], dendrite-tolerant solid-state batteries were demonstrated by improving the morphological stability of a Li anode at the Li/SE interface by raising the temperature and self-diffusion rate of the metallic anode. In our previous study[107], we proposed that by increasing the GB density and exploiting fast diffusions in the GB region, the self-diffusivity of Li polycrystal can be raised, and a larger discharge capacity is accessible at the high current density; however, the kinetic contribution of dislocations was not considered in the simulation of a Li dissolution, and thus, it left room for a future study.

Another approach to maintain the Li/SE interface in LMSSB is to induce creep in Li metal by applying a stack pressure. Under compressive loading, the plastically deformed Li

anode has been confirmed to retain good contact with SE during stripping, and to increase the cell performance.[22,92,108] In addition, many studies have been performed to understand the creep behavior of Li metal anode in the cell. Masias et al[109] performed tensile tests to measure the time-dependent deformation of Li, and revealed that dislocation-climb is the dominant creep mechanism. The work of Raj[92] demonstrated that reducing Li grain size can change the prevailing creep mechanism at the same stress and temperature. For example, when Li is under the 0.1Mpa at 25°C, the grain size reduction from 100 μm to 1 μm will convert the power-law creep to boundary diffusional creep; and the strain rate will increase from ~10^{-8} to ~10^{-4} (1/s). While these studies extended the understanding of Li creep, the lack of transport properties of Li metal linked with its microstructure still bounds our predictions on the creep behavior. Several studies[107,110–112] have investigated Li defects, but to our knowledge, there is no available data for dislocation self-diffusivity.

In the present study, multiscale simulations of Li transport are performed to minimize the dendrite formation in LMSSB. First, the self-diffusion rate of low-energy edge and screw dislocations of Li are measured by molecular dynamics simulations and a Kim et al's 2NN MEAM interatomic potential.[113] More accurate measurement is performed by regularly updating the sampling region of dislocation atoms in Li during MD. The transport data of Li dislocation are combined with the self-diffusivities of Li grain boundary(GB) and bulk from our previous study.[107] When compared, the Li diffusion in dislocations is confirmed to be 2-5 orders of magnitude faster than in bulk (consistent with dislocation diffusivity studies for metals[114–118]); but dislocation diffusivity is predicted to be comparable with or ~1 order slower than the diffusion in the GB. Subsequently, the polycrystalline diffusivity of Li is predicted as a function

of dislocation density and grain size. The estimation shows that by tuning the defect concentrations, Li self-diffusivity can be enhanced by several orders of magnitude.

Atomistic transport properties are used to parameterize the mesoscopic model based on Fick's 2nd law. This model calculated the maximum discharge capacity as a function of stripping current, dislocation density, grain size, and anode thickness. The model reveals that ~1μm grains and ~10^{11}/cm^2 dislocation density can satisfy the performance targets of the advanced lithium metal solid-state battery. Lastly, the plastic deformation map of Li is constructed using the atomistic data and constitutive equations. The map indicates that in fine-grained Li, GB sliding and coble creep will become the main mechanisms, and GB diffusion will govern the plastic deformation.

4.2 Methods

For accurate modeling of dislocation atoms movement and interactions, 2NN MEAM interatomic potential[113] is used. By extending interaction range of MEAM to 2nd nearest-neighbors, this potential successfully reproduced fundamental physical properties of pure Li, including bulk modulus, vacancy formation/migration energy, surface energy, specific heat etc. First, an edge dislocation is created at the center of the supercell by joining two-half crystals, top and bottom in the y direction, where the above one has an extra plane inserted mid-way through the crystal. The supercell has periodic boundaries in the x, y, and z direction, where the z axis is aligned with <1-21> dislocation line, and x and y axis are parallel to the <111> and <-101> crystallographic orientation, respectively. In this setup, x-axis is in parallel with the burgers vector of BCC Li $\frac{1}{2}$<111>. Subsequently, the cell is relaxed with conjugate gradient method, and the final structure is shown in Figure 4.1. A screw dislocation is constructed by anisotropically

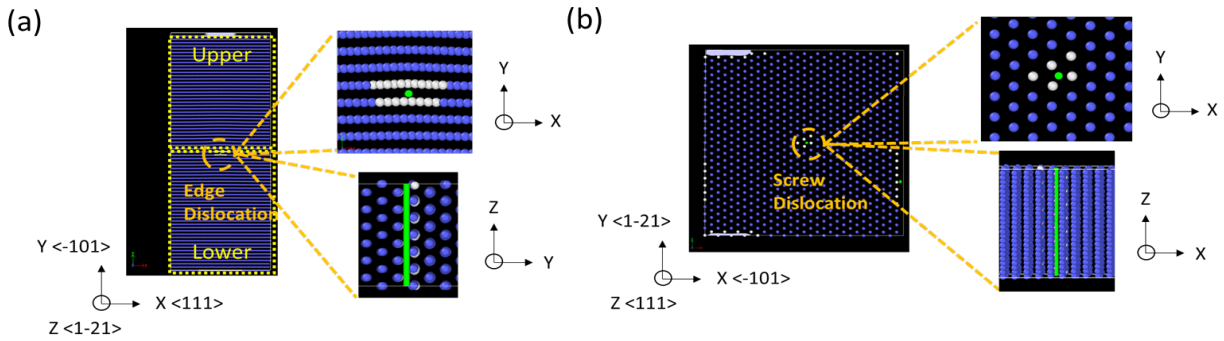

Figure 4.1 The visualization of dislocations in the simulation cell before being input to dynamics calculation. A green line at the center of the simulation cell represents a dislocation pipe. (a) edge and (b) screw dislocation is shown respectively.

straining the cell such that atoms are arranged in a helical pattern along the z-axis at the center of the cell[119]. The x, y, z axes are set to be parallel with <-101>, <1-21>, <111> facet of the lattice, respectively, where z is the burgers vector direction.

Afterwards, the as-prepared structure is expanded by thermal expansion coefficient at four different target temperatures 250K, 300K, 350K, and 400K, to minimize the thermal stress during dynamics at each target temperature. And then, as depicted in Figure 4.2, a cylindrical model is adopted such that atoms within the cylindrical region bounded by 70Å diameter are cut out of the supercell incorporating a dislocation at the center. During dynamics, to reduce the dislocation migration from the center, atoms within 5Å thick outer layer of the cylinder are fixed. Later, all atoms in the dynamic region (excluding fixed atoms) are set to the canonical ensemble (NVT), and temperature is controlled by Nose-Hoover thermostat. After a series of NVT heating and equilibration for a total of 10 ns, subsequent 5ns NVT equilibration is conducted at the target temperature. At this step, atomic positions are output to dump files every 0.1ns, and used for post-processing. Figure 4.3 displays the flow chart of MD simulation steps.

To calculate the dislocation diffusivity, the dislocation “pipe” needs to be first defined, and atoms within such region are required to be identified. In this study, the dislocation region

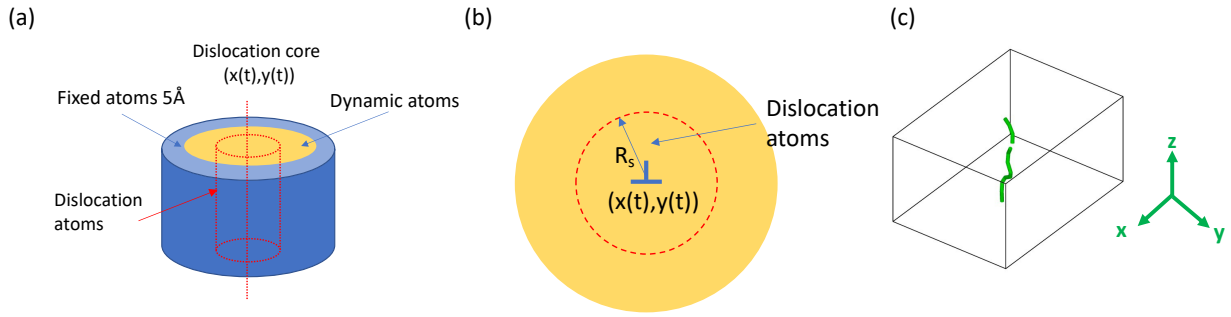

Figure 4.2 The schematic of cylindrical model for NVT simulation and dislocation core measurement. (a) The region of dynamic atoms with a 70Å-diameter cylinder is bounded by 5Å thick fixed atoms region. At the center of the cell, a dislocation is located. (b) During NVT simulation, the position (x(t),y(t)) of the dislocation core is measured using OVITO[120] every 0.1ns. Rs denotes the radius of the dislocation pipe. (c) Green line in the example snapshot represents the dislocation core extracted out of the simulation cell using OVITO.

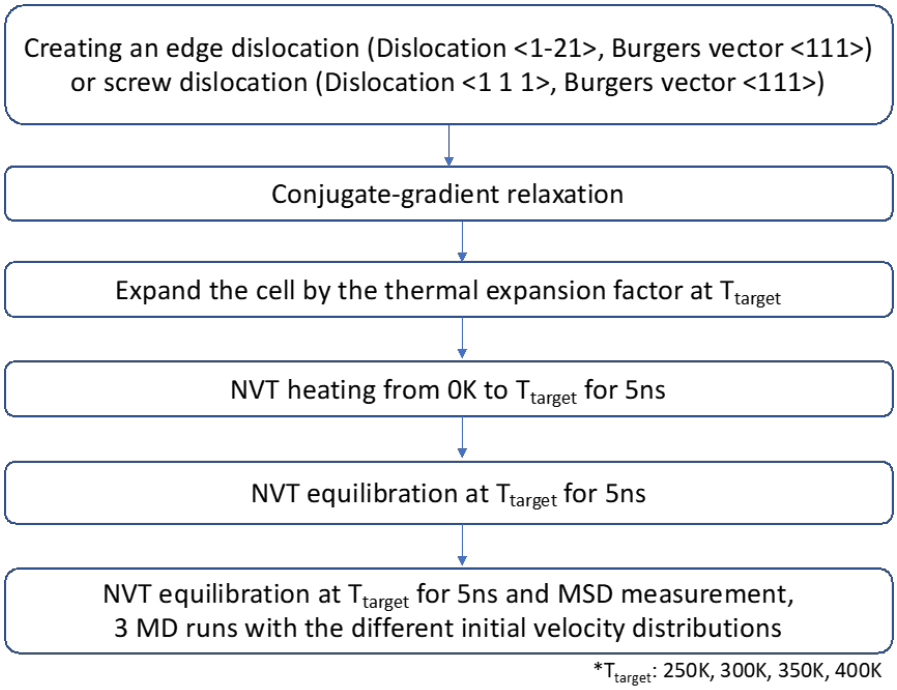

Figure 4.3 Flow chart describing the procedure for calculating dislocation diffusivity.

in Li is characterized using OVITO software equipped with Dislocation Extraction Analysis (DXA)[120]. It is possible to extract a series of 1D representations of dislocation core from dump

file snapshots using DXA. And then, by averaging the x and y coordinates of dislocation segments, the axial position of the dislocation pipe (x(t), y(t)) is identified every 0.1ns. Subsequently, by setting sampling radius R_s, and tracing all atoms inside the dislocation pipe defined with (x(t), y(t)) and R_s, the mean-squared displacement (MSD) of dislocation atoms is measured as a function of time. This regular update in a group of dislocation atoms is performed to enhance the accuracy of dislocation diffusivity. Diffusivity is calculated from the Einstein formula, $D_{Dislocation} = \frac{1}{6t} < x^2(t) + y^2(t) + z^2(t) >$, such that all x, y, z components of MSD are considered.

Dislocation diffusivity can vary as a function of sampling radius R_s. As seen in Figures 4.4a and 4.4c, when R_s is small, the diffusivity will be at maximum as it captures the kinetics of the dislocation core. Whereas the diffusivity will continuously decrease as R_s increases because the displacements of atoms in bulk will begin to be included in the calculation. To systematically determine the boundary between dislocation and bulk atoms (*i.e.,* R_s), Purja Pun et al[121] tried several analytical forms and discovered that the Gaussian function best describes the diffusivity vs R_s. Accordingly, the authors presented that the effective dislocation diffusivity $\frac{A}{e} + B$, and the radius of dislocation pipe r_d, can be determined by fitting $D(R_s)$ vs R_s data to the equation 4.1, where A and B are fitting parameters.

$$D(R_s) = Aexp\left(-\frac{R_s^2}{r_d^2}\right) + B \tag{4.1}$$

The same approach is adopted in this study to determine dislocations' effective diffusivity and pipe radius.

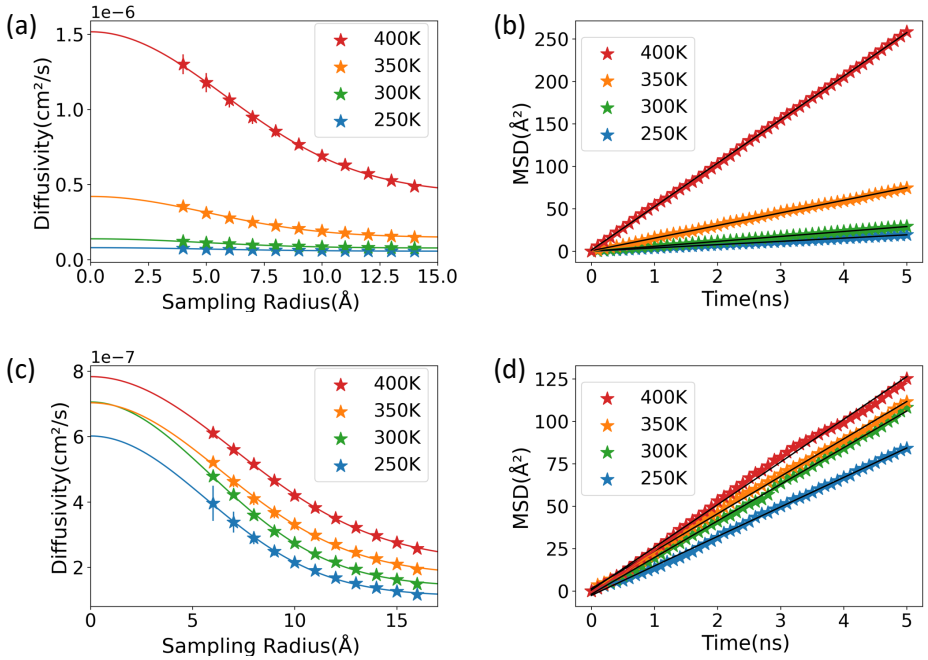

Figure 4.4 Average dislocation diffusivity as a function of sampling radius in (a) edge dislocation, (c) screw dislocation. Mean-squared displacement (MSD) at the pipe radius r_d of (b) edge dislocation, (d) screw dislocation.

The diffusivity of the Li metal anode will be contributed by Li transport in dislocations, GBs, and the bulk. In our previous work[107], both GB and bulk diffusion coefficients were calculated. In addition, it is presented that the rate of self-diffusion in Li metal can be raised by decreasing the average grain size. This is possible because GB is a fast diffusion pathway, and thus, increasing the concentration of GB defects in Li can boost the polycrystalline diffusivity. Aligned with this, next, it would be worthwhile to estimate the increase in effective volumetric diffusivity as a function of dislocation density in Li. In this calculation, only dislocations are assumed to be present in Li matrix to see the kinetic contribution of dislocations. To evaluate effective diffusivity, equation 4.2 [51] is used, where f_{Pipe} is the volume fraction of dislocations in Li, D_{Pipe} and D_{Bulk} are dislocation and bulk diffusivity at finite temperatures respectively. In particular, $f_{Pipe}$is obtained from the product of dislocation density ρ_{Pipe}, and the cross-section

area of dislocation pipe $\pi {r_d}^2$.

$$D_{effective} = f_{Pipe} D_{Pipe} + \left(1 - f_{Pipe}\right) D_{Bulk} \tag{4.2}$$

To predict the polycrystalline diffusivity, kinetic contributions of both dislocation and GB defects are considered. The weighted average of the diffusion coefficient of dislocation, GB, and bulk is calculated by equation 4.3, where f_{GB}, D_{GB} are GB volume fraction and GB self-diffusivity respectively.

$$D_{Polycrystal} = f_{Pipe} D_{Pipe} + f_{GB} D_{GB} + \left(1 - f_{Pipe} - f_{GB}\right) D_{Bulk} \tag{4.3}$$

In equation 4.3, the interaction between GBs and dislocations is assumed to be small such that kinetic contributions from both defects can be superposed to estimate the polycrystalline diffusivity.

Lastly, the Li polycrystalline diffusivity was used as an input parameter for mesoscale simulations of Li dissolution process in LMSSB. The evolution of time-dependent concentration of Li atoms in the anode of LMSSB is evaluated using equation 4.4, Fick's 2nd law.

$$\frac{\partial C}{\partial t} = D \frac{\partial^2 C}{\partial x^2} \tag{4.4}$$

Equation 4.4 is solved with two flux boundary conditions (BC) and one initial condition (IC) to physically model the stripping of LMSSB at the constant current density, and the details of them are explained in Figure 2.4. Equation 4.5 is the analytical solution of Fick's 2nd law under the given BCs and Ic[23,61], where I is current, t is time, x is position, D is polycrystalline diffusivity, L is anode thickness, and F is Faraday constant.

$$C(x,t) = C_o - \frac{2It^{\frac{1}{2}}}{FD^{\frac{1}{2}}} \sum_{n=o}^{\infty} \left[ierfc \frac{2(n+1)L - x}{2(Dt)^{\frac{1}{2}}} + ierfc \frac{2nL + x}{2(Dt)^{\frac{1}{2}}} \right] \tag{4.5}$$

4.3 Results and Discussion

4.3.1 Defect Formation in Dislocations

In Figure 4.5, contour plots exhibit defect formation energy in the vicinity of edge and screw dislocations. Here, the formation energies are measured at all available defect sites on a plane of specific z-height in the simulation cell. Because all atoms in each atomic row sitting at the same x and y coordinates are identical in our structure, the computation of one per row is enough. As the formation energy of a bulk interstitial is measured to be so high, the x-y range of energy plots of interstitials is narrowed down to the dislocation core. According to the contour map, the lowest formation energy is predicted in the vicinity of a dislocation, consistent with the fact that dislocation is a source of defects[119]. In particular, in comparison with screw dislocation,

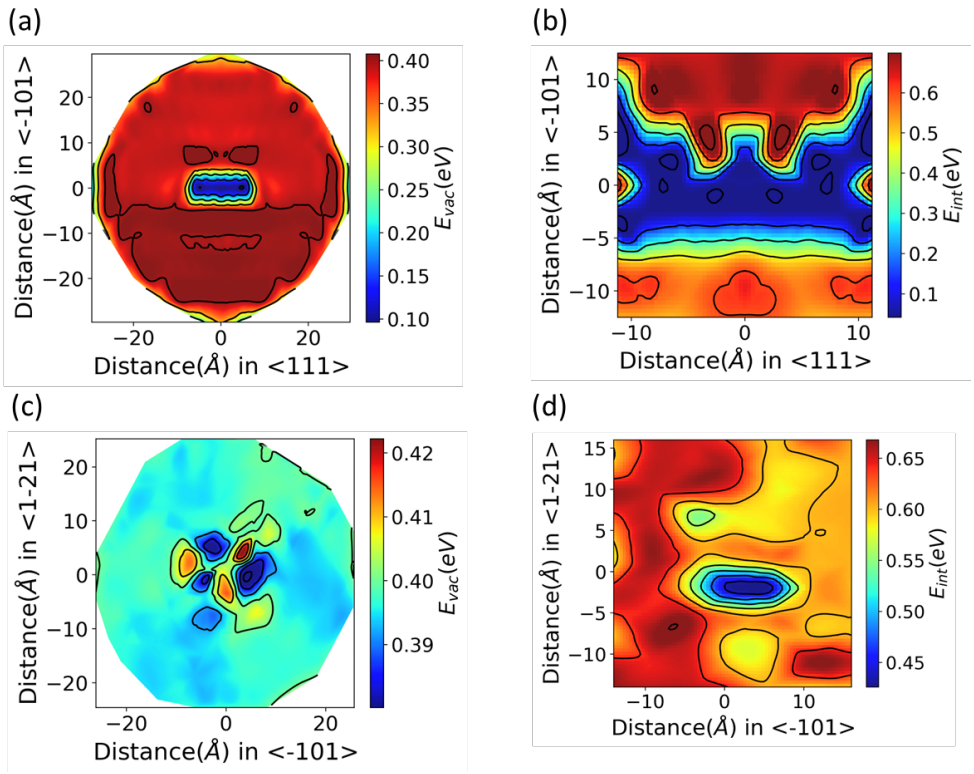

Figure 4.5 Contour energy plot of the (a) vacancy formation, (b) interstitial formation in the vicinity of edge dislocation. Energy plot of the (c) vacancy formation, (d) interstitial formation near a screw dislocation. The dislocation line is normal to the page and located at the coordinates x=0 and y=0.

a more significant drop in the formation energy is observed in the edge dislocation core, indicating that more defects can be generated. The lowest energy site identified in this analysis is further used to run the NVT simulation of dislocations with a pre-existing defect in the later section.

4.3.2 Dislocation Diffusivity

In Table 4.1, the effective diffusivity and pipe radius of dislocations are presented. Similar to Purja pun's finding,[121] diffusivity data are confirmed to be well fit to the Gaussian curve with an R-squared value close to the unity. The correlation between temperature and pipe radius is predicted to be more distinct in screw dislocation than in edge dislocation. Note that between 250K and 400K, in edge dislocation, about one order difference is measured in the diffusivity, whereas less than a factor of 2 change is estimated in screw dislocation.

To put this into perspective, an Arrhenius plot and corresponding parameters are presented in Figure 4.6 and Table 4.2, respectively, where diffusivities in dislocations, GB[107], bulk[107], and polycrystal[107,122] of Li metal are all considered together. In the plot, it is clearly shown that screw dislocation has a way smaller slope than edge dislocation suggesting a lower diffusion energy barrier in screw dislocation (0.02 eV) than in edge dislocation (0.14 eV), which

(a)

	Diffusivity(cm^2/s)	Pipe Radius(Å)	R-squared
250K	$6.4*10^{-8}$	7.1	0.99
300K	$9.9*10^{-8}$	6.8	1.0
350K	$2.5*10^{-7}$	7.1	1.0
400K	$8.4*10^{-7}$	8.2	1.0

(b)

	Diffusivity(cm^2/s)	Pipe Radius(Å)	R-squared
250K	$2.9*10^{-7}$	8	1.0
300K	$3.5*10^{-7}$	8.3	1.0
350K	$3.7*10^{-7}$	9	1.0
400K	$4.3*10^{-7}$	9.9	1.0

Table 4.1 Effective diffusivity and pipe radius of (a) Edge dislocation and (b) Screw dislocation at finite temperatures. R-squared value shows how well $D(R_s)$ vs R_s are fit to Gaussian function.

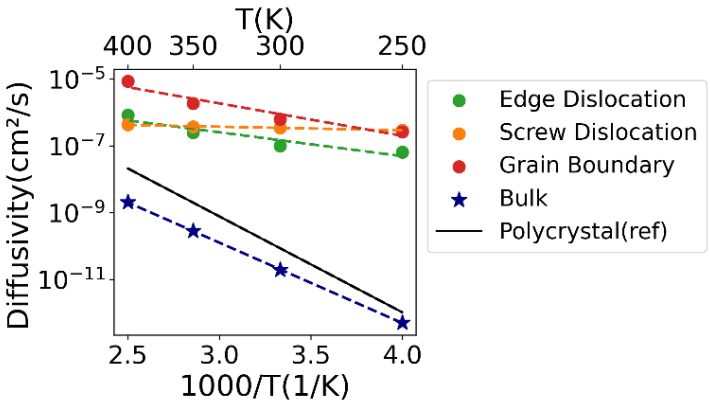

Figure 4.6 An Arrhenius plot of diffusion coefficients in edge and screw dislocations. For the comparison, GB,[107] polycrystal diffusivities[122] are added together.

	E_a (eV)	D_0 (cm²/s)	R-squared
Edge(intrinsic)	0.14	$3.6*10^{-5}$	0.81
Screw(intrinsic)	0.02	$7.8*10^{-7}$	0.96
GB	0.19	$1.5*10^{-3}$	0.81
Bulk	0.48	$2*10^{-3}$	1

Table 4.2 Arrhenius parameters of diffusivities of edge and screw dislocations, grain boundary, and bulk.

can partly account for higher diffusion rate of screw dislocation at below 400K, where the crossover in diffusivity happens. Diffusivities in dislocations are predicted to be 2-5 orders of magnitude higher than in bulk. Polycrystal diffusivity from reference is confirmed to lie between dislocation and bulk diffusivities, which is reasonable in that kinetics in polycrystals will be contributed by both dislocations and bulk. At 350K or higher, atoms in dislocation are calculated to be less mobile than in grain boundary, but at 300K or below, diffusions in both defects are predicted to be comparable.

4.3.3 Pre-existing Defect in Dislocation

When there is a pre-existing defect in the vicinity of dislocation, the mobility of dislocation atoms can change. To reveal the kinetic effect of an extra defect, additional MD studies are performed. In each dislocation, a single defect is inserted at the lowest formation energy site confirmed on the energy plots in Figure 4.5. Subsequently, thermal expansion and NVT dynamics at target temperatures are followed same as in the case of intrinsic diffusion.

Figure 4.7a exhibits that adding a defect to an edge dislocation core does not make any difference such that diffusivities in 3 different cases (*i.e.,* intrinsic, 1 vacancy, 1 interstitial) are all within the statistical error bars. As shown in Figure 4.7b, in screw dislocation, an extra defect is confirmed to only marginally affect the dislocation diffusivity. Though the slope of 1 interstitial appears to be less steep compared to the other two cases, it mainly arises from the very small activation energy of screw dislocation diffusion and non-negligible error bars of the measurement. The minor kinetic contribution of a pre-existing defect can indicate that the intrinsic diffusion is a dominant mechanism in the edge and screw dislocation of Li. This is qualitatively consistent with the lowest formation energy in a dislocation core of Li, confirmed in Figure 4.5. It is speculated that the number of defects are fluctuating near equilibrium in Li dislocations at finite temperatures.

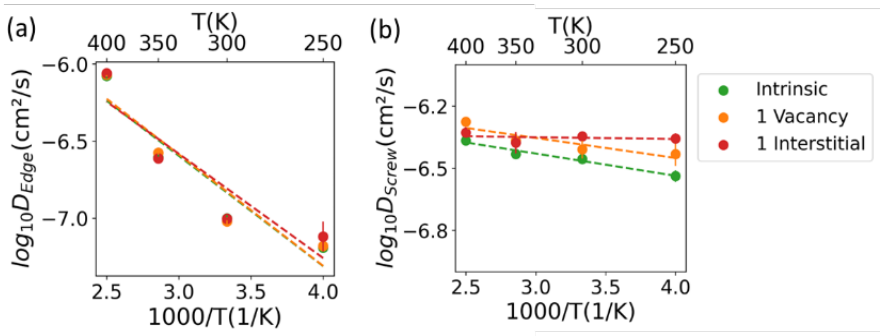

Figure 4.7 Arrhenius plot of self-diffusivity when a single defect is added to an (a) edge dislocation, (b) screw dislocation. Intrinsic diffusion denotes the case when there is no pre-existing defect in a dislocation core.

4.3.4 Polycrystalline Diffusivity

In Figure 4.8, plots portray that an increase in dislocation density by orders of magnitude raises the effective diffusivity (obtained from equation 4.2) exponentially. For instance, as presented in Figure 4.8b, a substantial increase in diffusivity is expected when dislocations are more populated than $10^9/cm^2$ at room temperature. At 250K, 300K, and 350K, a Li matrix incorporating screw dislocations is predicted to have higher diffusivity than the one with edge dislocations. But at 400K, as there is a cross-over between edge and screw dislocation diffusivities, the effective diffusivity of the edge type is higher than that of the screw type.

The $D_{effective}$ in Figure 4.8 is estimated with the Hart model using equation 4.2. However, the calculation can vary depending on the assumptions on the dislocation orientations relative to the diffusion direction within the Li single crystalline (see Figure 2.2). The diffusivities estimated by Hart model (dislocations parallel with the diffusion direction) and

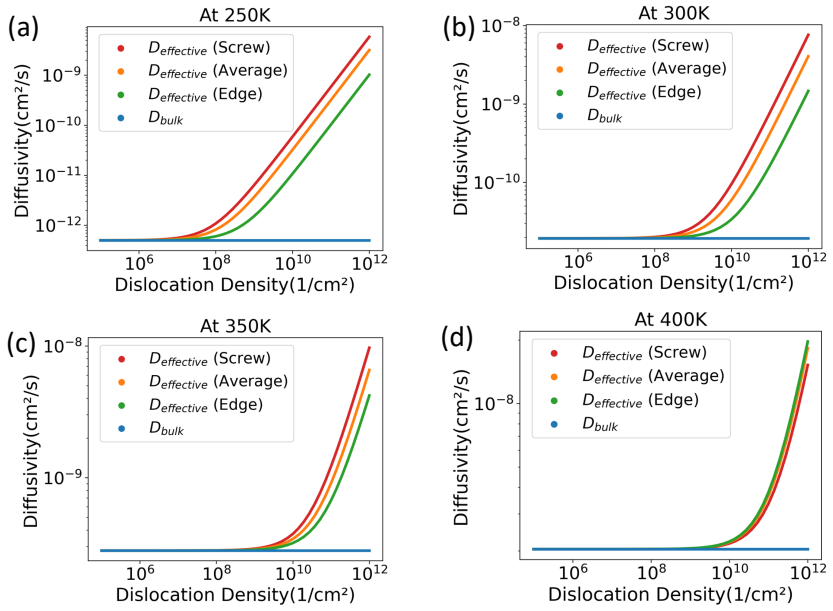

Figure 4.8 Plots of effective volumetric diffusivity as a function of dislocation density in a Li metal. Diffusivity is calculated with the Hart equation[51] for the Li metal including screw dislocations only (red curve), or edge dislocations only (green curve). Effective diffusivity is also calculated for the case when the equal contributions of edge and screw dislocation is assumed (orange curve). Bulk diffusivity (blue curve) is added as a reference.

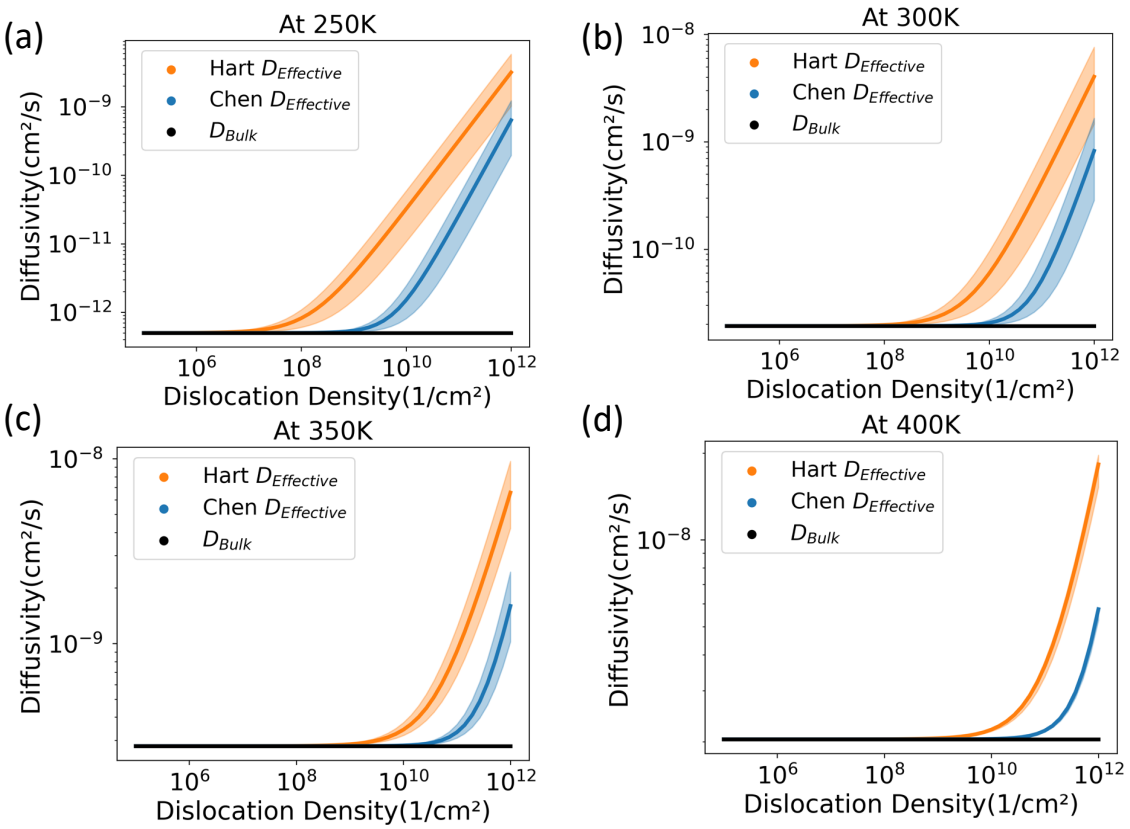

Figure 4.9 Effective volume diffusivity of Li as predicted by 2 models that make different assumptions about dislocation orientation. Plots a-d show predictions of effective diffusivity at 250K, 300K, 350K, and 400K respectively. The calculation results of the Hart model are shown with the orange line, and those of the Chen models are shown with the blue lines. The orange(blue) shaded area represents the range of effective diffusivities from the Hart(Chen) model, assuming scenarios where the largest and smallest dislocation diffusivities are used, respectively, as input to that model.

Chen's model (a 3D Frank net) are plotted in Figure 4.9. The plots indicate that $D_{effective}$ from the two models are beyond the error-bar range of each other. Therefore, for the calculation of diffusion within the granular region, both models need to be examined.

Polycrystalline diffusivities ($D_{Polycrystal}$) are estimated with two models (i.e., equation 2.28, the extended Hart model, and equation 2.31, the Chen's model), capturing the Li transport in dislocations, GBs, TJs (in Chen's model), and the bulk. Chen's model assumes more realistic microstructural features, such as a 3D network of dislocations and grains enclosed by GBs and

TJs, while the Hart model assumes dislocations and GBs parallel with the diffusion direction. Therefore, the $D_{Polycrystal}$ of the Chen's model and extended Hart model are predicted to be different. For example, as shown in Figure 4.10, at 10^{11}/cm^2 dislocation density and 150 μm grain size, the $D_{Polycrystal}$ in Hart model ($4.3*10^{-10}$ cm^2/s) is estimated to be larger than that in Chen's model ($6.0*10^{-11}$ cm^2/s). The effect of selecting different polycrystalline models on the battery design guidelines will be further discussed in the later part of section 4.3.5. But, discussions in Figures 4.11- 4.15 will be based on the Hart model prediction to focus on the enhancement of Li self-diffusivity in the anode and performance of LMSSBs.

Figure 4.11 displays $D_{Polycrystal}$ predicted by Hart model as a function of dislocation density, grain size, and temperature. In chapter 3, it is confirmed that the Li self-diffusivity is required to be on the order of 10^{-9} cm^2/s to meet the goals of advanced LMSSB, and such level could be obtained when the grain size is 0.1-3μm. According to Figure 4.11b, at 300K, when 10^{11}/cm^2 dislocations are present in a Li metal, even with grains larger than 1μm, 10^{-9} cm^2/s diffusivity is attainable. The positive z-shift of $D_{polycrystal}$ surface plot at elevated temperatures indicates that the self-diffusivity can be regulated by changing battery temperatures.

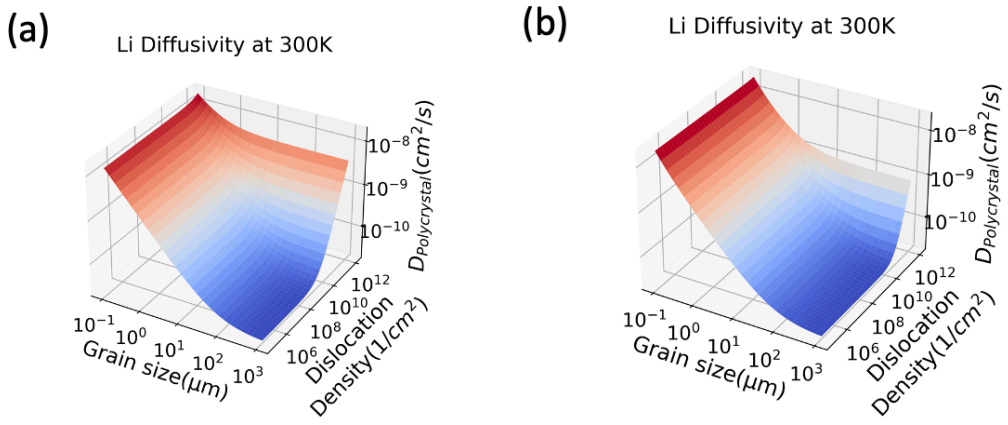

Figure 4.10 Polycrystalline diffusivity at 300K as a function of grain size and dislocation density predicted by (a) the extended Hart model, and (b) the Chen's model where D_{TJ} is assumed to be 10^2 D_{GB}.

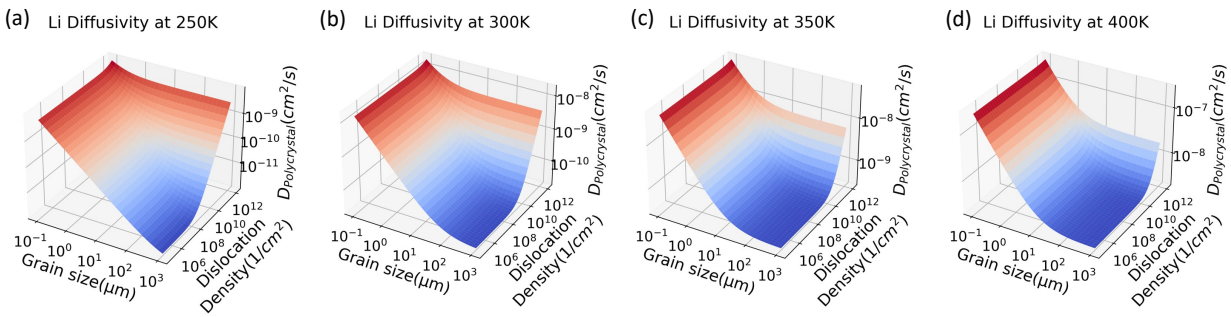

Figure 4.11 Plots of polycrystalline diffusivity at given conditions of dislocation density and grain size of a Li metal. Diffusivity is calculated with the Hart equation when kinetic contributions from grain boundaries, dislocations, and bulk are considered.

A more detailed discussion on the implication of engineering Li polycrystalline diffusivity in the development of LMSSB will be followed in battery design guidelines section.

4.3.5 Battery Design Guidelines

During the discharge of LMSSB, the flux of Li atoms in Li anode and that of Li^+ ions in SE compete at the Li/SE interface and determine morphological stability. As the mismatch between two fluxes can result in the void formation and the depletion of anode[23], it is pivotal to find the battery design parameters to prevent such kinetic discrepancy and predict the maximum discharge capacity at the given operating condition. By using equation 4.5, it is possible to measure the depletion time when the concentration at the interface becomes zero. Furthermore, from the product of the current and the depletion time, we can calculate the maximum discharge capacity at the given operating parameters.

At 300K, the discharge capacity of LMSSB is calculated at various combinations of stripping current, dislocation density, grain size, and anode thickness, which is displayed in Figure 4.12 and Figure B.1. First, it is confirmed that when the stripping current is high, and dislocation density is low, only limited portion of the Li anode can be discharged.

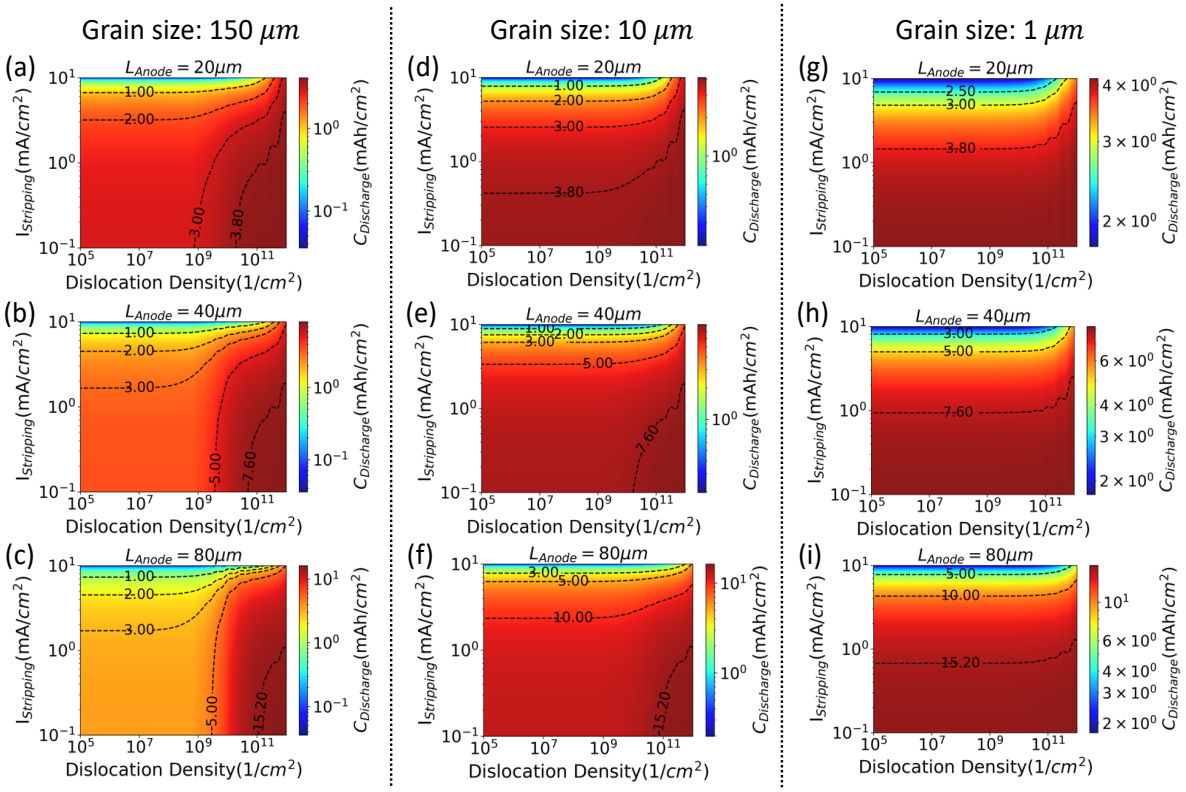

Figure 4.12 Maximum discharge capacity at given stripping current, dislocation density, and anode thickness. (a),(b),(c) show the capacity when grain size is 150μm, and (d),(e),(f) show the results when grain size is 10μm, and (g),(h),(i) exhibit the case when grain size is 1μm.

It can be explained that as the polycrystalline self-diffusivity is low while the stripping rate is high, the difference between two fluxes (i.e., Li atom flux and Li^+ ion flux) increases, and it leads to a short depletion time. Second, when dislocation density increases within the range of $10^5 \sim 10^9/cm^2$, the increase in discharge capacity is predicted to be marginal. This indicates that the volume fraction of total dislocations in Li anode at this level of number density is not large enough to boost the overall self-diffusion rate of Li metal. It is consistent with the plots in Figure 4.11, presenting the flat (or gently sloping) diffusivity surface in the density of 10^5~$10^9/cm^2$. Third, when Figure 4.12g-i are compared with Figure 4.12a-c, the longer portion of contour lines of discharge capacity are conspicuously flat when dislocation density is increased. It is because the polycrystal diffusivity is already high enough solely contributed by GB regions at the level of

1 μm grain size, and the kinetic effect of dislocation contribution is relatively small. But, even at such grain size level, ~10^{11}/cm^2 density of dislocations is predicted to push up the discharge capacity. Lastly, Figure 4.13 displays that the fraction of Li utilization per cycle can be raised when the thinner anode is used. This is reasonable because the thick anode larger than the diffusion length of the Li atom will have more excess Li than the thin anode.

To enable advanced battery applications, previous studies[20,98] suggested the goals of the electrochemical performance of Li metal batteries. ARPA-E IONICS project proposed the minimum current density of I = 3mA/cm^2 and the capacity C = 3mAh/cm^2, while the goals in the fast-charging project targeted at the minimum of I = 10mA/cm^2 and the capacity C = 5mAh/cm^2. By examining and screening all different combinations of design parameters with the above

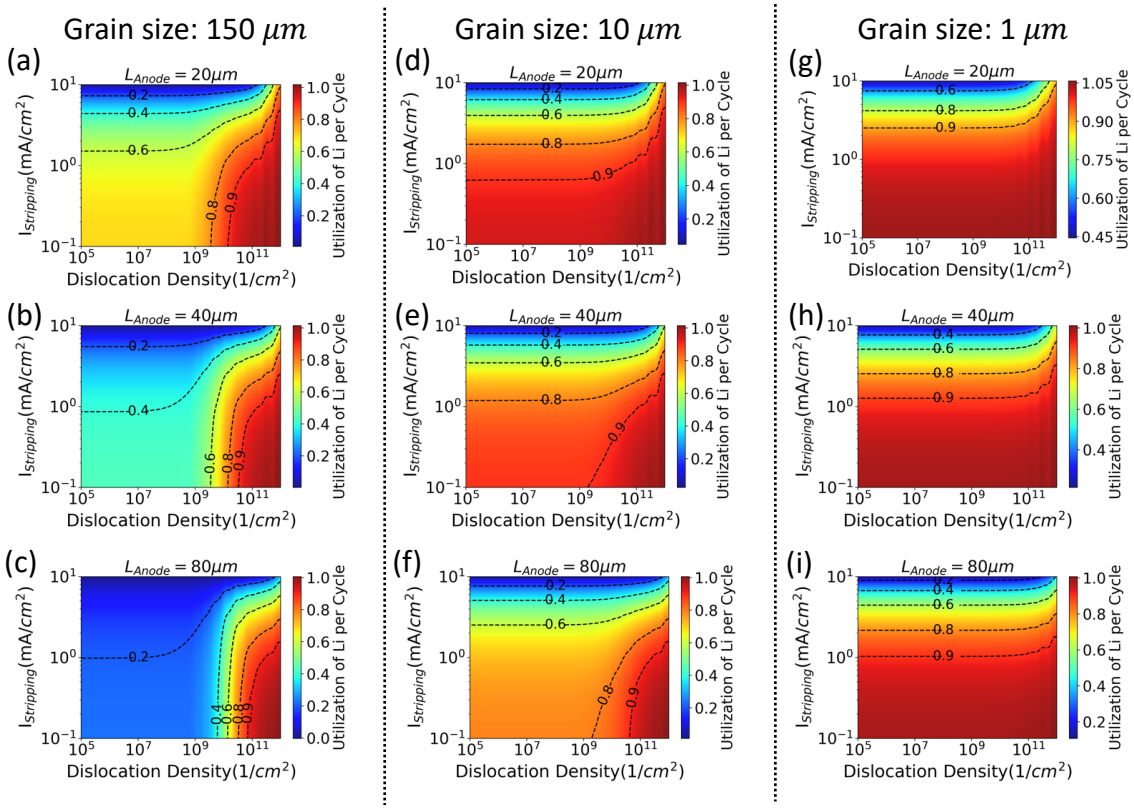

Figure 4.13 The fraction of Li utilization per cycle at given stripping current, dislocation density, and anode thickness. (a),(b),(c) show the capacity when grain size is 150μm, and (d),(e),(f) show the results when grain size is 10μm, and (g),(h),(i) exhibit the case when grain size is 1μm.

battery performance goals, microstructural design guidelines are proposed in Figure 4.14. In the plots, the fast-charging goal (I>10 C>5) is hatched with blue lines, and the ARPA-E Ionics goal (I>3 C>3) is pattern-filled with orange dots. The mixture of two goals (I>3 C>5) is green-hatched region. First, as depicted in Figure 4.14a, when the anode is 20 μm thick, only the ARPA-E Ionics goal is predicted to be reachable, as opposed to the cases of 30, 40, 80 μm thick anode. This is because the required minimum capacity C = 5 corresponds to ~25 μm anode thickness. In Figure 4.14b-d, it is shown that the increase in anode thickness will expand the combinations of grain size and dislocation density, satisfying the fast charging and mixture goals. This could be explained by the increase of depletion time to the maximum when the anode thickness is increased to the diffusion length of Li atom[23]. To fulfil the discharging goal with the minimum excess Li in the battery, it would be preferable to select the thinnest anode when the

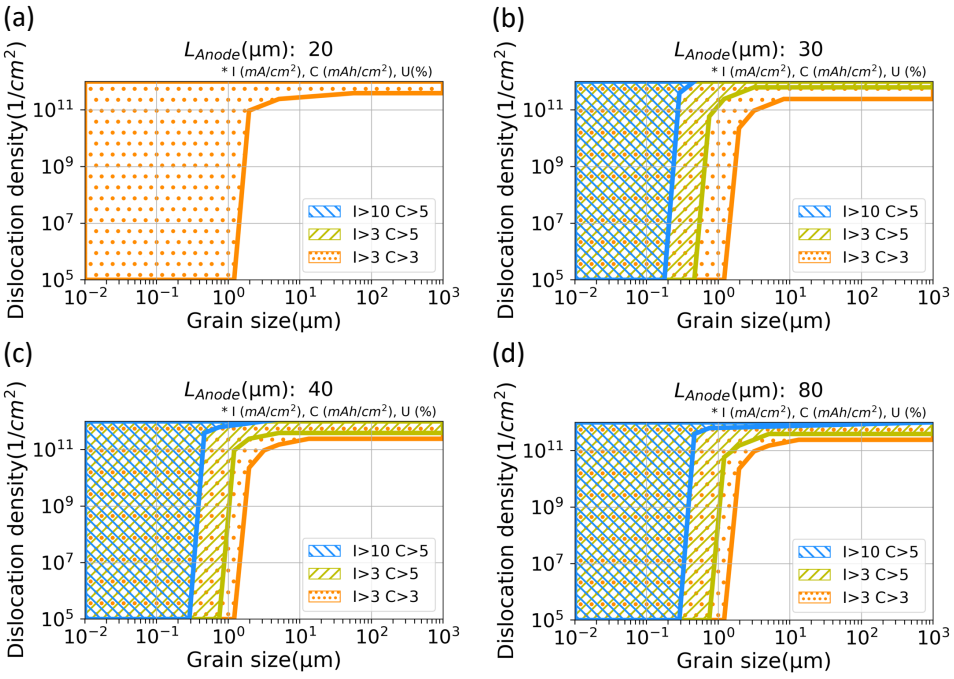

Figure 4.14 The microstructural design guideline plots of Li metal anode. The shaded region presents the combinations of grain size and dislocation density of an anode satisfying three different goals of battery performance, when anode thickness is (a) 20 μm, (b) 30 μm, (c) 40 μm, and (d) 80 μm. The fast-charging goal (I>10 C>5) is blue, the ARPA-E Ionics goal (I>3 C>3) is orange, and the mixture of two goals (I>3 C>5) is green area in the plot.

coordinates of grain size and dislocation density are in the shade of plots. Lastly, it is also noteworthy in Figure 4.14 that when the grain size is ~1 μm, even without a further kinetic contribution from dislocations, it is possible to meet I>3, C>3. Whereas when the average grain size is a few micrometers or larger, at least ~10^{11}/cm^2 dislocations are expected to be needed. Figure 4.15 is prepared to provide the updated design guidelines when the Li utilization per cycle is set to be larger than 80%. Those plots in Figure 4.15 clearly indicate that the fewer combinations of microstructural parameters will meet three goals in comparison with plots in Figure 4.14, when the excess Li in LMSSB is considered.

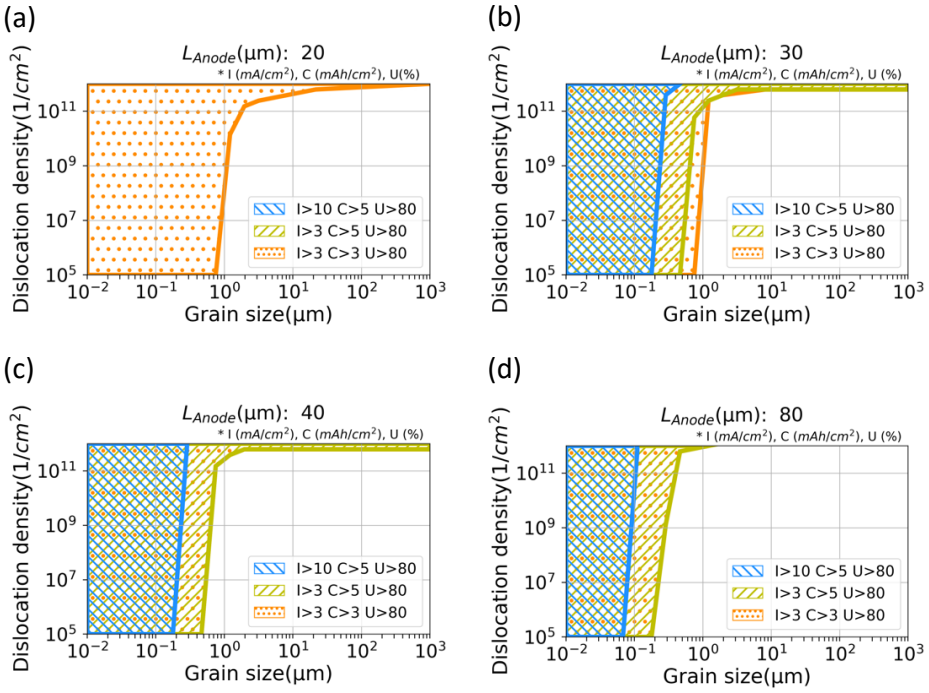

Figure 4.15 The microstructural design guideline plot of Li metal anode. The shaded region presents the combinations of grain size and dislocation density of an anode satisfying three different goals of battery performance, when anode thickness is (a) 20 μm, (b) 30 μm, (c) 40 μm, and (d) 80 μm. The fast-charging goal (I>10 C>5 U>80) is blue, the ARPA-E Ionics goal (I>3 C>3 U>80) is orange, and the mixture of two goals (I>3 C>5 U>80) is green area in the plot.

The design guidelines for microstructural features of Li (i.e., dislocation density and grain size) can be varied depending on the adopted models for polycrystalline diffusivities and input ranges of dislocation and GB diffusivities. The results proposed in Figures 4.14 and 4.15 are from mesoscale simulations based on the extended Hart model[51] (Eq 4.3). In this model, dislocations in each grain are assumed to be parallel with the 1D diffusion direction. However, if dislocations are assumed to form a 3D Frank net[123] within the Li anode, equation 2.31, Chen's model[58] would better describe the transport in Li polycrystal. Figure 4.16 demonstrates how the design guidelines for 30 μm-thick Li anode would change depending on the models. The result indicates that 10^{11}-10^{12}/cm^2 dislocation density will be required at the grain size larger than ~1μm according to the Hart model (the range ascribed to maximum and minimum diffusivities

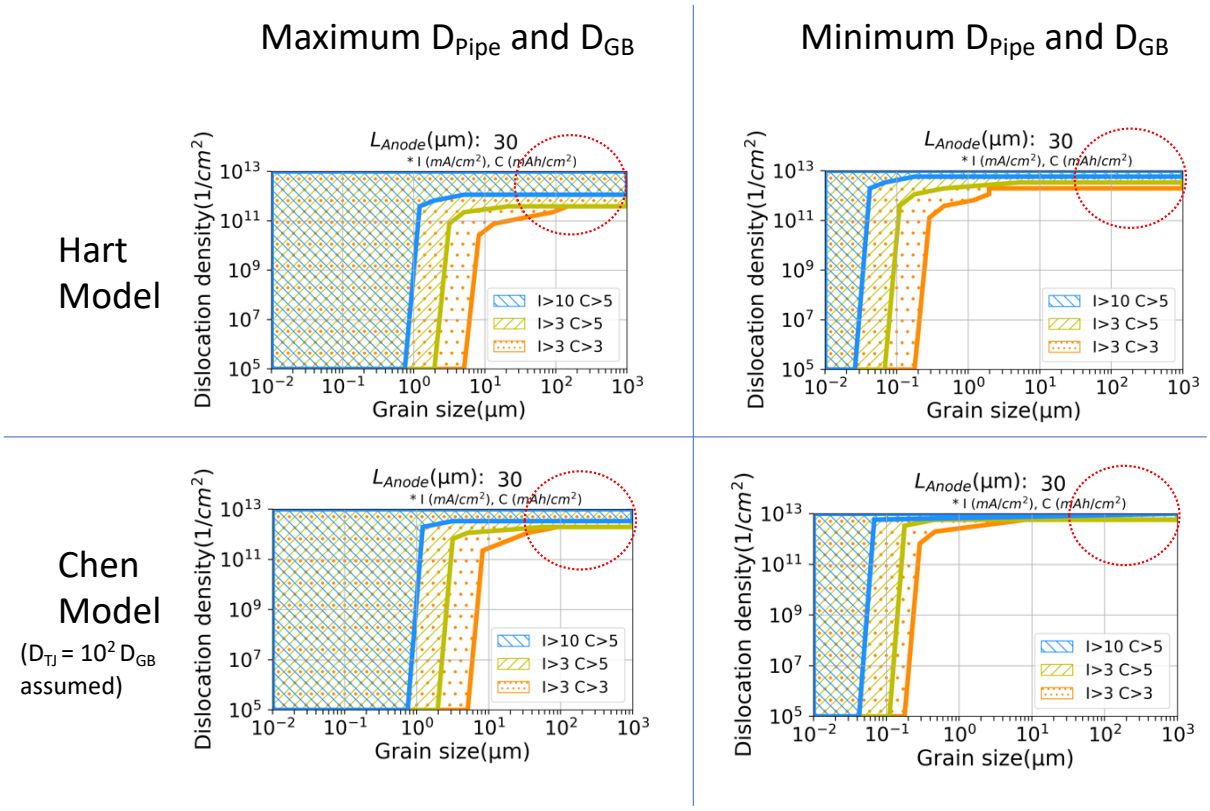

Figure 4.16 Variation in design guidelines depending on polycrystal models and uncertainties in GB and dislocation diffusivities. The extended Hart model (eq 2.28) and Chen's model (eq 2.31) are compared. For Chen's model, as the triple-junction diffusivity (D_{TJ}) is not available, the $D_{TJ} = 10^2 D_{GB}$ is assumed. The variation of plots for the maximum and minimum D_{Pipe} and D_{GB} are also exhibited.

in dislocation and GB); On the other hand, $10^{12}/cm^2$ dislocation density is predicted to be optimal by Chen's model including 3D dislocation orientations in the same grain size range. This is attributed to the lower diffusion rate in the intragranular region when the dislocations are laterally connected as well, as exhibited in Figure 2.2. Lastly, it needs to be pointed out that design guidelines of Chen's model in Figure 4.16 are based on the assumption that D_{TJ} is 100 times faster than D_{GB}; However, if D_{TJ} is faster than this level, $D_{polycrystal}$ at the small grain sizes can increase further, and thus, the required grain size to satisfy performance targets can become larger. Therefore, for more accurate predictions by Chen's model, D_{TJ} is required.

Experimentally, it has been reported that electro-deposited Li can have a few micro or sub-micrometer grain sizes on the current collector.[54,71,100,124] However, the battery community still lacks comprehensive studies on the dislocation density of Li metal due to the high chemical reactivity or sensitivity to high-energy beams required in TEM measurement[54,125]. Typically in metals, it is reported that dislocation density is in the range of 10^6~$10^8/cm^2$, and through heavy cold-working, it can increase to as high as $10^{12}/cm^2$.[126,127] In the work of Ungar et al[128], it is presented that when Ni was pulse-plated on cold-rolled Cu substrate, $4.9*10^{11}cm^2$ dislocation density and nanocrystalline grains were measured in the electrodeposits. It is speculated that such a high level of dislocation density is attributed to small grain size[124,129,130] and a large number of dislocation nucleation sites[54,124] in the electroplated layers. In the work of Singh, it was discussed that the large isostatic compression (e.g., 362 MPa in their study) during the cell fabrication of LMSSB can increase the dislocation density of the Li anode to ~$10^{12}/cm^2$.[101] However, given that high homologous temperature of Li at room temperature (*i.e.* T/T_m=0.66 at 298K) can result in dislocation annihilations in Li, there is a limitation in predicting the dislocation densities in Li

anode. Therefore, more experimental studies are needed to realize the microstructural engineering strategy toward the advanced LMSSB.

In the design guidelines, the required microstructural features (i.e., dislocation density and grain size) of Li anode are identified to satisfy battery performance targets. However, it needs to be acknowledged that there are limitations in the present model. First, the microstructural evolution of Li at the Li/SE interface (*e.g.* void formation) cannot be captured by the 1-D Fick's law model. Although the maximum discharge capacity is predicted by identifying the depletion time in the calculation, vacancies can be clustered before the depletion time, which can limit the capacity. To more accurately quantify accessible capacity, updating this model with kinetic Monte Carlo or phase field technique can be considered. Second, as no stack pressure is assumed, the model only accounts for the imbalance between Li^0 diffusional flux in the anode and Li^+ ion flux in the solid electrolyte. The current design guidelines do not consider Li creep deformation at the interface. Finally, diffusivities on Li surfaces and triple-junctions may also be important for modeling the stripping in LMSSB.

4.3.6 Creep Deformation Mechanism

During the stripping of LMSSB, when a cell is under stack pressure, both plastic deformation in the form of creep and diffusional flux of Li^0 atoms can play a role in controlling the morphology of Li at the Li/SE interface. In previous sections, we discussed enhancing the Li diffusional flux by exploiting fast diffusion along microstructural defects such as grain boundaries and dislocations. Here we focus on contributions to creep deformation arising from Li transport within these defects.

Creep is defined as time-dependent plastic deformation. Various creep mechanisms can operate within Li metal under pressure. In prior studies[92,101] of Li metal creep, diffusional creep (i.e., Nabarro-Herring and Coble creep) and dislocation-climb creep were investigated. However, those studies either 1) did not consider the contributions of dislocations to Li transport, or 2) did not characterize grain boundary sliding (GBS) creep. GBS can be the predominant creep mechanism in fine-grained materials.[131] Presumably, the scope of previous studies could have been limited by the lack of atomistic data (i.e., GB and dislocation diffusivity of Li). Using the atomistic data from the present simulations, the creep rate of each mechanism is evaluated, and the rate-controlling mechanism is identified as a function of temperature, applied (uniaxial) stress, and grain size.

In calculations of creep rates, constitutive equations from Ruano et al's studies[131,132] are used (Table 4.3). When the creep mechanism is controlled by bulk and pipe diffusions, the

Creep Mechanism	Equation	Reference
Diffusional creep		
Nabarro-Herring (Bulk and pipe diffusion)	$\dot{\varepsilon} = k_1(\frac{D_{Eff}}{d^2})(\frac{Eb^3}{kT})(\frac{\sigma}{E})$	k_1=14,[92,132]
Coble (GB diffusion)	$\dot{\varepsilon} = k_2(\frac{D_{gb}b}{d^3})(\frac{Eb^3}{kT})(\frac{\sigma}{E})$	k_2=50,[92,132]
Slip		
Dislocation climb (Bulk and pipe diffusion)	$\dot{\varepsilon} = k_3(\frac{D_{Eff}}{b^2})(\frac{\sigma}{E})^n$	k_3=10^{11}, n=5,[131,133]
Grain boundary sliding		
(Bulk and pipe diffusion)	$\dot{\varepsilon} = k_4(\frac{D_{Eff}}{d^2})(\frac{\sigma}{E})^2$	k_4= 2*10^9,[131]
(GB diffusion)	$\dot{\varepsilon} = k_5(\frac{D_{gb}b}{d^3})(\frac{\sigma}{E})^2$	k_5= 10^8,[131]

* $D_{Eff} = D_L f_L + D_P f_P = D_L + 50D_P(\frac{\sigma}{E})^2$,[131]

Table 4.3 Constitutive equations for creep deformation in polycrystalline Li. E is the elastic modulus, 7.82GPa,[101] b is the burgers vector, 3.04 Å,[101] d is the grain size, k is the Boltzmann constant 8.617*10^{-5} eV/K, T is the absolute temperature, σ is the uniaxial stress. The yield stress of Li metal is assumed to be 4.8mPa, as reported by Raj.[92]

effective diffusivity (i.e., D_{Eff}) is exploited, while the creep rate controlled by GB diffusion is computed with D_{gb}. The material's constants k_i or stress exponent n, were determined by referring to values provided in references.[92,101,131,132] It should be acknowledged here that the accuracy of the prediction of creep rates can be dependent on the error range of k_i and n.

Figure 4.17 shows the calculated Li creep deformation maps, identifying the dominant creep mechanism at a specified pressure, temperature, and grain size. In predicting these deformation maps, the atomistic data is an important input parameter. Depending on the mechanism, this diffusivity can arise from pipe and bulk diffusion or GB diffusion.

As a first example, we consider a case where the Li grain size is 150 μm with a pressure of ~ 1 MPa, Fig. 4.17d. In this scenario, dislocation climb is predicted to be dominant, consistent

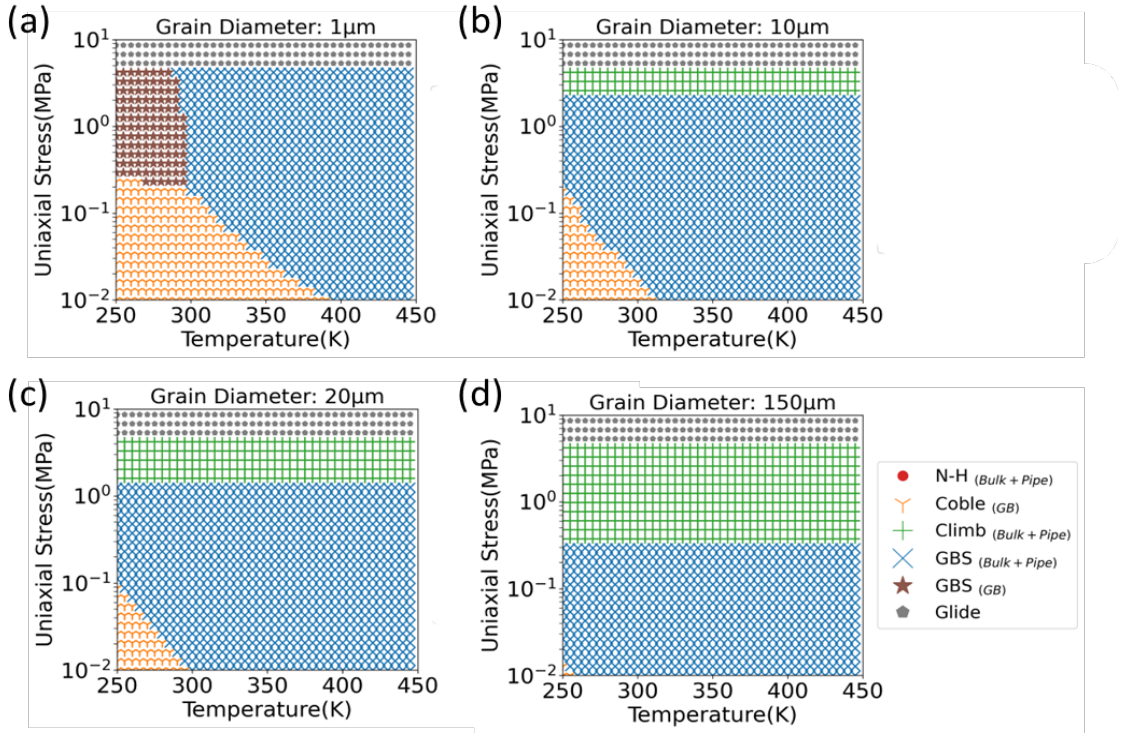

Figure 4.17 Creep deformation map of Li metal at grain size (a) 1 μm, (b) 10 μm, (c) 20 μm, and (d) 150 μm. As grain size decreases, grain boundary sliding and coble creep dominates the deformation.

with Masias et al's work.[109] However, for this same grain size and at stresses below 0.3MPa, GBS becomes the dominant mechanism. In the work of Raj et al,[92] in which the author considered the diffusional creep and dislocation climb only, Nabarro-Herring creep is predicted to be dominant. However, as GBS and pipe diffusions are additionally assessed in the present study, a different prediction is made. This suggests that including more atomistic transport properties and creep mechanisms is critical in the construction of the Li creep deformation map.

As a second example, we consider the case where the grain size is decreased to 1 μm, Fig. 4.17a. In this scenario, GBS and Coble creep dominate: Coble creep is expected at low stress, and GBS controlled by GB diffusion is expected at high stress. This can be explained by the larger stress exponent of $GBS_{(GB)}$ than $Coble_{(GB)}$. Furthermore, dislocation climb is not significant under any combination of the temperatures or pressures examined. This behavior is reasonable given that the deformation rate due to GBS and Coble creep increases when the grain size decreases, while dislocation climb creep is independent of the grain size. Lastly, at 300K and 1 μm grains, creep mechanisms are predicted to be controlled by GB diffusion than effective diffusivity.

The creep deformation map presented in our study can be a good reference to understand the mechanistic behavior of the Li anode when LMSSB is under stack pressure. There are improvements in our Li deformation maps compared to previous works[92,101], which deserves note. First, as compared to pre-existing maps which are based on assumptions on Li transport properties, such as diffusivities in dislocations or GBs, the creep maps in our study are constructed with constitutive equations informed by diffusivities from atomistic simulations. For example, diffusion rates in dislocations and GBs are assumed to be equal ($8.8*10^{-7}$ cm^2/s) in the study of Singh et al.,[101] while approximately 1 order difference in diffusivity is predicted

between edge dislocation and GB according to our simulations. Second, the work presented by Raj[92] did not consider the contributions of dislocations to Li transport, while our prediction included pipe diffusions using effective diffusivity. In particular, as dislocation densities are expected to be large in fine-grained or stack-pressured Li anode,[101] accommodating dislocation diffusivities will be important for more accurate predictions. Last, GBS creep is additionally considered in our study. In literature, when the grain size is small and stress level is in the intermediate range, GBS mechanism is reported to be predominant.[131] Our computation also evidences that when grain diameter is small (1 μm), the GBS mechanism dominates the creep deformation. Overall, the deformation map in our study exhibits that the creep behavior of Li anode can be evaluated more accurately when various creep mechanisms are considered and Li transport properties are understood at the atomistic level.

In closing, it is crucial to recognize the limitations of predicting the creep of Li under the stack pressure using solely constitutive equations. As reported in Haslam et al's work[134], when LMSSB is under compression loading, there are frictions at the interfaces of Li/SE and Li/Current collector. As a result, the resultant creep rate of Li is dependent on the thickness of Li, because the governing stress can change (i.e., hydrostatic vs deviatoric stress).[109,134] Furthermore, constitutive equations parameterized with tensile test data may not be directly applicable to the cell under compression.[134] Though the stress in Figure 4.17 represents the deviatoric component, guidelines can be further updated by quantifying the rate of each creep mechanism considering the compressive pressure, friction at the interfaces (Li/SE and Li/Current collector), and the estimation of hydrostatic and deviatoric stresses.

4.4 Conclusion

To prevent dendrite growth in Li metal-based solid-state batteries, suppressing void formation in the Li anode is critical. Voids reduce the contact area between the Li anode and solid electrolyte, resulting in the increase of local current density during plating and dendrite initiation.

The present study demonstrates that void formation at the interface of the Li anode and the solid electrolyte during stripping can be minimized by exploiting fast diffusion in microstructural defects (i.e., dislocations and grain boundaries) within the Li anode. By increasing the dislocation density and reducing the grain size, the volume fraction of defects will be raised, leading to the enhanced transport properties of the Li anode.

By using molecular dynamics simulations, we measured the self-diffusion rate in 2 low-energy edge and screw dislocations in Li metal. Compared to the bulk region, self-diffusivities of dislocations were found to be 2-5 orders of magnitude higher. Whereas the diffusion in dislocation was predicted to be comparable with or 1 order slower than in grain boundary. Li polycrystalline diffusivity is calculated as a function of both dislocation density and grain size. The results indicate that by tuning the concentration of microstructural defects in Li, boosting the self-diffusivity is possible by several orders of magnitude. By parameterizing the mesoscale model(based on Fick's 2nd law) with polycrystalline diffusivities, the dissolution process of LMSSB under zero stack pressure was simulated. The model linked stripping current, dislocation density, grain size, anode thickness, and the maximum discharge capacity. The model predicts that the high dislocation density of ~10^{11}-10^{12}/cm^2 would enable achieving performance targets of advanced Li metal batteries even with a grain size larger than ~1 μm.

Lastly, all atomistic kinetic parameters (i.e., Li diffusivities in dislocation, GB, and bulk) are exploited to create the plastic deformation map for LMSSB under the stack pressure. The creep rate of each mechanism is evaluated using constitutive equations, and the dominant creep mechanism at the given stress, temperature, and grain size is identified. The map presents that when the grain size is 150 μm, the dislocation-climb creep rate is largest, while when the grain is 1 μm, coble creep and GBS will be predominant. In the fine-grained Li polycrystalline, the creep deformation is confirmed to be controlled by GB diffusion.

Chapter 5 Predicting Wettability at the Li Anode and Cu Current Collector Interface

5.1 Introduction

Despite the advantages of better safety and high energy density, there is a challenge regarding cycling inefficiencies in realizing "anode-free" Li metal solid-state batteries (LMSSB). One hypothesis explains that this is relevant with nucleation overpotential and inhomogeneous deposition of Li on metal current collectors (e.g., Cu foil).[26,135] During plating, a large nucleation barrier of Li on a metal current collector (CC) will require the additional energetic cost to charge a cell. Also, the inhomogeneous deposition attributed to the poor wettability between Li and a metal CC can cause the contact loss between Li and CC during cycling, resulting in the degradation of the Coulombic efficiency.[28] In the study of Dudney et al.,[29] it was shown that the non-uniform nucleation and isolated Li islands on Cu CC could result in low reversibility of a cycling and damage to the Cu substrate in a "anode-free" cell.

To lower the nucleation overpotential and enhance the wettability of Li on a metal CC, studies have focused on introducing an alloy interlayer between a current collector and a solid electrolyte.[6,30,31,134] The work of Lee et al[30] demonstrated that by interposing the Ag-C layer between the SUS CC and LPSCl, more uniform Li deposition and long cyclability can be achieved. In the work of Haslam et al.,[134] the layer of Au metal clusters between Cu CC and LLZO is confirmed to eliminate the nucleation overpotential during Li plating and induce the homogeneous nucleation on Cu CC. In addition, Wang et al[6] demonstrated that by including a Li_2Te layer between Cu CC and LPSCl, lowering the nucleation barrier and homogenizing Li electrodeposition is possible.

While studies above have shown that lowering the nucleation overpotential during Li plating can improve cell performance, there is still a lack of knowledge of the origin of the barrier of Li deposition on a metal CC. Oftentimes it is hypothesized that the low solubility, large interfacial energy, and poor work of adhesion between Li and a metal substrate can form the large nucleation overpotential.[72] For example, in the work of Yan et al.,[72] the overpotential observed during Li plating on Cu CC was explained by no formation of the solid solution layer between Li and Cu, which would eliminate the nucleation barrier if it existed. Meanwhile, Qin et al[33] have reported that the poor wetting behavior of Li and Cu CC could be originated from the presence of a native oxide layer on Cu rather than the lithiophobicity of Cu metal; Because a typical Cu foil has an oxide layer, Li can react with it and form Li_2O leading to poor wettability. Given that commercially viable Cu foil can have such an oxide surface, the investigation regarding the Li wettability change depending on the presence of Cu oxide is worthwhile.

To understand the chemical reaction during Li plating onto the Cu oxide layer, previous studies for the Cu_xO conversion electrode can be referred to.[136,137] For example, CuO is a well-known conversion material that involves a two-step reduction process as follows.

1. $2CuO + 2Li^+ + 2e^- \rightarrow Cu_2O + Li_2O$
2. $Cu_2O + 2Li^+ + 2e^- \leftrightarrow 2Cu + Li_2O$

As the 1st reduction process is irreversible, only 2nd step will take place while cycling persists, in which the electrodes will be comprised of Cu_2O, Cu, Li_2O, and Li. Experimental observations[136,137] of the nano-sized metallic particles in the Li_2O matrix are also consistent with the reaction equation at the 2nd step. Martin et al[138] have performed density functional theory(DFT) calculations for the work of adhesion of interfaces which can be present within the lithiated Cu oxide; The authors concluded that interface formation of Cu_2O/Cu and Li_2O/Cu are thermodynamically favorable, whereas that of Li_2O/Cu_2O could be unfavorable. In the study of

Lowe et al,[139] the thermodynamic properties of various models of Li/Li_2O interface are computed using DFT. In the calculations, both poor and good wettability are predicted depending on the Li_2O terminations of interfaces. Though the above studies explored many interfaces comprising Cu, Cu_2O, Li, or Li_2O, we still need the contact properties of Li and Cu (or Cu_2O) to complete the understanding of the lithiophobic behavior of the Cu CC.

Here we investigated the thermodynamic properties of Li/Cu and Li/Cu_2O interfaces. Highly probable interface models are down-selected, and the wettability of each interface is investigated. Our results indicate that both pure metallic Cu and Cu_2O are lithiophilic. However, when Cu_2O is lithiated, the subsequent conversion reaction can generate Li/Li_2O; Among various interface models, a stoichiometric Li/Li_2O interface is predicted to have low work of adhesion, accounting for the poor wettability of Li and Cu current collector. Our study suggests that removing the native oxide layer of the Cu current collector in "anode-free" LMSSB can potentially resolve the inhomogeneous plating and dendrite formation issue.

5.2 Methods

5.2.1 First-Principles Calculations

DFT calculations were performed using Vienna ab initio Simulation Package (VASP). Exchange-correlation effects were described using Perdew, Burke, and Ernzerhof (PBE) functional. Interactions between core and valence electrons were treated with the projector-augmented wave method. The energy cutoff of 390 eV and 520 eV were used for a plane-wave basis set during energy calculations of Li/Cu and Li/Cu_2O interface, respectively. The convergence criterion for the electronic ground state was set to 10^{-5} eV, and that for the ionic

relaxation was set to 0.05eV/Å. Kpoint grid for each interface model is determined based on the convergence test, as shown in Table 5.1.

5.2.2 Surface Energies

Surface energies of Li, Cu, and Cu_2O were investigated before the down-selection of facets (or terminations) to construct the thermodynamically most probable interface models. For Li and Cu metals, (100), (110), and (111) low-index surfaces were explored. In the case of Cu_2O, the (111) surface was studied because it had been reported as the lowest-energy facet in prior studies[138,140–142]. As exhibited in Figure 5.1, Cu_2O(111) surface has a tri-layer lateral unit, where a Cu layer is sandwiched by two oxygen layers. In this study, three terminations of (111) surface were considered: stoichiometric O#1 termination shown in Figure 5.1(b), non-stoichiometric O#2 termination shown in Figure 5.1(c), and non-stoichiometric Cu#1#2 in Figure 5.1(d). The surface energies of 3 terminations of Cu_2O were calculated using equation 5.1,

$$\sigma = \frac{1}{A}(E_{slab} - \sum_i n_i^{slab}\mu_i^{Cu_2O}) \tag{5.1}$$

Interface	# of atoms	Cell size in a (Å)	Cell size in b (Å)	Li strain in a (%)	Li strain in b (%)	Kpoints (a, b, c)
Li(100)/Cu(111)	588	13.6	23.6	-0.7	-1.7	(4, 2, 1)
Li(110)/Cu(111)	448	23.6	10.3	-1.7	0.3	(2, 4, 1)
Li(100)/Cu(100)	175	10.3	10.3	0.1	0.1	(4, 4, 1)
Li(100)/Cu_2O(111)(O#1)	387	24.3	10.5	1.1	2.2	(2, 4, 1)
Li(110)/Cu_2O(111)O#1	420	42	6.1	0.1	2.2	(1, 6, 1)
Li(100)/Cu_2O(111)O#2	410	36.9	12.1	-0.1	1.3	(2, 4, 1)
Li(110)/Cu_2O(111)O#2	436	42	6.1	0.1	2.2	(1, 6, 1)

Table 5.1 Details of the interface models investigated in this study

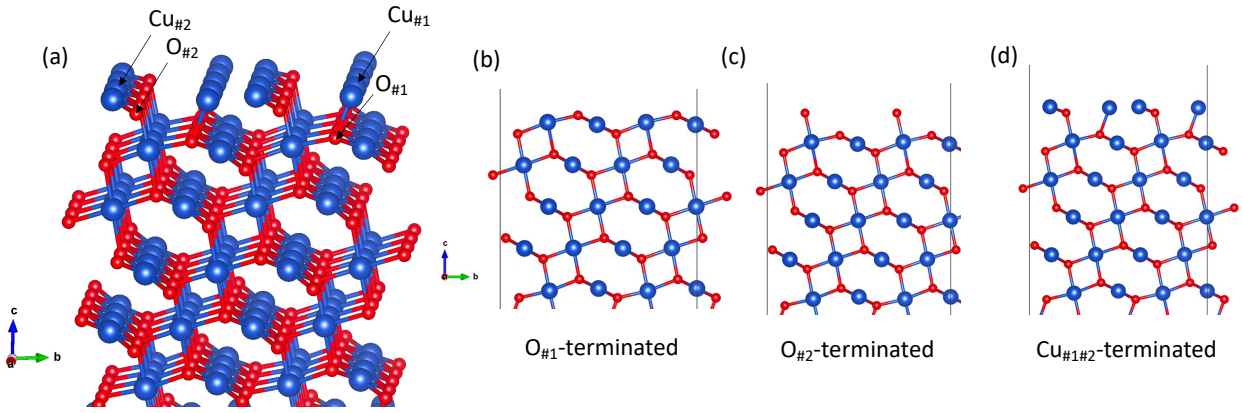

Figure 5.1 Surface structures of $Cu_2O(111)$. (a) tilted-view snapshot of $Cu_2O(111)$ surface, (b) stoichiometric O#1 termination, (c) non-stoichiometric O#2 termination, and (d) non-stoichiometric Cu#1Cu#2 termination are displayed.

where E_{slab} is the total electronic energy of the slab, n_i^{slab} is the number of atoms of the element i in the slab, $\mu_i^{Cu_2O}$ is the chemical potential of the element i in the bulk Cu_2O, and A is the surface area.

In equation 5.1, there are two variables, i.e., $\boldsymbol{\mu_{Cu}^{Cu_2O}}$ and $\boldsymbol{\mu_{O}^{Cu_2O}}$. However, two chemical potentials are related by the total energy of Cu_2O bulk $\boldsymbol{E_{Cu_2O}^{Bulk}}$, as shown in equation 5.2.

$$E_{Cu_2O}^{Bulk} = 2\mu_{Cu}^{Cu_2O} + \mu_{O}^{Cu_2O} \tag{5.2}$$

Thus, we can evaluate the surface energy σ of 3 different terminations in Figure 5.1b-d as a function of $\mu_O^{Cu_2O}$. The allowable range of $\mu_O^{Cu_2O}$ can be determined by the following constraints to prevent the decomposition of Cu_2O into the elements.

$$\mu_{O}^{Cu_2O} \leq \frac{1}{2} E_{O_2}^{gas}$$

$$\mu_{Cu}^{Cu_2O} \leq \mu_{Cu}^{FCC\ Bulk} \tag{5.3}$$

5.2.3 Interfacial Thermodynamics

Figure 5.2 summarizes the computational procedures to measure the work of adhesion of Li/Cu and Li/Cu_2O interfaces. First, with the lowest energy facets of Li, Cu, and Cu_2O, interface models were generated. In the modeling, the relative rotation of two slabs and the supercell expansion of two unit-cell slabs were considered to minimize the strain of Li (less than 2%) for the lattice match. The interface supercell has two, symmetry-equivalent interfaces, as Cu(or Cu_2O) slab is sandwiched by Li slab in symmetry. Subsequently, with the initially generated interface models, the rigid-body translation of one slab relative to the other was performed in all three directions; γ surface analysis was performed to identify the in-plane (a,b directions) translation state corresponding to the minimum energy configuration; The distance between two slabs in c direction was varied between 1 Å and 4 Å, and the work of adhesion (W_{ad}) of two slabs at each distance was measured. By fitting W_{ad} vs inter-distance to the universal binding energy relation (UBER), the unrelaxed W_{ad} was calculated as exhibited in Figure 5.3 and Figure C.1. The structure obtained from the rigid-body translation was input to the ionic relaxation step. As the interfacial effects are expected to be localized to atomic layers adjacent to the interface,[138] atoms in the bulk region were fixed during the relaxation. Lastly, the single-point energy calculation was followed on the relaxed structure with the more strict convergence criterion, and the relaxed W_{ad} was measured.

Thermodynamic properties of interfaces comprised of a strained Li and a slab B (either Cu, or Cu_2O) were evaluated, including interface formation energy $E_{formation}$, interface energy $E_{interface}$, and strain energy E_{strain}. For the stoichiometric interface, the formation energy (per mole) was calculated with the equation 5.4,

$$E_{formation} = \frac{E_{Li/B} - n_{Li}^{Li\,Slab}\mu_{Li}^{Li(BCC)} - n_{B}^{Slab\,B}\mu_{B}^{Bulk}}{N/N_A} \quad (5.4)$$

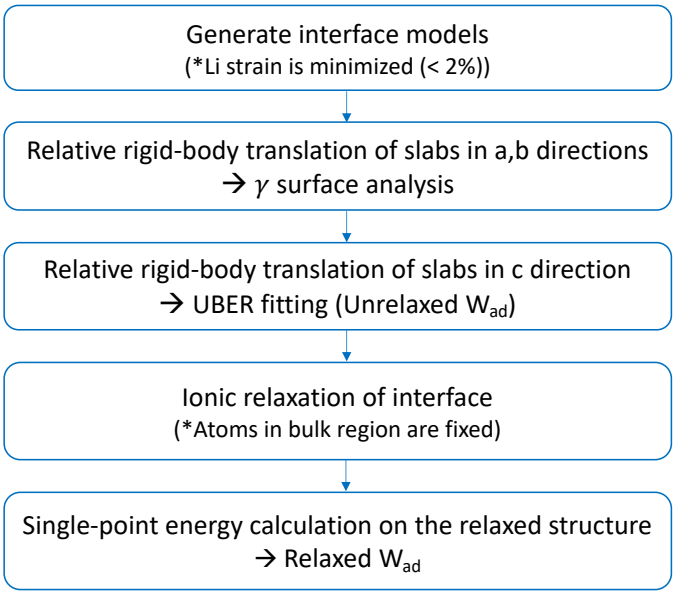

Figure 5.2 Computational procedures to measure the interfacial work of adhesion

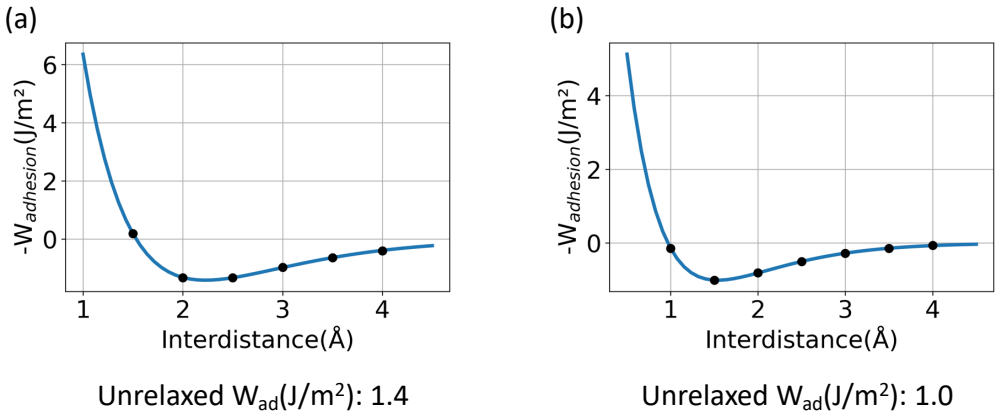

Figure 5.3 Universal Binding Energy Relation(UBER) plot of (a) Li(100)-Cu(111), (b) Li(100)-Cu_2O(111)O#1 interfaces.

where $E_{Li/B}$ is the energy of relaxed Li/B interface, $n_{Li}^{Li\ Slab}$ is the number of Li atoms in the Li slab, $\mu_{Li}^{Li(BCC)}$ is the chemical potential of Li in bulk Li metal, $n_B^{Slab\ B}$ is the number of B atoms(or

compounds) in the slab B, μ_B^{Bulk} is the chemical potential of B atom in bulk(or one formula unit), N is the number of total atoms in the interface model, and N_A is the Avogadro number.

The interface energy for the stoichiometric system was calculated using the equation 5.5,

$$E_{interface} = \frac{E_{Li/B} - n_{Li}^{Li\ Slab}\mu_{Li}^{Li(c)} - n_B^{Slab\ B}\mu_B^{Bulk}}{2A} \quad (5.5)$$

where $\mu_{Li}^{Li(c)}$ is the chemical potential of bulk Li strained in a and b directions to match the lattice vector of slab B in the interface model (and relaxed in c direction), and 2A is the area of symmetric interfaces.

The equation to calculate the strain energy (per mol) is expressed in equation 5.6.

$$E_{strain} = E_{formation} - \frac{2A\ N_A}{N} E_{interface} \quad (5.6)$$

In the present study, Li was strained in all interfaces as its mechanical properties are stiffer than Cu and CuO according to previous studies.[143,144]

When the interface includes non-stoichiometric Cu_2O, the Cu_2O slab in the interface is either oxygen-deficient or oxygen-excessive. As such, the interface formation energies can be varied as a function of $\boldsymbol{\mu_O^{Cu_2O}}$. The $\boldsymbol{E_{formation}}$ were computed for two extreme equilibrium cases expressed in the equation 5.3,

Equilibrium condition 1: $\boldsymbol{\mu_O^{Cu_2O} = \frac{1}{2}E_{O_2}^{gas}}$

$$\boldsymbol{E_{formation} = \frac{N_A}{N}\{E_{Li/Cu_2O} - n_{Li}^{Li\ Slab}\mu_{Li}^{Li(BCC)} - \frac{1}{2}n_{Cu}^{Cu_2O\ Slab}E_{Cu_2O}^{Bulk} - (n_O^{Cu_2O\ Slab} - \frac{1}{2}n_{Cu}^{Cu_2O\ Slab})\frac{1}{2}E_{O_2}^{gas}\}} \quad (5.7)$$

Equilibrium condition 2: $\boldsymbol{\mu_{Cu}^{Cu_2O} = \mu_{Cu}^{FCC\ Bulk}}$

$$\boldsymbol{E_{formation} = \frac{N_A}{N}\left\{E_{Li/Cu_2O} - n_{Li}^{Li\ Slab}\mu_{Li}^{Li(BCC)} - \frac{1}{2}n_{Cu}^{Cu_2O\ Slab}E_{Cu_2O}^{Bulk} - \left(n_O^{Cu_2O\ Slab} - \frac{1}{2}n_{Cu}^{Cu_2O\ Slab}\right)\left(E_{Cu_2O}^{Bulk} - 2\mu_{Cu}^{FCC\ Bulk}\right)\right\}} \quad (5.8)$$

For calculations of interfacial and strain energies of non-stoichiometric Li/Cu_2O, equations 5.5 and 5.6 were referred to and identical approaches were adopted. During the analysis of $\boldsymbol{\mu_{Li}^{Li(c)}}$, the energy contribution of a stacking fault was removed by comparing it with the bulk energy of Li.

5.2.4 Interface Wettability

The work of adhesion W_{ad} of interfaces comprised of Li slab and slab B(either Cu or Cu_2O) were calculated with the equation 5.9,

$$W_{ad} = \frac{1}{A}(E_{Li} + E_B - E_{Li/B}) \quad (5.9)$$

where A is the interfacial area, E_{Li}, E_B, $E_{Li/B}$ are energies of an isolated Li slab, an isolated B slab, Li/B interface respectively. The number of layers or the dimension of isolated slabs was equal to those within the interface models. First, to obtain the unrelaxed W_{ad}, the work of adhesions of the "rigid" interface was calculated as a function of the interfacial separation using equation 5.9. (In this case, isolated slabs and a Li/B interface were unrelaxed.) Afterward, the energy versus distance was fit to the UBER (equation 5.10),[145]

$$W_{ad} = -W_{ad}^0\left(1 + \frac{d-d_o}{l}\right)e^{-\frac{(d-d_o)}{l}} \quad (5.10)$$

where W_{ad}^{0} is the unrelaxed work of adhesion, d_o is the interfacial separation, and l is a scaling length. Second, the relaxed W_{ad} was computed with the equation 5.9, where E_{Li}, E_B, $E_{Li/B}$ are energies of relaxed structures.

The contact angle θ_c was measured using Young-Dupre equation,

$$\theta_c = \cos^{-1}\left(\frac{W_{ad}}{\sigma_{Li}} - 1\right) \tag{5.11}$$

where W_{ad}, σ_{Li} are the relaxed work of adhesion and Li surface energy, respectively.

5.3 Results and Discussion

5.3.1 Li and Cu Surface Energies

As shown in Table 5.2, the surface energies of low-index facets of Li and Cu are investigated to down-select the most probable Li/Cu interface models. In case of Li, (100) and (110) surfaces are predicted to have first and second lowest energy respectively. When Cu surface energies are measured, (111) and (100) facets are confirmed to have first and second lowest energies each. The order of surface energies calculated in this study is consistent with references. Based on the result, Li(100)/Cu(111), Li(100)/Cu(100), Li(110)/Cu(111) are selected as interface models, as they are predicted to be thermodynamically most probable.

Facets	Li Surface Energy(J/m^2)	Ref [1]- Li Surface Energy(J/m^2)
100	0.47	0.49
110	0.49	0.53
111	0.55	0.56
Facets	Cu Surface Energy(J/m^2)	Ref [2]- Cu Surface Energy(J/m^2)
100	1.47	1.47
110	1.53	1.56
111	1.33	1.34

Table 5.2 Surface energies of low-index facets of Li and Cu.

5.3.2 Cu_2O Surface Energies

To determine Li/Cu_2O interface models, the surface energies of various terminations of Cu_2O were investigated. In Figure 5.4, (111) surface energies are evaluated as a function of oxygen chemical potential. The range of oxygen chemical potential is determined from two equilibrium conditions mentioned in the Methods section (i.e., $\mu_O^{Max} = \frac{1}{2}E_{O_2}^{gas}$, $\mu_O^{Min} = E_{Cu_2O}^{Bulk} - 2\mu_{Cu}^{FCC\ Bulk}$). When $E_{O_2}^{gas}$ is calculated, the binding energy of O_2 is corrected with the equation 5.12, because $E_{Binding}$ of O_2 is overestimated in DFT.[146,147]

$$E_{O2}(0K) = 2E_O(0K) + E_{Binding} \quad (5.12)$$

In Equation 5.12, $E_O(0K)$ is the DFT energy of the isolated O element, $E_{Binding}$ is the empirical binding energy 5.12eV/molecule [148].

As exhibited in Figure 5.4, O#1 and O#2 terminated surfaces are predicted to be most stable in the (111) facet. This result is consistent with Soon et al's work[147] where non-defected (111) oxygen terminations are reported to have lower energies than the non-defected (111) copper termination. However, an inconsistency is also found between our result and the prior

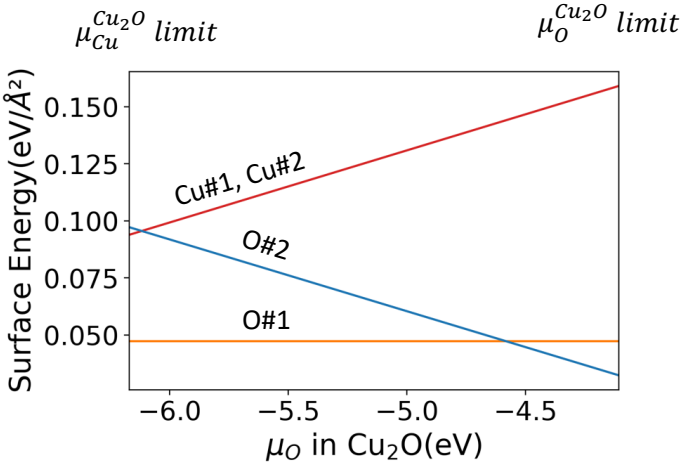

Figure 5.4 Surface energies of Cu_2O(111) as a function of oxygen chemical potential.

work[147]; the order of surface energies of O#1 and O#2 terminations are flipped at the $\mu_O^{Cu_2O\ limit}$ in Figure 5.4, whereas Soon et al predicted the order would be constant. Presumably, it could be explained that the energy correction for the $E_{Binding}$ of DFT is performed in our study as opposed to the reference. Based on the surface energy evaluation of Li and $Cu_2O(111)$, the most probable interface models are selected for further analysis: Li(100)/Cu_2O(111)O#1, Li(110)/Cu_2O(111)O#1, Li(100)/Cu_2O(111)O#2, Li(110)/Cu_2O(111)O#2.

5.3.3 Relaxed Interfacial Structures

Figure 5.5 displays examples of relaxed Li/Cu and Li/Cu_2O interfaces. As displayed in Figure 5.5a, when the Li/Cu is relaxed, the interfacial effect is predicted to be moderate and mostly localized to the first atomic layers of Li and Cu adjacent to the contact. However, when Li is interfaced with Cu_2O, a more significant distortion of the contact morphology is predicted as depicted in Figure 5.5b. It could be attributed to the conversion reaction occurring when the copper oxide is lithiated. According to the reaction energy calculation, the thermodynamic driving force for the reduction of Cu_2O to Cu is large.

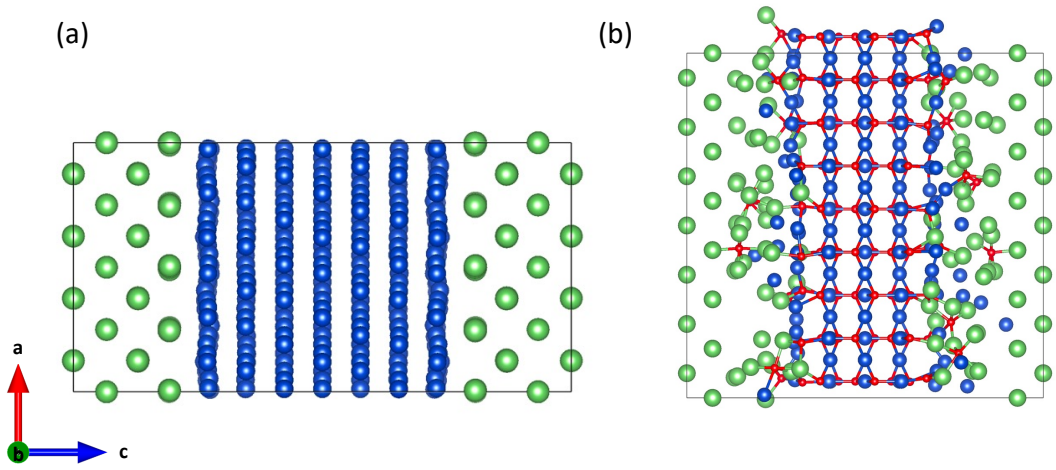

Figure 5.5 Structures of the relaxed a) Li(100)/Cu(111), b) Li(100)/Cu_2O(111)O#1 interfaces. Li, Cu, and O atoms are colored green, blue, and red respectively.

$$2\ Li + 1\ Cu_2O \rightarrow 2\ Cu + Li_2O,\ E_{Reaction} = -0.85\ eV/atom \quad (5.13)$$

The isolated Cu atoms and O-coordinated Li atoms in Figure 5.5b exhibit the products of the conversion reaction.

5.3.4 Li/Cu Interfacial Properties

Three models of Li/Cu interface were examined: Li(100)/Cu(111), Li(110)/Cu(111), and Li(100)/Cu(100). First, using equations 5.4-5.6, interfacial formation energy, interface energy, and strain energy were calculated (Table 5.3). The calculated formation energies (0.4-3 kJ/mol) and interface energies (0.1-0.4 J/m^2) are positive and small, indicating that low energetic cost is required to form Li/Cu interface and chemical bonding. The smaller interfacial energy of Li(110)/Cu(111) than that of the other two models suggests that bonding at the corresponding interface will be formed more easily. Strain energies are predicted to be from 1 to 5% of the total formation energy; Given the range of strain energy of Li/Li_2CO_3 in the work of Liu et al was 1.3-11.7% of the formation energy,[149] the strain in the interfaces of the current study is evaluated to be small.

The wettability of Li and Cu is assessed by calculating the unrelaxed/relaxed work of adhesions, and contact angle. In all interfaces, strong adhesions between Li and Cu are predicted resulting in perfect wettings. This result is consistent with Qin et al's study[33], reporting that pure

Interface	$E_{formation}$ (kJ/mol)	$E_{interface}$ (J/m^2)	E_{strain} (kJ/mol)	Unrelaxed W_{ad} (J/m^2)	Relaxed W_{ad} (J/m^2)	θ_c (deg)
Li(100)/Cu(111)	2	0.3	0.02	1.4	1.4	0
Li(110)/Cu(111)	0.4	0.1	0.02	1.5	1.8	0
Li(100)/Cu(100)	3	0.4	0.04	1.2	1.5	0

Table 5.3 Thermodynamic properties of Li/Cu interface

Cu is lithiophilic. To further understand the origin of the large nucleation energy barrier of Li on Cu current collector, the properties of Li/Cu_2O interfaces are explored.

5.3.5 Li/Cu_2O Interfacial Properties

Four models of Li/Cu_2O interface were examined: Li(100)/Cu_2O(111)O#1, Li(110)/Cu_2O(111)O#1, Li(100)/Cu_2O(111)O#2, Li(110)/Cu_2O(111)O#2. For non-stoichiometric interfaces (i.e., Li(100)/Cu_2O(111)O#2, Li(110)/Cu_2O(111)O#2), both interfacial formation energies and interface energies are calculated for oxygen-excessive/oxygen-deficient conditions(corresponding to equilibrium condition 1/ condition 2 respectively). As shown in Table 5.4, interfacial formation energies are predicted to be in the range of -25 to -8 kJ/mol, showing that interface will be formed spontaneously. In addition, more negative interface energies are predicted for non-stoichiometric interfaces suggesting stronger interfacial bonding. Strain energies of interface models are measured to be 0.06-0.4% of total interfacial formation energies. The relaxed work of adhesions of Li/Cu_2O is 2.5-4.3 J/m^2, larger than those of Li/Cu. The contact angle estimations of Li/Cu_2O interfaces predict 0 degree. In conclusion, Cu_2O is confirmed to be lithiophilic.

Interface	$E_{formation}$ (kJ/mol)	$E_{interface}$ (J/m^2)	E_{strain} (kJ/mol)	Unrelaxed W_{ad} (J/m^2)	Relaxed W_{ad} (J/m^2)	θ_c (deg)
Li(100)/Cu_2O(111)O#1	-10	-1.3	0.03	1.0	2.5	0/0
Li(110)/Cu_2O(111)O#1	-8	-1.1	0.01	1.3	2.3	0/0
Li(100)/Cu_2O(111)O#2	-25/-17	-3.3/-2.3	0.07	2.3	4.3	0/0
Li(110)/Cu_2O(111)O#2	-21/-14	-3.0/-2.0	0.01	2.5	4.0	0/0

Table 5.4 Interfacial properties of Li/Cu_2O. For interfaces including Cu_2O(111)O#2, $E_{formation}$ and $E_{interface}$ are calculated for each equilibrium condition, (i.e., equilibrium condition 1/ condition 2). As Li/Cu_2O is predicted to undergo conversion reaction when interfacial atoms are relaxed, θ_c for unrelaxed W_{ad}/relaxed W_{ad} are measured respectively.

5.3.6 Lithiophobicity of Cu Substrate

Given that the native oxide layer is present on the Cu current collector, at the beginning of Li plating, the uniformity of Li nucleation will be determined by the work of adhesion of the Li/Cu_2O interface. However, as Li plating progresses, new phases will be formed in Cu_2O resulting in various interfaces contributing to Li wetting; The strong downhill energy of the conversion reaction ($E_{Reaction}$ = -0.85 eV/atom, Equation 5.13) reduces Cu_2O to Cu and forms Li_2O, and thus, the adhesion of Li/Cu and Li/Li_2O interfaces will determine the wetting.

Table 5.5 shows the interfacial formation energy, relaxed work of adhesion, and the contact angle of Li/Cu (from the current study) and Li/Li_2O (from the Lowe et al's work[139]). Among all thermodynamically most probable interfaces, the Li(111)/$Li_2O(111)_{(stoichiometric)}$ is solely predicted to have small work of adhesion and a large contact angle. This can account for the lithiophobic behavior of Cu current collector in experiments[33,72,150]. It must be acknowledged that the interfacial formation energy of Li(111)/$Li_2O(111)_{(O\text{-}term)}$ is more negative than that of Li(111)/$Li_2O(111)_{(stoichiometric)}$, and thus, the former is more likely to be present than the latter under the equilibrium.

Interface	$E_{formation}$ (kJ/mol)	Relaxed W_{ad} (J/m^2)	θ_c (deg)
Li(100)/Cu(111)	2	1.4	0
Li(110)/Cu(111)	0.4	1.8	0
Li(100)/Cu(100)	3	1.5	0
Li(111)/Li_2O(111)(Stoichiometric)	3.76	0.18	132
Li(111)/Li_2O(111)(O-term)	-34.7/-5.81	6.69	0

Table 5.5 Thermodynamic properties of most probable interfaces during Li plating on the Cu current collector. Interfacial properties of Li/Li_2O are from the Lowe et al's study[139]. For Li(111)/Li_2O(111)(O-term), interfacial formation energies are reported for oxygen-excessive/oxygen-deficient equilibrium conditions.

However, given that the Li plating could occur at the non-equilibrium condition, $Li(111)/Li_2O(111)_{(stoichiometric)}$ could be present at the interface of Li and Cu current collector.

In the DFT study of Martin et al[138], interface formation of Li_2O/Cu_2O was reported to be thermodynamically unfavorable, while that of Li_2O/Cu and Cu_2O/Cu were favorable; Based on these findings, the authors proposed the model of lithiated Cu_2O electrode comprised of a Li_2O matrix including small metallic Cu particles and the large domain of Cu_2O. By integrating the results of Martin et al[138], Lowe et al[139], and the current study, the updated model is proposed as shown in Figure 5.6. The schematics in Figure 5.6 display the interfacial region of the Li/Cu current collector during plating. When Li is deposited on the fresh Cu_2O layer upon the start of plating, Li will wet the Cu_2O layer perfectly due to the good work of adhesion (Figure 5.6a). However, as the plating progresses, Cu_2O will turn into a Li_2O matrix where Cu particles and the Cu_2O domain are embedded (Figure 5.6b). As Li will be deposited on the Li_2O surface at this intermediate state, non-uniform deposition and poor wetting are anticipated.

The model in the current study predicts that removing the native oxide layer of the Cu

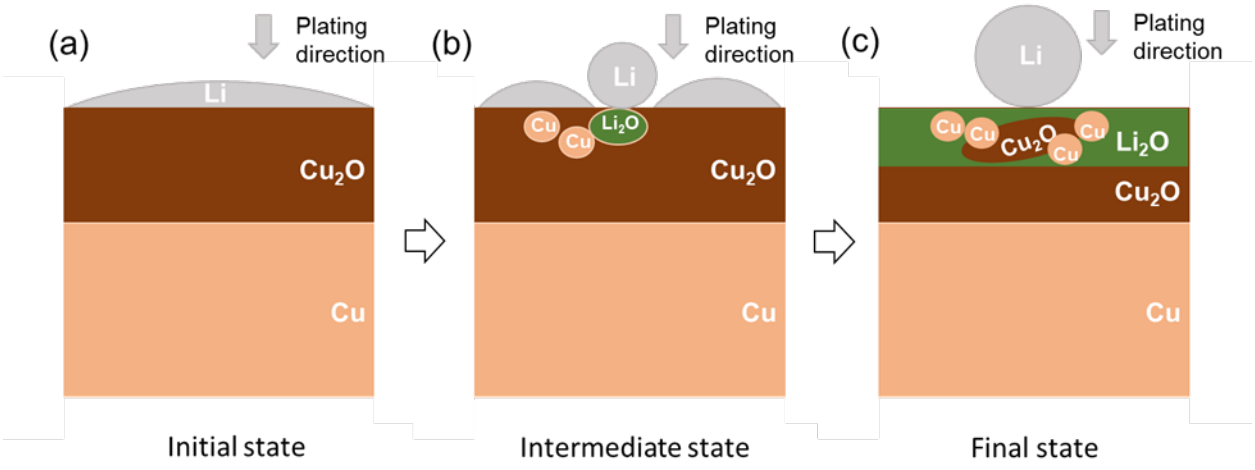

Figure 5.6 Schematic of the interfacial region of Li/Cu current collector (a) upon the start of plating, (b) at the intermediate state of plating, (c) at the final state of plating. Initially good wetting is anticipated due to the large work of adhesion of Li/Cu_2O. However, as Li_2O phase is formed, poor wetting and non-uniform deposition will occur.

current collector can prevent such inhomogeneous plating issues; As pure Cu is predicted to be lithiophilic, Cu_2O-etched Cu current collector will show lithiophilic behavior.

5.4 Conclusion

To achieve robust solid-state batteries employing Li metal anodes, a key challenge is to prevent the inhomogeneous and inefficient plating of Li on the Cu current collector. In prior studies aimed at understanding Li plating on a Cu substrate, various explanations were provided (i.e., the lithiophobicity of Cu surface VS the native oxide layer on Cu), and not all of these are consistent. Therefore, the present DFT work aims to carefully characterize the thermodynamics and the adhesion/wettability of the interface between Li and the Cu current collector.

Several models of Li/Cu and Li/Cu_2O interfaces were developed. These models were down-selected based on the energies of various facets and chemical terminations of the surfaces of each material, to determine the thermodynamically most probable interfaces. For each interface model, the interfacial formation energy, interface energy, strain energy, work of adhesion, and contact angle are computed. The results indicate that Cu and Cu_2O are lithiophilic; in contrast to some prior assertions of non-wetting behavior at this interface.[72] However, as the Li plating progresses, the Cu_2O layer on Cu current collector is expected to form Li_2O through the conversion reaction; And the Li/Li_2O stoichiometric interface is confirmed to have the poor work of adhesion. Given that the Li plating on Cu_2O is expected to occur at non-equilibrium conditions, the formation of Li/Li_2O stoichiometric interface and the resulting non-wetting behavior of Li on the Cu current collector are plausible. In conclusion, the current study suggests that the origin of non-uniform plating in LMSSB can be traced to the native oxide layer on the

Cu current collector. Therefore, minimizing the thickness of this oxide layer during the manufacturing of LMSSB should improve performance.

Chapter 6 Conclusions and Next Steps

6.1 Conclusions

All-solid-state batteries based on Li metal anodes (LMSSB) are a promising "beyond-Li ion" technology with the potential to achieve high energy densities and enhanced safety. However, the formation of harmful Li dendrites during the operation of these batteries has slowed their commercialization. To aid in overcoming this challenge, the research presented in this thesis clarifies several kinetic and thermodynamic properties of Li metal in the context of LMSSB using multiscale simulation methods.

First, the diffusion coefficients of 55 tilt and twist grain boundaries (GBs) in Li are predicted using molecular dynamics simulation. GB diffusion was found to be 3 to 6 orders of magnitude faster than in the bulk. Atomic-scale data were used to parameterize a meso-scale model of Li depletion in the anode during discharge. The model suggests design and operation guidelines for LMSSB that link the Li grain size, discharge current, anode thickness, and achievable capacity. The model predicts that Li anodes with average grain sizes ranging from 0.1 to 3 μm have sufficient Li diffusivity to meet performance targets for rate capability and capacity. These grain sizes are approximately two orders of magnitude smaller than those in (coarse-grained) commercial Li foils. The model highlights the importance of microstructures of the Li anode on the performance of LMSSB.

Second, the self-diffusivity of Li in two dislocations types (edge and screw) was calculated using molecular dynamics. The diffusion in the dislocation core was predicted

to be 2-5 orders of magnitude faster than in BCC bulk Li. Although faster than diffusion in the bulk, depending on the temperature, dislocation (pipe) diffusivity is comparable to, or 1 order slower than GB diffusivity. Based on the pipe diffusion data, an updated mesoscale model of Li depletion in the anode during stripping was parameterized to include Li transport along GBs and dislocation cores. The model predicts that a relatively high dislocation density, ~10^{11}-10^{12}/cm^2, is needed to satisfy performance targets of advanced Li batteries even at a grain size larger than ~1 μm. It is conceivable that dislocation densities of this magnitude could be present in highly deformed Li. Lastly, the accumulated atomistic data were used to parameterize constitutive equations to predict plastic deformation maps of Li as a function of temperature, stress, and grain size. These maps predict that when the grain size is large (~150 μm), dislocation-climb dominates the creep deformation. However, in fine-grained Li metal (~1 μm-size grain), GB sliding and Coble creep predominate, as GB transport controls the creep deformation under these conditions.

Lastly, the adhesive and thermodynamic properties of the interface of Li metal and a Cu current collector are predicted using density functional theory. Surface energies of various facets (or terminations) of Li, Cu, and Cu_2O were evaluated to down-select the thermodynamically most probable Li/Cu and Li/Cu_2O interface models. For each model, the interfacial formation energy, interface energy, strain energy, and the work of adhesion are calculated. The results indicate that both Cu and Cu_2O are lithiophilic. However, because of the conversion reaction in lithiated Cu_2O, the formation of Li_2O is expected when Li is in contact with Cu_2O. This nascent Li_2O can potentially form a stoichiometric lithiophobic interface with Li; Given that plating in LMSSB can occur under non-equilibrium conditions, such a poorly-adherent Li/Li_2O interface can be present and could explain the inhomogeneities observed for Li plating on Cu (oxide)

substrates. This study highlights the importance of the native oxide layer on Cu in realizing homogeneous plating of Li on the Cu current collector.

6.2 Next Steps

In Chapters 3 and 4, a multiscale model for Li transport in a Li metal anode is developed. Nevertheless, there are several avenues to extend the model.

First, the self-diffusivity of polycrystalline Li depends on the grain size and the dislocation density. The distribution and orientation of these features can be difficult to measure and are therefore generally not perfectly known. To account for this uncertainty, the results from our models refer to a range of predicted values by including extreme cases as well as average behavior. For example, as discussed in chapters 3 and 4, plating the Li anode operates under non-equilibrium conditions. Under these conditions various higher-energy or non-equilibrium GB structures can be present. In this case, it is not correct to simply base diffusivity predictions on the lowest-energy GBs. Rather, our results account for the fastest, slowest, and average GB diffusivities in determining the optimal grain sizes. Similar uncertainties apply to the orientation of GBs and dislocations in Li polycrystals. For example, our simulations show that diffusing within a GB plane is typically much faster than perpendicular to the plane. These orientations impact the overall diffusivity, and several models of orientation and number density of these features were examined to place realistic bounds on the predicted transport properties. Detailed experimental measurements of the grain size distribution, orientation, and dislocation density/connectivity would be helpful in adding more realism to our predictions.

Second, though the depletion time was predicted with a 1-D model in our study, the voiding and contact loss are 3-D phenomena. To more accurately identify vacancy clustering and

its impact on the accessible capacity of LMSSB, more complex mesoscopic models present fruitful avenues to extend this work. For example, kinetic Monte Carlo or phase field techniques can be used to realistically capture the 2D or 3D microstructural evolution of the Li anode. These models would benefit by adopting the atomistic transport properties obtained in the present study.

Third, though the deviatoric stress is used to construct the Li creep deformation map, it is still unclear how the stack pressure and deviatoric stress are related during the operation of LMSSB. When the cell is under compressive loading, friction at two interfaces (i.e., Li/metal current collector, Li/solid electrolyte) also affect the stress state of Li metal. As a result, the deviatoric stress within the Li anode can change as a function of the Li thickness. Our creep deformation map can be further updated with the aim of replacing the uniaxial stress with the compressive stack pressure in future studies.

Fourth, the yield stress used in the current Li creep deformation maps is assumed to be constant. However, the threshold stress (or the yield stress) for plastic flow via dislocation glide can be a function of grain size. This is the well-known Hall-Petch relationship, which states that dislocation motion is impeded by GBs. Hence, when the grain size is reduced a larger stress level is required to initiate plastic deformation. In a related result, Conrad et al also reported that in BCC Niobium, polycrystals with smaller grain size have higher dislocation densities.[129] Together, these data imply that fine-grained BCC Li is more likely to have increased work hardening rate. Overall, the current Li plastic deformation maps need to be updated to reflect the yield stress change as a function of grain size. More experimental studies are required for that.

In Chapter 5, it is revealed that the lithiophobic behavior of a Cu current collector is attributed to the formation of Li_2O through Li reactions involving the native oxide layer of Cu. There are several opportunities to extend this work.

First, it is not clear if or how the initial deposition behavior of Li on Cu foil can influence the dendrite formation after large quantities of Li have been deposited (e.g., 20 μm-thick Li). It would be interesting to investigate the effect of the uniformity of an initial nucleation layer on 1) the plating current distribution, 2) the morphology evolution of subsequent Li layers, 3) the possibility of dendrite formation.

Second, our DFT study concluded that the poorly-adherent Li/Li_2O interface can be a source of the overpotential observed for Li nucleation on a Cu substrate. However, this prediction is based on thermodynamics only. In reality, Cu_2O reduction and Li_2O formation conversion reaction could be kinetically slow. If the latter is true, then our analysis would not fully explain the origin of the plating overpotential; other phenomena may be at play and experimental measurements can help clarify the situation. Sessile drop tests of molten Li on Cu foil, and characterization of their resulting interfaces, are being performed by our experimental collaborators.

Third, although the removal of the oxide layer on a Cu foil is expected to enhance Li wetting at the beginning of deposition, it is likely impractical to cycle LMSSB under an oxygen-free environment. When oxygen is present, Li_2O will be generated and be present at the interface of the Li/Cu current collector. Improvements to cell manufacturing and oxygen-free operation would be needed to minimize Li_2O formation and thereby realize homogeneous plating of Li on the Cu current collector.

Appendices

Appendix A - Supporting Tables and Figures for Chapter 3

Table A.1 Details for the symmetric tilt grain boundaries investigated in this study

Rotation Axis	GB plane	Misorientation Angle (°)	Simulation cell length			No. atoms in simulation cell
			Lx (Å)	Ly (Å)	Lz (Å)	
[001]	∑25(710)	16.26	98.63	98.63	13.95	12800
	∑13(510)	22.6	71.13	71.13	13.95	6528
	∑17(410)	28.07	57.51	71.89	13.95	5440
	∑5(310)	36.87	44.11	66.16	13.95	3776
	∑29(520)	43.6	75.12	75.12	13.95	7392
	∑29(730)	46.4	106.23	106.23	13.95	14720
	∑5(210)	53.13	31.19	77.98	13.95	3168
	∑17(530)	61.93	81.33	81.33	13.95	8640
	∑13(320)	67.38	50.29	75.44	13.95	4960
	∑25(430)	73.74	69.74	69.74	13.95	6396
[01-1]	∑33(811)	20.05	80.13	84.99	14.79	9360
	∑19(611)	26.53	60.8	64.49	14.79	5352
	∑27(511)	31.59	51.25	72.48	14.79	5136
	∑9(411)	38.94	41.85	73.97	14.79	4224
	∑11(311)	50.48	32.71	69.39	14.79	3120
	∑33(522)	58.99	56.66	60.1	14.79	4680
	∑3(211)	70.53	24.16	59.79	14.79	1968
	∑17(322)	86.63	40.67	71.89	14.79	3984
	∑17(433)	93.37	57.51	61	14.79	4776
	∑3(111)	109.47	34.17	60.4	14.79	2878
	∑33(455)	121.01	80.13	84.99	14.79	9495
	∑11(233)	129.52	46.26	65.43	14.79	4176
	∑9(122)	141.06	29.59	62.77	14.79	2600
	∑27(255)	148.41	72.48	76.88	14.79	7772
	∑19(133)	153.47	42.99	60.8	14.79	3648
	∑33(144)	159.95	56.66	60.1	14.79	4727
[11-1]	∑31(156)	17.9	95.12	82.37	18.12	13320
	∑21(145)	21.79	78.29	67.8	18.12	9000
	∑13(134)	27.8	61.6	71.13	18.12	7344

∑7(123)	38.21	67.8	65.24	18.12	7452
∑19(235)	46.83	74.47	64.49	18.12	8064

Table A.2 Structural parameters for twist grain boundaries investigated in this study.

Rotation Axis	GB plane	Misorientation Angle (°)	Simulation cell length			No. of atoms in simulation cell
			Lx (Å)	Ly (Å)	Lz (Å)	
[001]	∑25(001)	16.26	49.32	62.77	49.32	14112
	∑13(001)	22.62	35.56	62.77	35.56	7344
	∑17(001)	28.07	43.13	62.77	43.13	10782
	∑5(001)	36.87	33.08	62.77	33.08	6336
	∑29(001)	43.6	37.56	62.77	37.56	8176
	∑29(001)	46.4	53.12	62.77	53.12	16352
	∑5(001)	53.13	23.39	62.77	23.39	3168
	∑17(001)	61.93	40.67	62.77	40.67	9584
	∑13(001)	67.38	37.72	62.77	37.72	8262
	∑25(001)	73.74	52.31	62.77	52.31	15876
[01-1]	∑33(01-1)	20.05	80.13	64.11	56.66	27456
	∑19(01-1)	26.53	60.8	64.11	42.99	15808
	∑27(01-1)	31.59	51.25	64.11	36.24	11232
	∑9(01-1)	38.94	41.85	64.11	29.59	7488
	∑11(01-1)	50.48	32.71	64.11	23.13	4560
	∑33(01-1)	58.99	56.66	64.11	40.06	13728
	∑3(01-1)	70.53	24.16	64.11	17.08	2496
	∑17(01-1)	86.63	40.67	64.11	28.76	7072
	∑17(01-1)	93.37	57.51	64.11	40.67	14144
	∑3(01-1)	109.47	25.63	64.11	18.12	2808
	∑33(01-1)	121.01	80.13	64.11	56.66	27456
	∑11(01-1)	129.52	46.26	64.11	32.71	9120
	∑9(01-1)	141.06	44.38	64.11	31.38	8424
	∑27(01-1)	148.41	72.48	64.11	51.25	22464
	∑19(01-1)	153.47	42.99	64.11	30.4	7904
	∑33(01-1)	159.95	56.66	64.11	40.06	13728
[11-1]	∑31(11-1)	17.9	95.12	60.4	54.92	29160
	∑21(11-1)	21.79	78.29	60.4	45.2	19821
	∑13(11-1)	27.8	61.6	60.4	35.56	12293
	∑7(11-1)	38.21	67.8	60.4	39.14	14936
	∑19(11-1)	46.83	74.47	60.4	42.99	18032

Table A.3 Calculated γ surfaces for symmetric tilt grain boundaries.

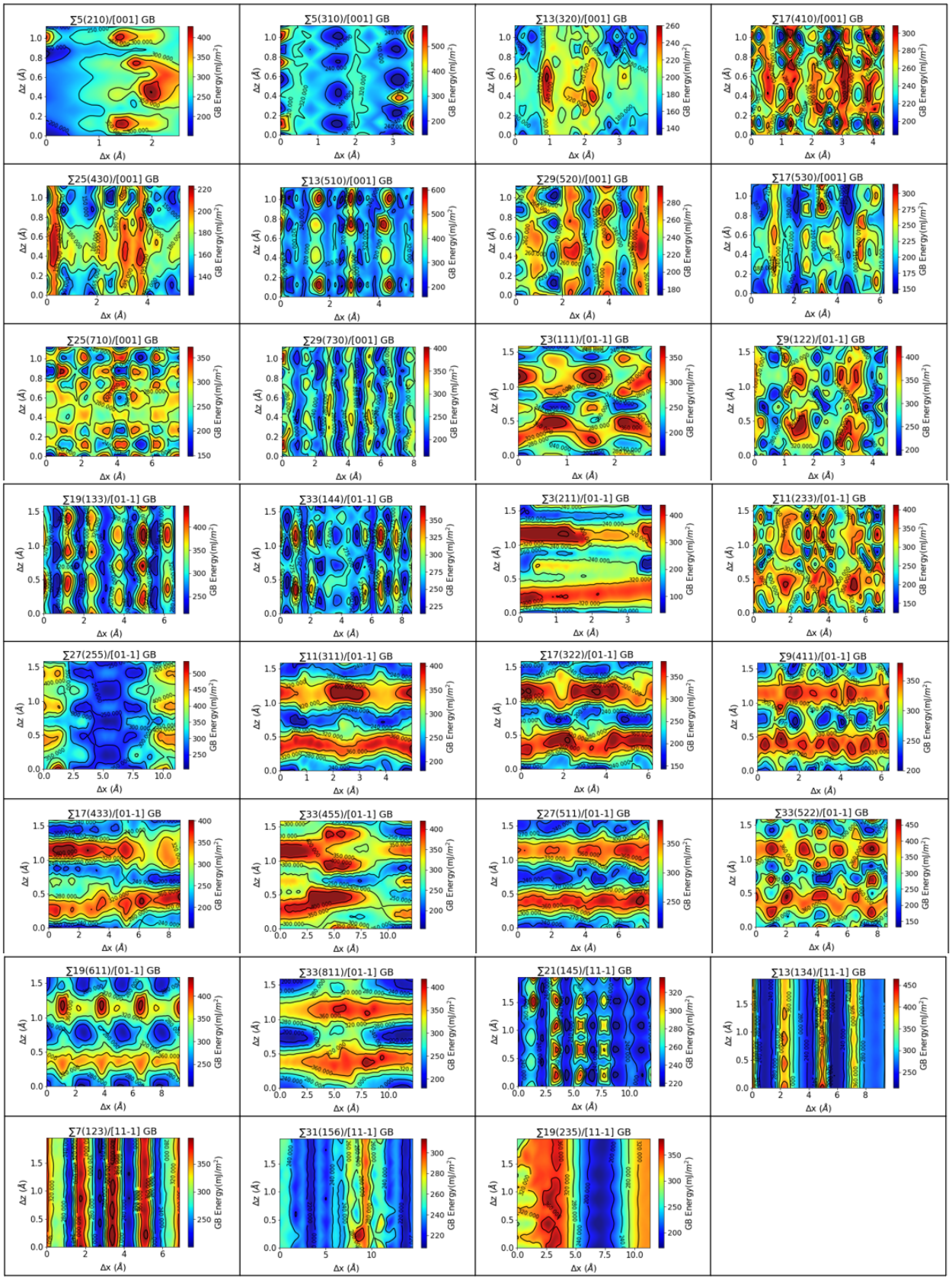

Table A.4 Calculated γ surfaces for twist grain boundaries.

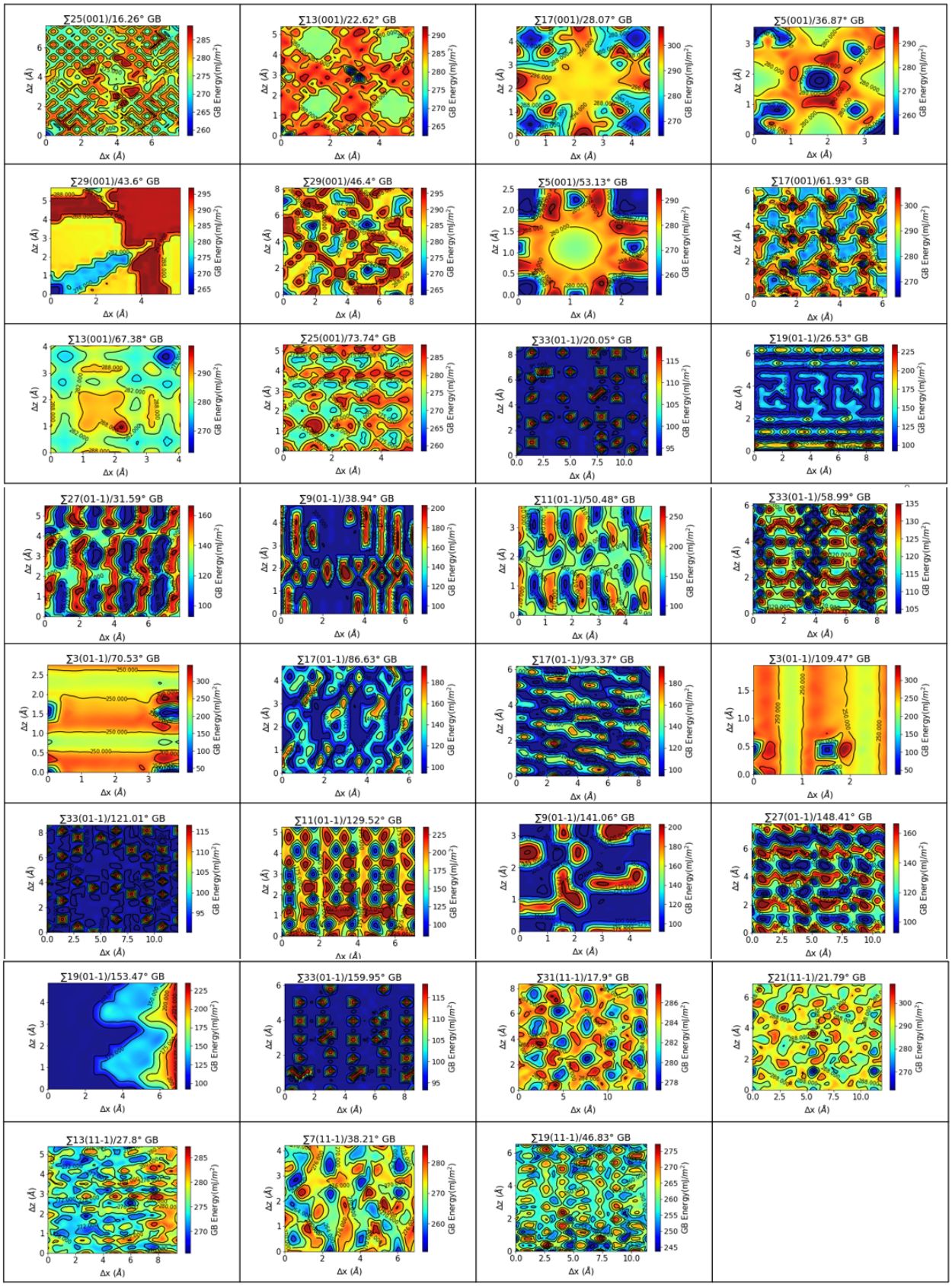

Table A.5 Calculated GB widths (Å) of (a)-(c) tilt GBs, (d)-(f) twist GBs, and (g) the average across all GBs as a function of temperature. The value at each temperature is sampled every 0.1 ns and time-averaged.

a) [001] tilt\Temperature(K)	250	300	350	400
∑5(210)	7.2	7.8	9.5	16.2
∑5(310)	8.2	8.5	11.4	18.1
∑13(320)	8.9	9.6	10.9	13.5
∑17(410)	8.1	9.3	11.6	16.3
∑25(430)	10.2	9.5	10.2	12.7
∑13(510)	8.9	9.3	11	15
∑29(520)	8.8	9.1	12.6	18.9
∑17(530)	8.9	9.4	10.5	18.4
∑25(710)	10.8	11.2	12.6	14.3
∑29(730)	8.3	9	13.6	19.8
b) [01-1] tilt\Temperature(K)	250	300	350	400
∑9(122)	12.7	14.3	12.5	15.6
∑19(133)	13	13.2	13.6	17
∑33(144)	13.7	14.1	13.5	16.3
∑27(255)	11.8	12.7	14.2	18
∑11(311)	14.8	12.7	13.3	15.9
∑17(322)	13.2	13.3	13.1	13.7
∑9(411)	6.6	7	13	17
∑17(433)	16	14.1	14.5	16.2
∑33(455)	17.1	14.9	14.3	14.9
∑27(511)	8.7	11.5	14.2	17
∑33(522)	13	13	12.9	13.4
∑19(611)	11.6	12.5	14.4	17.6
∑33(811)	12.1	12.3	13.2	16.2
c) [11-1] tilt\Temperature(K)	250	300	350	400
∑7(123)	12.7	12.7	13.4	16.6
∑13(134)	12.3	13.1	12.6	16.6
∑21(145)	11.8	12.6	12.8	17.7
∑31(156)	10.7	10.9	12.9	17.1
∑19(235)	13.4	14.4	13.4	14.4
d) [001] twist\Temperature(K)	250	300	350	400
∑5(001)/53.13°	14.7	15.3	15.4	17.0
∑5(001)/36.87°	15.2	15.5	15.5	18.9
∑13(001)/67.38°	15.5	15.3	15.2	18.0
∑17(001)/28.07°	14.2	14.3	14.9	19.8
∑25(001)/73.74°	16.6	15.9	16.1	16.9
∑13(001)/22.62°	15.4	15.4	15.2	17.4
∑29(001)/43.6°	14.5	14.8	15.6	20.2
∑17(001)/61.93°	13.7	14.0	14.6	19.2

∑25(001)/16.26°	16.2	15.5	15.6	17.2
∑29(001)/46.4°	14.6	14.8	15.3	21.8

e) [01-1] twist\Temperature(K)	250	300	350	400
∑19(01-1)/153.47°	6.6	6.8	7.2	9.1
∑33(01-1)/159.95°	6.5	6.7	7.2	9.4
∑11(01-1)/129.52°	8.8	8.7	8.3	11.2
∑27(01-1)/148.41°	6.8	7.4	8.0	9.7
∑11(01-1)/50.48°	7.6	7.9	7.9	9.3
∑17(01-1)/86.63°	5.9	6.3	6.6	8.7
∑17(01-1)/93.37°	6.2	6.8	7.2	7.9
∑33(01-1)/121.01°	9.3	10.0	9.8	12.2
∑27(01-1)/31.59°	7.3	7.6	7.7	9.4
∑33(01-1)/58.99°	7.8	8.1	8.3	9.8
∑19(01-1)/26.53°	6.5	6.9	7.7	8.8
∑33(01-1)/20.05°	6.7	6.9	7.3	9.0
f) [11-1] twist\Temperature(K)	250	300	350	400
∑7(11-1)/38.21°	10.7	10.9	11.2	14.4
∑13(11-1)/27.8°	9.9	10.3	11.4	19.7
∑21(11-1)/21.79°	9.8	10.6	12.6	17.9
∑31(11-1)/17.9°	10.8	11.4	12.5	20.4
∑19(11-1)/46.83°	10.1	11.3	11.9	14.7

g) Average GB width\Temperature(K)	250	300	350	400
	10.9	11.2	12	15.3

Table A.6 Calculated mean squared displacements for symmetric tilt GBs.

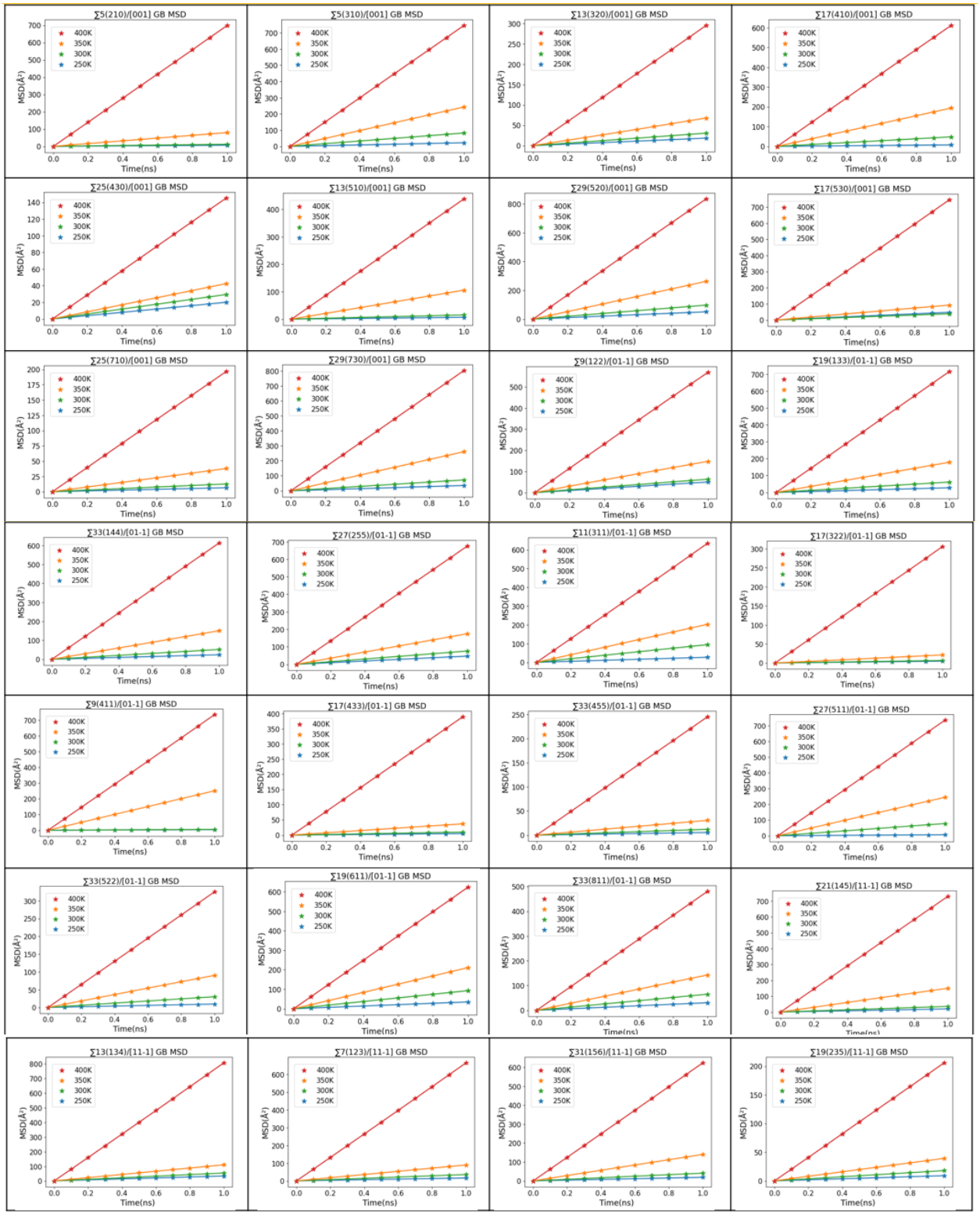

Table A.7 Calculated mean squared displacements for twist GBs.

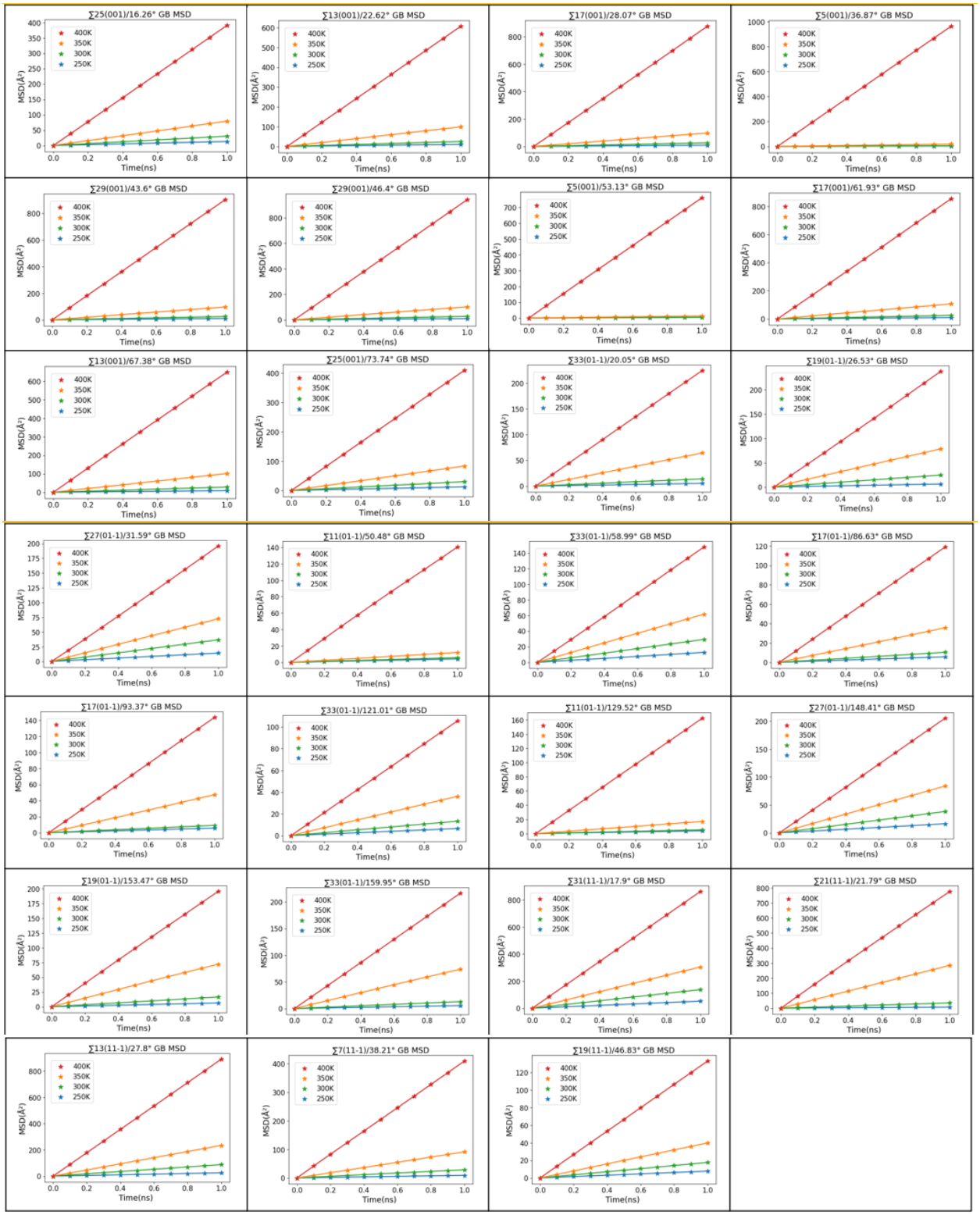

Table A.8 Arrhenius parameters for tilt GBs calculated using fits to low temperature data (250K, 300K, 350K) and high temperature data (300K, 350K, 400K). The calculated values for diffusion in the bulk via a vacancy mechanism are presented for comparison.

	Fit to 250, 300, and 350 K			Fit to 300, 350, and 400 K		
Tilt GB	**E_a (eV)**	**D_0 (cm^2/s)**	**R^2**	**E_a (eV)**	**D_0 (cm^2/s)**	**R^2**
∑5(210)	0.18	$3.66*10^{-4}$	0.83	0.41	1.28	0.96
∑5(310)	0.18	$1.72E*10^{-3}$	0.99	0.23	$8.77*10^{-3}$	0.99
∑13(320)	0.1	$2.40*10^{-5}$	0.95	0.23	$2.80*10^{-3}$	0.92
∑17(410)	0.25	$1.25*10^{-2}$	1	0.27	$2.39*10^{-2}$	1
∑25(430)	0.07	$6.95*10^{-6}$	0.96	0.16	$2.49*10^{-4}$	0.92
∑13(510)	0.2	$1.17*10^{-3}$	0.88	0.34	$1.38*10^{-1}$	1
∑29(520)	0.13	$2.71*10^{-4}$	0.96	0.22	$6.93*10^{-3}$	0.97
∑17(530)	0.05	$6.36*10^{-6}$	0.61	0.3	$5.41*10^{-2}$	0.86
∑25(710)	0.13	$4.14*10^{-5}$	0.93	0.28	$1.06*10^{-2}$	0.94
∑29(730)	0.16	$6.78*10^{-4}$	0.95	0.24	$1.48*10^{-2}$	0.99
∑9(122)	0.09	$3.64*10^{-5}$	0.89	0.22	$5.33*10^{-3}$	0.94
∑19(133)	0.14	$2.40*10^{-4}$	0.95	0.25	$1.55*10^{-2}$	0.96
∑33(144)	0.13	$1.89*10^{-4}$	0.96	0.25	$1.47*10^{-2}$	0.95
∑27(255)	0.1	$6.85*10^{-5}$	0.94	0.22	$6.44*10^{-3}$	0.93
∑11(311)	0.15	$5.36*10^{-4}$	1	0.19	$2.58*10^{-3}$	0.96
∑17(322)	0.11	$1.09*10^{-5}$	0.87	0.38	$1.92*10^{-1}$	0.82
∑9(411)	0.3	$3.87*10^{-2}$	0.5	0.53	$7.51*10^{1}$	0.44
∑17(433)	0.14	$6.04*10^{-5}$	0.89	0.38	$2.60*10^{-1}$	0.89
∑33(455)	0.12	$2.67*10^{-5}$	0.97	0.3	$2.08*10^{-2}$	0.86
∑27(511)	0.28	$4.93*10^{-2}$	0.94	0.23	$8.86*10^{-3}$	0.99
∑33(522)	0.17	$3.72*10^{-4}$	0.99	0.24	$5.09*10^{-3}$	0.98
∑19(611)	0.13	$2.92*10^{-4}$	1	0.2	$2.73*10^{-3}$	0.97
∑33(811)	0.12	$1.10*10^{-4}$	0.99	0.2	$2.40*10^{-3}$	0.95
∑7(123)	0.12	$6.05*10^{-5}$	0.96	0.29	$4.12*10^{-2}$	0.86
∑13(134)	0.09	$3.10*10^{-5}$	0.93	0.27	$2.75*10^{-2}$	0.86
∑21(145)	0.14	$2.12*10^{-4}$	0.88	0.31	$8.16*10^{-2}$	0.97
∑31(156)	0.15	$2.47*10^{-4}$	0.92	0.28	$3.20*10^{-2}$	0.97
∑19(235)	0.11	$1.96*10^{-5}$	0.96	0.25	$4.30*10^{-3}$	0.89
Bulk(cal)	0.48	$2.18*10^{-3}$	1	0.48		1

Table A.9 Arrhenius parameters for twist GBs calculated using fits to low temperature data (250K, 300K, 350K) and high temperature data (300K, 350K, 400K). The calculated values for diffusion in the bulk via a vacancy mechanism are presented for comparison.

	Fit to 250, 300, and 350 K			Fit to 300, 350, and 400 K		
Twist GB	**E_a (eV)**	**D_0 (cm^2/s)**	**R^2**	**E_a (eV)**	**D_0 (cm^2/s)**	**R^2**
∑5(001)/53.13°	0.1	$5.71*10^{-6}$	0.83	0.51	1.75*10	0.63
∑5(001)/36.87°	0.12	$1.24*10^{-5}$	0.82	0.53	4.23*10	0.66
∑13(001)/67.38°	0.18	$7.33*10^{-4}$	0.97	0.32	$1.02*10^{-1}$	0.94
∑17(001)/28.07°	0.18	$6.49*10^{-4}$	0.96	0.36	$3.44*10^{-1}$	0.92
∑25(001)/73.74°	0.14	$1.25*10^{-4}$	0.97	0.26	$1.05*10^{-2}$	0.93
∑13(001)/22.62°	0.17	$3.64*10^{-4}$	0.93	0.33	$1.13*10^{-1}$	0.95
∑29(001)/43.6°	0.17	$4.33*10^{-4}$	0.96	0.36	$3.93*10^{-1}$	0.9
∑17(001)/61.93°	0.18	$5.35*10^{-4}$	0.95	0.36	$3.48*10^{-1}$	0.92
∑25(001)/16.26°	0.14	$1.12*10^{-4}$	0.98	0.26	$1.01*10^{-2}$	0.93
∑29(001)/46.4°	0.18	$5.54*10^{-4}$	0.96	0.36	$4.47*10^{-1}$	0.9
∑19(01-1)/153.47°	0.17	$3.36*10^{-4}$	0.94	0.25	$4.77*10^{-3}$	1
∑33(01-1)/159.95°	0.18	$3.63*10^{-4}$	0.89	0.29	$1.83*10^{-2}$	1
∑11(01-1)/129.52°	0.11	$7.44*10^{-6}$	0.83	0.35	$5.07*10^{-2}$	0.88
∑27(01-1)/148.41°	0.12	$7.55*10^{-5}$	1	0.17	$3.74*10^{-4}$	0.97
∑11(01-1)/50.48°	0.07	$1.81*10^{-6}$	0.88	0.32	$1.70*10^{-2}$	0.79
∑17(01-1)/86.63°	0.14	$4.30*10^{-5}$	0.9	0.27	$4.56*10^{-3}$	0.98
∑17(01-1)/93.37°	0.15	$7.96*10^{-5}$	0.86	0.29	$1.11*10^{-2}$	1
∑33(01-1)/121.01°	0.13	$3.53*10^{-5}$	0.95	0.21	$7.74*10^{-4}$	0.99
∑27(01-1)/31.59°	0.12	$7.27*10^{-5}$	1	0.17	$3.99*10^{-4}$	0.97
∑33(01-1)/58.99°	0.11	$4.28*10^{-5}$	0.99	0.17	$3.26*10^{-4}$	0.98
∑19(01-1)/26.53°	0.19	$6.06*10^{-4}$	0.99	0.23	$3.07*10^{-3}$	1
∑33(01-1)/20.05°	0.18	$3.59*10^{-4}$	0.92	0.29	$1.50*10^{-2}$	1
∑7(11-1)/38.21°	0.18	$5.13*10^{-4}$	0.98	0.27	$1.60*10^{-2}$	0.97
∑13(11-1)/27.8°	0.17	$9.03*10^{-4}$	1	0.23	$1.15*10^{-2}$	0.95
∑21(11-1)/21.79°	0.28	$4.75*10^{-2}$	0.99	0.24	$1.50*10^{-2}$	1
∑31(11-1)/17.9°	0.13	$4.26*10^{-4}$	1	0.19	$2.96*10^{-3}$	0.97
∑19(11-1)/46.83°	0.12	$3.53*10^{-5}$	0.99	0.2	$6.30*10^{-4}$	0.95
Bulk(cal)	0.48	$2.18*10^{-3}$	1	0.48	$2.18*10^{-3}$	1

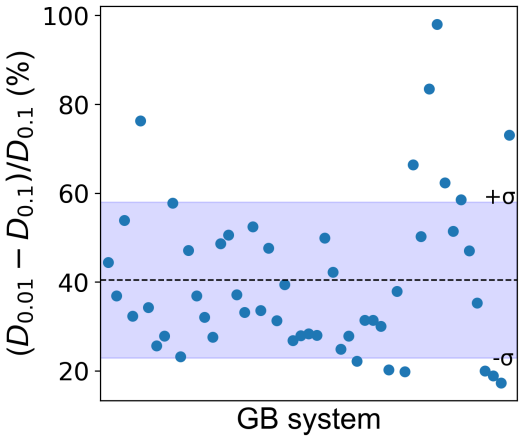

Figure A.1 Change in calculated diffusivity when the identity of GB atoms is updated every 0.01 ns instead of every 0.1 ns. On average, GB diffusivity increases by 40% when the more frequent sampling rate of 0.01 ns is used. As a result, 0.1ns sampling rate is chosen since it does not alter conclusions of the current study and computational cost is less expensive.

Appendix B - Supporting Figures for Chapter 4

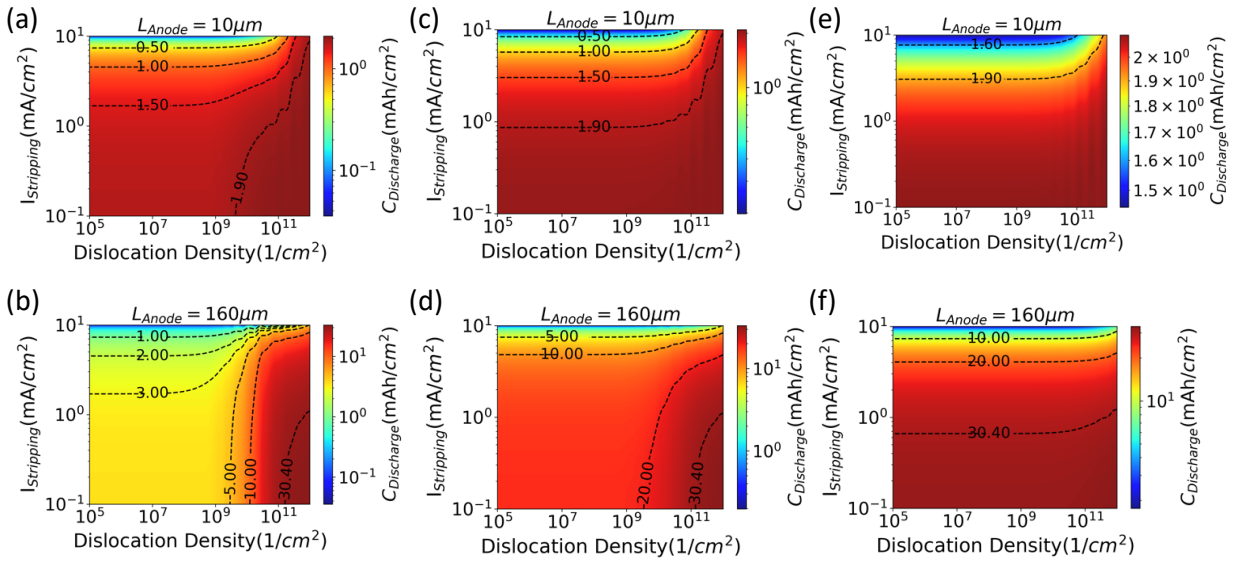

Figure B.1 Maximum discharge capacity at given stripping current, dislocation density, and anode thickness. (a),(b) show the capacity when grain size is 150μm, and (c),(d) show the results when grain size is 10μm, and (e),(f) exhibit the case when grain size is 1μm.

Appendix C - Supporting Figures for Chapter 5

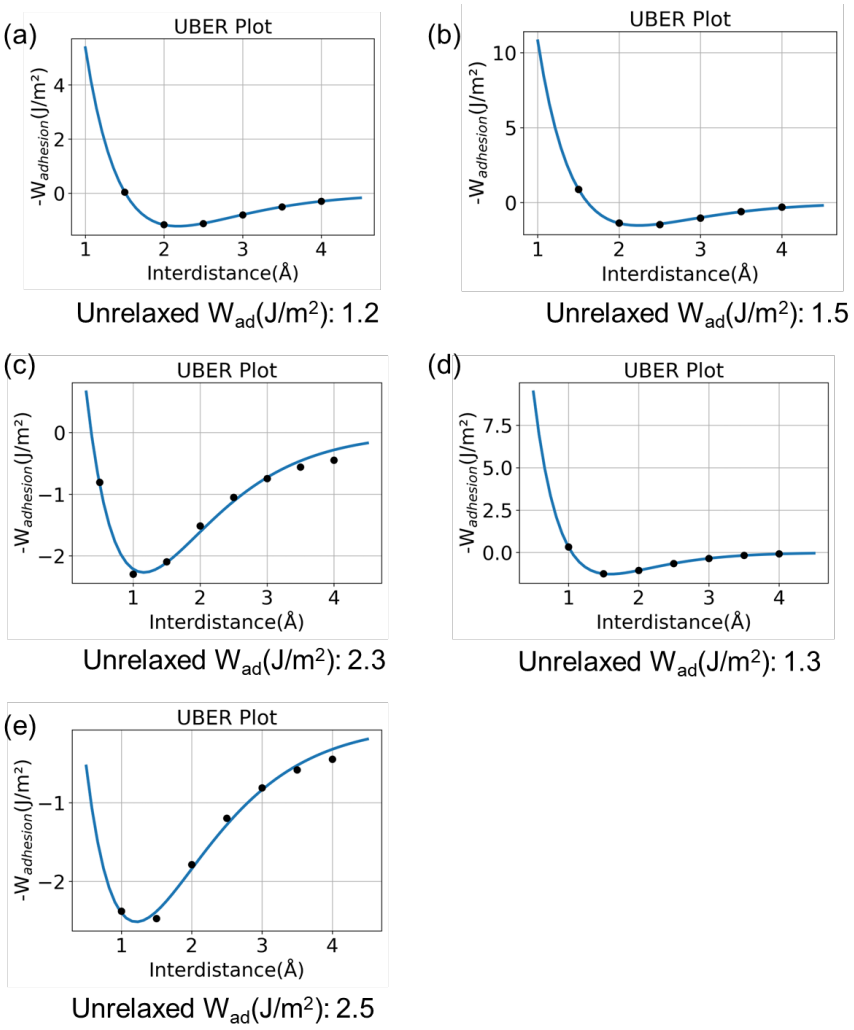

Figure C.1 Universal Binding Energy Relation(UBER) plot of (a) Li(100)-Cu(100), (b) Li(110)-Cu(111), (c) Li(100)-Cu_2O(111)O#2, (d) Li(110)-Cu_2O(111)O#1, (e) Li(110)-Cu_2O(111)O#2 interfaces

Bibliography

1 P. G. Bruce, S. A. Freunberger, L. J. Hardwick and J. M. Tarascon, *Nat Mater*, 2012, 11, 19–29.

2 Z. P. Cano, D. Banham, S. Ye, A. Hintennach, J. Lu, M. Fowler and Z. Chen, *Nat Energy*, 2018, **3**, 279–289.

3 G. Crabtree, *Science (1979)*, 2019, **366**, 422–424.

4 Y. Tian, G. Zeng, A. Rutt, T. Shi, H. Kim, J. Wang, J. Koettgen, Y. Sun, B. Ouyang, T. Chen, Z. Lun, Z. Rong, K. Persson and G. Ceder, *Chem. Rev*, 2021, **121**, 1623–1669.

5 V. Technologies Office, *2020 Vehicle Technologies Office Annual Merit Review Results Report*, 2020.

6 Y. Wang, Y. Liu, M. Nguyen, J. Cho, N. Katyal, B. S. Vishnugopi, H. Hao, R. Fang, N. Wu, P. Liu, P. P. Mukherjee, J. Nanda, G. Henkelman, J. Watt and D. Mitlin, *Advanced Materials*, 2023, **35**, 2206762.

7 N. Kamaya, K. Homma, Y. Yamakawa, M. Hirayama, R. Kanno, M. Yonemura, T. Kamiyama, Y. Kato, S. Hama, K. Kawamoto and A. Mitsui, *Nat Mater*, 2011, **10**, 682–686.

8 S. Yu, H. Park and D. J. Siegel, *ACS Appl Mater Interfaces*, 2019, **11**, 36607–36615.

9 H. Park, S. Yu and D. J. Siegel, *ACS Energy Lett*, 2020, **6**, 150–157.

10 Y. Xiao, L. J. Miara, Y. Wang and G. Ceder, *Joule*, 2019, **3**, 1252–1275.

11 mie Auvergniot, A. Cassel, J.-B. Ledeuil, V. Viallet, V. Seznec and mi Dedryve, *Chemistry of Materials*, 2017, **29**, 3883–3890.

12 L. J. Miara, N. Suzuki, W. D. Richards, Y. Wang, J. C. Kim and G. Ceder, *J Mater Chem A Mater*, 2015, **3**, 20338.

13 S. Wenzel, S. J. Sedlmaier, C. Dietrich, W. G. Zeier and J. Janek, *Solid State Ion*, 2018, **318**, 102–112.

14 R. Koerver, I. Aygü, T. Leichtweiß, C. Dietrich, W. Zhang, J. O. Binder, P. Hartmann, W. G. Zeier and J. Rgen Janek, *Chemistry of Materials*, 2017, **29**, 5574–5582.

15 A. Sakuda, A. Hayashi and M. Tatsumisago, *Chemistry of Materials*, 2010, **22**, 949–956.

16 N. Ohta, K. Takada, I. Sakaguchi, L. Zhang, R. Ma, K. Fukuda, M. Osada and T. Sasaki, *Electrochem commun*, 2007, **9**, 1486–1490.

17 T. Krauskopf, H. Hartmann, W. G. Zeier and J. Janek, *ACS Appl Mater Interfaces*, 2019, **11**, 14463–14477.

18 J. Kasemchainan, S. Zekoll, D. Spencer Jolly, Z. Ning, G. O. Hartley, J. Marrow and P. G. Bruce, *Nat Mater*, 2019, **18**, 1105–1111.

19 M. Wang, J. B. Wolfenstine and J. Sakamoto, *Electrochim Acta*, 2019, **296**, 842–847.

20 P. Albertus, S. Babinec, S. Litzelman and A. Newman, *Nat Energy*, 2018, **3**, 16–21.

21 C. Monroe and J. Newman, *J Electrochem Soc*, 2005, **152**, A396.

22 M. J. Wang, R. Choudhury and J. Sakamoto, *Joule*, 2019, **3**, 2165–2178.

23 C. L. Tsai, T. Lan, C. Dellen, Y. Ling, Q. Ma, D. Fattakhova-Rohlfing, O. Guillon and F. Tietz, *J Power Sources*, 2020, **476**, 228666.

24 T. Krauskopf, B. Mogwitz, C. Rosenbach, W. G. Zeier and J. Janek, *Adv Energy Mater*, , DOI:10.1002/aenm.201902568.

25 M. Siniscalchi, J. Liu, J. S. Gibson, S. J. Turrell, J. Aspinall, R. S. Weatherup, M. Pasta, S. C. Speller and C. R. M. Grovenor, *ACS Energy Lett*, 2022, **7**, 3593–3599.

26 E. Kazyak, M. J. Wang, K. Lee, S. Yadavalli, A. J. Sanchez, M. D. Thouless, J. Sakamoto and N. P. Dasgupta, *Matter*, 2022, **5**, 3912–3934.

27 K. Lee, E. Kazyak, M. J. Wang, N. P. Dasgupta and J. Sakamoto, *Joule*, 2022, **6**, 2547–2565.

28 M. J. Wang, E. Carmona, A. Gupta, P. Albertus and J. Sakamoto, *Nat Commun*, 2020, **11**, 5201.

29 B. J. Neudecker, N. J. Dudney and J. B. Bates, *'Lithium-Free' Thin-Film Battery with In Situ Plated Li Anode*, 2000, vol. 147.

30 Y.-G. Lee, S. Fujiki, C. Jung, N. Suzuki, N. Yashiro, R. Omoda, D.-S. Ko, T. Shiratsuchi, T. Sugimoto, S. Ryu, J. Hwan Ku, T. Watanabe, Y. Park, Y. Aihara, D. Im and I. Taek Han, *Nat Energy*, 2020, **5**, 299–308.

31 S. E. Sandoval, J. A. Lewis, B. S. Vishnugopi, D. L. Nelson, M. M. Schneider, F. Javier, Q. Cortes, C. M. Matthews, J. Watt, M. Tian, P. Shevchenko, P. P. Mukherjee, M. T. Mcdowell and G. W. Woodruff, *https://chemrxiv.org/engage/chemrxiv/article-details/647fdb8e4f8b1884b7f2799c*.

32 C. Haslam and J. Sakamoto, *J Electrochem Soc*, 2023, **170**, 040524.

33 K. Qin, J. Baucom, D. Liu, W. Shi, N. Zhao and Y. Lu, *Small*, 2020, **16**, 2000794.

34 M. Born and R. Oppenheimer, *Ann Phys*, 1927, **389**, 457–484.

35 D. S. Sholl and J. A. Steckel, *John Wiley & Sons Inc.: Hoboken, New Jersey*, 2009, 1–34.

36 W. Kohn and L. J. Sham, *Phys. Rev.*, 1965, **140**, A1133–A1138.

37 J. P. Perdew, K. Burke and M. Ernzerhof, *Phys. Rev. Lett.*, 1996, **77**, 3865–3868.

38 J. P. Perdew and Y. Wang', *Phys Rev B*, 1992, **45**, 244–249.

39 A. V. Krukau, O. A. Vydrov, A. F. Izmaylov and G. E. Scuseria, *Journal of Chemical Physics*, 2006, **125**, 224106.

40 J. P. Perdew, M. Ernzerhof and K. Burke, *Journal of Chemical Physics*, 1996, **105**, 9982–9985.

41 V. I. Anisimov, J. Zaanen and O. K. Andersen, *Phys Rev B*, 1991, **44**, 943.

42 M. Dion, H. Rydberg, E. Schröder, D. C. Langreth and B. I. Lundqvist, *Phys Rev Lett*, 2004, **92**, 246401.

43 G. Kresse and J. Furthmü, *Phys. Rev. B - Condens. Matter Mater. Phys.*, 1996, **54**, 11169.

44 G. Kresse and D. Joubert, *Phys. Rev. B* , 1999, **59**, 1758.

45 P. E. Blöchl, *Phys Rev B*, 1994, **50**, 17953.

46 L. Verlet, *Physical Review*, 1967, **159**, 98–103.

47 June Gunn Lee, *Computational Materials Science An Introduction*, CRC Press, Second edition., 2016.

48 Y. M. Kim, I. H. Jung and B. J. Lee, *Model Simul Mat Sci Eng*, 2012, **20**, 035005.

49 M. I. Baskes, B. J. Lee, H. Kim and Y. Koo Cho, *Phys Rev B Condens Matter Mater Phys*, 2001, **64**, 184102.

50 A. P. Thompson, H. M. Aktulga, R. Berger, D. S. Bolintineanu, W. M. Brown, P. S. Crozier, P. J. in 't Veld, A. Kohlmeyer, S. G. Moore, T. D. Nguyen, R. Shan, M. J. Stevens, J. Tranchida, C. Trott and S. J. Plimpton, *Comput Phys Commun*, 2022, **271**, 108171.

51 E. W. Hart, *Acta metallurgica 5.10 (1957): 597.*

52 I. V. Belova and G. E. Murch, *Journal of Physics and Chemistry of Solids*, 2003, **64**, 873–878.

53 M. Motoyama, M. Ejiri and Y. Iriyama, *J Electrochem Soc*, 2015, **162**, A7067–A7071.

54 M. A. Citrin, H. Yang, S. K. Nieh, J. Berry, W. Gao, X. Pan, D. J. Srolovitz and J. R. Greer, *MRS Bull*, 2020, **45**, 891–904.

55 H. Guo and X.-M. Guo, *Applied Mathematics and Mechanics (English Edition)*, 2007, **28**, 141–149.

56 J.C. Maxwell-Garnett, *Philos. Trans. R. Soc. London*, 1904, **203**, 385–420.

57 J. R. Kalnin and E. Kotomin, *J Phys A Math Gen*, 1998, **31**, 7227–7234.

58 Y. Chen and C. A. Schuh, *J Appl Phys*, 2007, **101**, 063524.

59 T. Frolov and Y. Mishin, *Phys Rev B Condens Matter Mater Phys*, 2009, **79**, 174110.

60 M. B. Isichenko, *Rev Mod Phys*, 1992, **64**, 961.

61 T. R. Jow and C. C. Liang, *J Electrochem Soc*, 1983, **130**, 737–740.

62 C. D. Fincher, C. E. Athanasiou, C. Gilgenbach, M. Wang, B. W. Sheldon, W. C. Carter and Y.-M. Chiang, *Joule*, 2022, **6**, 2794–2809.

63 B. P. Uberuaga, S. Choudhury, X. M. Bai and N. A. Benedek, *Scr Mater*, 2012, **66**, 105–108.

64 P. v. Nerikar, K. Rudman, T. G. Desai, D. Byler, C. Unal, K. J. McClellan, S. R. Phillpot, S. B. Sinnott, P. Peralta, B. P. Uberuaga and C. R. Stanek, *Journal of the American Ceramic Society*, 2011, **94**, 1893–1900.

65 A. Suzuki and Y. Mishin, *J Mater Sci*, 2005, **40**, 3155–3161.

66 C.-L. Liu and S. J. Plimpton, *Phys Rev B*, 1995, **51**, 4523.

67 D. J. Siegel and J. C. Hamilton, *Acta Mater*, 2005, **53**, 87–96.

68 S. Yu and D. J. Siegel, *Chemistry of Materials*, 2017, **29**, 9639–9647.

69 L. Sun, D. Marrocchelli and B. Yildiz, *Nat Commun*, 2015, **6**, 6294.

70 R. A. de Souza, M. J. Pietrowski, U. Anselmi-Tamburini, S. Kim, Z. A. Munir and M. Martin, *Physical Chemistry Chemical Physics*, 2008, **10**, 2067–2072.

71 Z. Zhang, X. Zhou and Z. Liu, *J Alloys Compd*, 2022, **893**, 162389.

72 K. Yan, Z. Lu, H. W. Lee, F. Xiong, P. C. Hsu, Y. Li, J. Zhao, S. Chu and Y. Cui, *Nat Energy*, 2016, **1**, 1–8.

73 A. Pei, G. Zheng, F. Shi, Y. Li and Y. Cui, *Nano Lett*, 2017, **17**, 1132–1139.

74 Y. M. Kim, I. H. Jung and B. J. Lee, *Model Simul Mat Sci Eng*, 2012, **20**, 035005.

75 R. Mohammadzadeh and M. Mohammadzadeh, *J Appl Phys*, 2018, **124**, 035102.

76 J. Marian, B. D. Wirth, G. R. Odette and J. M. Perlado, *Comput Mater Sci*, 2004, **31**, 347–367.

77 H. Yan, K. Tantratian, K. Ellwood, E. T. Harrison, M. Nichols, X. Cui and L. Chen, *Adv Energy Mater*, 2022, **12**, 2102283.

78 Y. Zhao, R. Wang and E. Martínez-Pañeda, *J Mech Phys Solids*, 2022, **167**, 104999.

79 H. Zheng, X. G. Li, R. Tran, C. Chen, M. Horton, D. Winston, K. A. Persson and S. P. Ong, *Acta Mater*, 2020, **186**, 40–49.

80 M. A. Tschopp, K. N. Solanki, F. Gao, X. Sun, M. A. Khaleel and M. F. Horstemeyer, *Phys Rev B Condens Matter Mater Phys*, 2012, **85**, 064108.

81 D. Scheiber, R. Pippan, P. Puschnig and L. Romaner, *Model Simul Mat Sci Eng*, 2016, **24**, 035013.

82 D. M. Saylor, B. S. el Dasher, A. D. Rollett and G. S. Rohrer, *Acta Mater*, 2004, **52**, 3649–3655.

83 P. Heitjans, A. Korblein, H. Ackermann, D. Dubbers, F. Fujara and H. J. stockmann, *Journal of Physics F: Metal Physics*, 1985, **15**, 41–54.

84 P. Heitjans, A. Korblein, H. Ackermann, D. Dubbers, F. Fujara and H.-J. Stockmann, *Journal of Physics F: Metal Physics J. Phys. F: Met. Phys*, 1985, **15**, 41.

85 R. Messer, *Applied physics*, 1975, **6**, 79–88.

86 A. Lodding, J. N. Mundy and A. Ott, *physica status solidi (b)*, 1970, **38**, 559–569.

87 M. Mali, J. Roos, M. Sonderegger, D. Brinkmann and P. Heitjans, *Journal of Physics F: Metal Physics*, 1988, **18**, 403.

88 D. M. Fischer, P. Duwe, S. Indris and P. Heitjans, *Solid State Nucl Magn Reson*, 2004, **26**, 74–83.

89 W. Frank, U. Breier, C. Elsässer and M. Fähnle, *Phys Rev Lett*, 1996, **77**, 518.

90 V. Schott, M. Fähnle and P. A. Madden, *Journal of Physics: Condensed Matter*, 2000, **12**, 1171–1194.

91 P.M. Sargent and M.F. Ashby, *Scripta Metallurgica*, 1984, **18**, 145–150.

92 R. Raj, *Acta Mater*, 2021, **215**, 117076.

93 S. J. Fensin, D. Olmsted, D. Buta, M. Asta, A. Karma and J. J. Hoyt, *Phys Rev E Stat Nonlin Soft Matter Phys*, 2010, **81**, 031601.

94 P. L. Williams and Y. Mishin, *Acta Mater*, 2009, **57**, 3786–3794.

95 M. Torabi Rad, G. Boussinot and M. Apel, *Sci Rep*, 2020, **10**, 21074.

96 B. Wang and H. M. Urbassek, *Phys Rev B*, 2013, **87**, 104108.

97 J. J. Möller and E. Bitzek, *MethodsX*, 2016, **3**, 279–288.

98 Integration and Optimization of Novel Ion Conducting Solids(IONICS) Program Overview, https://arpa-e.energy.gov/sites/default/files/documents/files/IONICS_ProgramOverview.pdf.

99 W. S. LePage, Y. Chen, E. Kazyak, K.-H. Chen, A. J. Sanchez, A. Poli, E. M. Arruda, M. D. Thouless and N. P. Dasgupta, *J Electrochem Soc*, 2019, **166**, A89–A97.

100 B. L. Mehdi, A. Stevens, J. Qian, C. Park, W. Xu, W. A. Henderson, J. G. Zhang, K. T. Mueller and N. D. Browning, *Sci Rep*, 2016, **6**, 34267.

101 D. K. Singh, T. Fuchs, C. Krempaszky, B. Mogwitz, S. Burkhardt, F. H. Richter and J. Janek, *Adv Funct Mater*, 2023, **33**, 2211067.

102 K. P. Larsen, J. T. Ravnkilde, M. Ginnerup and O. Hansen, in *The Fifteenth IEEE International Conference on Micro Electro Mechanical Systems*, 2002, pp. 443–446.

103 A. Ijaz, L. F. Kiss, A. L. Demirel, L. K. Varga and A. Mikó, *Mater Chem Phys*, 2021, **267**, 124681.

104 T. Watanabe, in *Nano-plating Microstructure Control Theory of Plated Film and Data Base of Plated Film Microstructure*, Elsevier, 2004.

105 C. T. Yang and Y. Qi, *Chemistry of Materials*, 2021, **33**, 2814–2823.

106 T. Krauskopf, B. Mogwitz, C. Rosenbach, W. G. Zeier and J. Janek, *Adv Energy Mater*, 2019, **9**, 1902568.

107 J. S. Yoon, H. Sulaimon and D. J. Siegel, *https://chemrxiv.org/engage/chemrxiv/article-details/648fba46be16ad5c572227fb*.

108 J. Kasemchainan, S. Zekoll, D. Spencer Jolly, Z. Ning, G. O. Hartley, J. Marrow and P. G. Bruce, *Nat Mater*, 2019, **18**, 1105–1111.

109 A. Masias, N. Felten, R. Garcia-Mendez, J. Wolfenstine and J. Sakamoto, *J Mater Sci*, 2019, **54**, 2585–2600.

110 P. Pétroff and B. Jouffrey, *Appl Phys Lett*, 1969, **14**, 366–368.

111 M. Alam and S. Groh, *Journal of Physics and Chemistry of Solids*, 2015, **82**, 1–9.

112 W. M. Sherryt, F. Prinzs Lnstitut, R. Fettkbrperphysik and W. Boltzmanngasse, *Acta Metallurgica*, 1980, **28**, 949–954.

113 Y. M. Kim, I. H. Jung and B. J. Lee, *Model Simul Mat Sci Eng*, 2012, **20**, 035005.

114 S. Grabowski, K. Kadau and P. Entel, *Phase Transitions*, 2002, **75**, 265–272.

115 Q. F. Fang and R. Wang, *Phys Rev B*, 2000, **62**, 9317.

116 J. Huang, M. Meyer and V. Pontikis, *Phys Rev Lett*, 1989, **63**, 628–631.

117 J. Von Boehm and R. M. Nieminen, *Phys Rev B*, 1994, **50**, 6450.

118 R. C. Picu and D. Zhang, *Acta Mater*, 2004, **52**, 161–171.

119 D. Hull and D. J. Bacon, *Introduction to dislocations*, Elsevier, 2011, vol. 37.

120 A. Stukowski, V. V. Bulatov and A. Arsenlis, *Model Simul Mat Sci Eng*, 2012, **20**, 085007.

121 G. P. Purja Pun and Y. Mishin, *Acta Mater*, 2009, **57**, 5531–5542.

122 C.-T. Yang, Y. Qi, P. Heitjans, A. Korbleinf', H. Ackermann, D. Dubbers$, F. Fujara$ and H.-J. Stockmann, *Journal of Physics F: Metal Physics J. Phys. F: Met. Phys*, 1985, **15**, 41–54.

123 Cottrell, *London Conference of Institute of Mechanical Engineers (IME, London, 1957)*, 1957, 18.

124 M. Motoyama, M. Ejiri and Y. Iriyama, *J Electrochem Soc*, 2015, **162**, A7067–A7071.

125 Y. Li, Y. Li, A. Pei, K. Yan, Y. Sun, C.-L. Wu, L.-M. Joubert, R. Chin, A. L. Koh, Y. Yu, J. Perrino, B. Butz, S. Chu and Y. Cui, *Science (1979)*, 2017, **358**, 506–510.

126 Arian. P. Mouritz, *Introduction to Aerospace Materials*, Elsevier, 2012.

127 M. Ohring, *Engineering Materials Science*, Elsevier, 1995.

128 T. Ungár, Á. RRévész and A. Borbély., *J. Appl. Cryst*, 1998, **31**, 554–558.

129 H. Conrad, S. Feuerstein and L. Rice, *Materials Science and Engineering*, 1967, **2**, 157–168.

130 H. Adachi, Y. Miyajima, A. Shibata, D. Terada and N. Tsuji, in *13th International Conference on Aluminum Alloys (ICAA13)*, 2012, pp. 61–66.

131 O. A. Ruano, A. K. Miller and O. D. Sherby, *Materials Science and Engineering*, 1981, **51**, 9–16.

132 O. A. Ruano, J. Wadsworth and O. D. Sherby, *Deformation mechanisms in an austenitic stainless steel (25Cr-20Ni) at elevated temperature*, 1985, vol. 20.

133 W. J. Kim and H. T. Jeong, *Journal of Materials Research and Technology*, 2020, **9**, 13434–13449.

134 C. G. Haslam, J. B. Wolfenstine and J. Sakamoto, *J Power Sources*, 2022, **520**, 230831.

135 K. S. Nagy, S. Kazemiabnavi, K. Thornton and D. J. Siegel, *ACS Appl Mater Interfaces*, 2019, **11**, 7954–7964.

136 R. Malini, U. Uma, T. Sheela, M. Ganesan and N. G. Renganathan, *Ionics (Kiel)*, 2009, 15, 301–307.

137 J. Cabana, L. Monconduit, D. Larcher and M. R. Palacín, *Advanced Materials*, 2010, **22**, E170–E192.

138 L. Martin, G. Vallverdu, H. Martinez, F. Le Cras and I. Baraille, *J Mater Chem*, 2012, **22**, 22063–22071.

139 J. S. Lowe and D. J. Siegel, *ACS Appl Mater Interfaces*, 2020, **12**, 46015–46026.

140 L. H. Dubois, *Surf Sci*, 1982, **119**, 399–410.

141 K. R. Lawless and A. T. Gwathmeyt, *Acta metallurgica*, 1956, **4**, 153–163.

142 L. I. Bendavid and E. A. Carter, *Journal of Physical Chemistry B*, 2013, **117**, 15750–15760.

143 S. Yu, R. D. Schmidt, R. Garcia-Mendez, E. Herbert, N. J. Dudney, J. B. Wolfenstine, J. Sakamoto and D. J. Siegel, *Chemistry of Materials*, 2016, **28**, 197–206.

144 N. Liu, J. Sun and D. Wu, in *Advanced Materials Research*, 2011, vol. 335–336, pp. 328–332.

145 J. R. Smith, T. Hong and D. J. Srolovitz, *Metal-Ceramic Adhesion and the Harris Functional*, 1994, vol. 72.

146 K. Kim and D. J. Siegel, *ACS Appl Mater Interfaces*, 2019, **11**, 39940–39950.

147 A. Soon, M. Todorova, B. Delley and C. Stampfl, *Phys Rev B*, 2007, **75**, 125420.

148 M. W. Chase, *NIST-JANAF thermochemical tables, 4th edition*, American Institute of Physics, Melville, NY, 4th edn., 1998, vol. 9.

149 Z. Liu, Y. Qi, Y. X. Lin, L. Chen, P. Lu and L. Q. Chen, *J Electrochem Soc*, 2016, **163**, A592–A598.

150 H. Yuan, J. Nai, H. Tian, Z. Ju, W. Zhang, Y. Liu, X. Tao and X. W. Lou, *Sci Adv*, 2020, **6**, eaaz3112.